OBJECTIVE: Tsunami Society International publishes this journal to increase and disseminate knowledge about tsunamis and their hazards.

DISCLAIMER: Although these articles have been technically reviewed by peers, Tsunami Society International is not responsible for the veracity of any statement, opinion or consequences.

Submit manuscripts of articles, notes or letters to the Editor. If an article is accepted for publication the author(s) must submit a scan ready manuscript, a Doc, TeX or a PDF file in the journal format. Issues of the journal are published electronically in PDF format. Issues of the journal (ISSN 8755-6839) from 1982 thru 2005 are available in PDF format at http://epubs.lanl.gov/tsunami/and at **WWW.TSUNAMISOCIETY.ORG** or on a CD-ROM that may be purchased by contacting Tsunami Society International at tsunamisociety@hawaiiantel.net
Recent and all past journal issues are also available at: http://www.TsunamiSociety.org

Tsunami Society International members are notified by e-mail when a new issue is available. There are minimal page charges for authors who are members of Tsunami Society International for three years and slightly higher for non-members. Permission to use figures, tables and brief excerpts from this journal in scientific and educational works is hereby granted provided that the source is acknowledged.
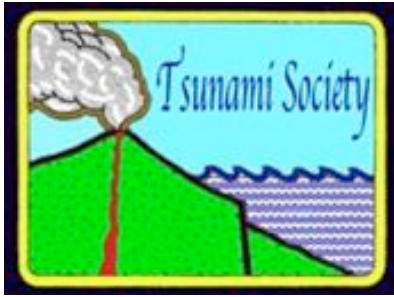
FLOW AND POTENTIAL FORCE DUE TO RUNUP TSUNAMI AROUND A COASTAL FOREST WITH A GAP – EXPERIMENTS AND NUMERICAL SIMULATIONS

Nguyen Ba Thuy [a], Katsutoshi Tanimoto [b], Norio Tanaka [c, *]

[a] Graduate School of Science and Engineering, Saitama University, 255 Shimo-okubo, Sakura-ku, Saitama, 338-8570, Japan.
[b] Emeritus Professor of Saitama University, 255 Shimo-okubo, Sakura-ku, Saitama 338-8570, Japan.
[c,*] Professor, Institute for Environmental Science and Technology, Saitama University, 255 Shimo-okubo, Sakura-ku, Saitama 338-8570, Japan.
Tel./Fax: +81-48-858-3564. E-mail address: tanaka01@mail.saitama-u.ac.jp

ABSTRACT

In the present study, laboratory experiments were conducted to validate the applicability of numerical model based on two-dimensional nonlinear long-wave equations including drag resistance of trees and turbulence induced shear forces to tsunami flow around a simplified forest with a gap in a wave channel. It was confirmed that the water surface elevation and flow velocity by the numerical simulations agree well with the experimental results for various forest conditions of width and tree density. Then the numerical model was applied to a prototype scale condition of a coastal forest of *Pandanus odoratissimus* with a gap to investigate the effects of forest conditions (width and tree density) and incident tsunami conditions (period and height) on a potential tsunami force. The potential tsunami force at the gap exit is greatly enhanced and the maximum in the spatial distribution around and inside the forest. The potential tsunami forces at four representative points at front and back of forest including the center of gap exit were analyzed for various conditions and formulated as function of forest and tsunami conditions in the non-dimensional form. The potential tsunami forces calculated by the curve-fit formula agree well with the simulated potential tsunami forces within ±10% error.

Key words: Runup tsunami, Coastal forest, Gap, *Pandanus odoratissimus*, Tsunami force

Science of Tsunami Hazards, Vol. 29, No. 2, page 43 (2010)

1. INTRODUCTION

Since the Indian Ocean tsunami in 2004, numerous studies have elucidated the effects of coastal vegetation in reducing tsunami forces and the damage to humans and property based on post-tsunami surveys (for example, Danielsen et al. 2005; Kathiresan and Rajendran, 2005; Tanaka et al., 2007). Currently, coastal forests are widely considered to be effective for mitigating tsunami damage from both economic and environmental points of view, although their role is still questioned due to the absence of adequate studies (Kerr and Baird, 2007). In fact, several projects to plant vegetation on coasts as a bioshield against tsunamis have been started in South and Southeast Asian countries (Tanaka et al., 2009; Tanaka, 2009).

The reduction in tsunami damage behind a coastal forest depends on the vegetation species and their dimensions (tree height, diameter, and density), scale and arrangement of the forest (along-shore length and cross-shore width), and tsunami conditions. In relation to forest arrangement, Mascarenhas and Jayakumar (2008) pointed out that roads perpendicular to the beach in a coastal forest served as a passages for a tsunami to travel inland in many places in Tamil Nadu-India on the occasion of the 2004 Indian Ocean tsunami. Fernando et al. (2008) reported that the destruction of coral by the tsunami was remarkable in some places in Hikkaduwa and Akuralla in Sri Lanka, and that the inundation depth behind the destroyed coral reefs was much larger than that behind unbroken coral reefs. Fernando et al. (2008) also conducted a laboratory experiment to verify the effect of an open gap in submerged porous barriers and found that the flow velocity at the gap exit was significantly higher than the case with no gap. Although the latter case was not a coastal forest, those indicate a negative effect of a gap in tsunami runup.

Tanaka et al. (2007) pointed out that *Pandanus odoratissimus*, which is dominant coastal vegetation in South and Southeast Asia, is especially effective in providing protection from tsunami damage due to its density and complex aerial root structure. To study the effect of a gap in a coastal forest of *P. odoratissimus*, Nandasena et al. (2008) performed a numerical simulation including resistance by the forest for limited conditions and found that a narrow gap has a significant effect on the exit flow, but an insignificant effect on the runup height. Thuy et al. (2009a) conducted experiments on a costal forest with a gap by using a simplified model in a 0.4-m-wide wave channel and validated that the numerical results, including the turbulence-induced shear force in addition to the forest resistance, agreed well with experimental results for both runup height and velocity at the gap exit. They also applied the numerical model to a coastal forest of *P. odoratissimus* with a gap and found that a 15-m-wide gap caused the highest velocity under their calculated conditions of a fixed condition of incident tsunami. Based on the discussions in experiment and prototype scale, they confirmed that the turbulence induced shear force gives a significant effect on the flow velocity at the gap exit. Furthermore, Thuy et al. (2009b) discussed the effects of forest and incident tsunami conditions on inundation depth and flow velocity at the gap exit and behind the vegetation patch based on the numerical results.

The tsunami forces are directly related with the damage of trees and other obstacles; however, tsunami forces were not discussed in previous studies using numerical simulations mentioned above. In the present paper, potential tsunami forces due to runup tsunami around a coastal forest of *P. odoratissimus* with a gap are studied by numerical simulations. The potential tsunami force is defined

as the total drag force on a virtual high column with unit width and unit drag coefficient. The numerical model is based on two-dimensional nonlinear long-wave equations incorporating drag resistance of trees and the sub-depth scale (*SDS*) turbulence model by Nadaoka and Yagi (1998). Laboratory experiments on tsunami flow around a simplified forest model with various width and tree density are conducted in a wave channel to validate the applicability of numerical model. The numerical model is then applied to a prototype scale condition of coastal forest of *P. odoratissimus* with a gap to investigate the effects of forest conditions (width and tree density) and incident tsunami conditions (height and period) on the potential tsunami forces. The potential tsunami forces at four representative points at front and back of forest including the center of gap exit are analyzed and formulated in the non-dimensional form.

2. MATHEMATICAL MODEL AND NUMERICAL METHOD

2.1. Governing equations

The governing equations are two-dimensional nonlinear long-wave equations that include drag and eddy viscosity forces due to interaction with vegetation. The continuity and the momentum equations are respectively:

$$\frac{\partial \zeta}{\partial t} + \frac{\partial (dV_x)}{\partial x} + \frac{\partial (dV_y)}{\partial y} = 0 \tag{1}$$

$$\frac{\partial V_x}{\partial t} + V_x \frac{\partial V_x}{\partial x} + V_y \frac{\partial V_x}{\partial y} + g \frac{\partial \zeta}{\partial x} + \frac{\tau_{bx}}{\rho d} + \frac{F_x}{\rho d} - \frac{E_{Vx}}{d} = 0 \tag{2}$$

$$\frac{\partial V_y}{\partial t} + V_x \frac{\partial V_y}{\partial x} + V_y \frac{\partial V_y}{\partial y} + g \frac{\partial \zeta}{\partial y} + \frac{\tau_{by}}{\rho d} + \frac{F_y}{\rho d} - \frac{E_{Vy}}{d} = 0 \tag{3}$$

where,

$$\vec{\tau}_b = \frac{\rho g n^2}{d^{1/3}} \vec{V} \left| \vec{V} \right| \tag{4}$$

$$\vec{F} = \gamma \frac{1}{2} \rho C_{D-all} b_{ref} \vec{V} \left| \vec{V} \right| d \tag{5}$$

$$E_{vx} = 2\frac{\partial}{\partial x}\left(d\nu_e \frac{\partial V_x}{\partial x}\right) + \frac{\partial}{\partial y}\left(d\nu_e \frac{\partial V_x}{\partial y} + d\nu_e \frac{\partial V_y}{\partial x}\right) \tag{6}$$

$$E_{vy} = 2\frac{\partial}{\partial y}\left(d\nu_e \frac{\partial V_y}{\partial y}\right) + \frac{\partial}{\partial x}\left(d\nu_e \frac{\partial V_x}{\partial y} + d\nu_e \frac{\partial V_y}{\partial x}\right) \tag{7}$$

x and y are the horizontal coordinates; V_x and V_y are the depth-averaged velocity components in x and y directions respectively; t is the time; d the total water depth ($d=h+\zeta$); h the local still water depth (on land, the negative height of the ground surface); ζ the water surface elevation; g the gravitational acceleration; ρ the water density; n the Manning roughness coefficient; γ the tree density (number of trees/m^2). $C_{D\text{-}all}$ is the depth-averaged equivalent drag coefficient considering the vertical stand structure of the trees, which was defined by Tanaka et al. (2007) as:

$$C_{D-all}(d) = C_{D-ref} \frac{1}{d} \int_0^d \frac{b(z_G)}{b_{ref}} \frac{C_D(z_G)}{C_{Dref}}) dz_G \tag{8}$$

where $b(z_G)$ and $C_D(z_G)$ are the projected width and drag coefficient of a tree at height z_G from the ground surface, and b_{ref} and $C_{D\text{-}ref}$ are the reference width of the trunk and the reference drag coefficient at breast height, respectively. The eddy viscosity v_e is given by the *SDS* turbulence model as described below.

2.2. Turbulence model

The *SDS* turbulence model of Nadaoka and Yagi (1998) was applied to evaluate the eddy viscosity with modifications related to the bottom friction and vegetation resistance.

$$\frac{\partial k_D}{\partial t} + V_x \frac{\partial k_D}{\partial x} + V_y \frac{\partial k_D}{\partial y} = \frac{1}{d} \frac{\partial}{\partial x}\left(d \frac{v_e}{\sigma_k} \frac{\partial k_D}{\partial x}\right) + \frac{1}{d} \frac{\partial}{\partial y}\left(d \frac{v_e}{\sigma_k} \frac{\partial k_D}{\partial y}\right) + p_{kh} + p_{kv} + p_{kd} - \varepsilon_D \tag{9}$$

$$p_{kh} = v_e \left[2\left(\frac{\partial V_x}{\partial x}\right)^2 + \left(\frac{\partial V_x}{\partial y} + \frac{\partial V_y}{\partial x}\right)^2 + 2\left(\frac{\partial V_y}{\partial y}\right)^2 \right] \tag{10}$$

$$p_{kv} = \frac{gn^2}{d^{4/3}}(V_x^2 + V_y^2)^{1.5} \tag{11}$$

$$p_{kd} = \frac{\gamma b_{ref} C_{D-all}}{2}(V_x^2 + V_y^2)^{1.5} \tag{12}$$

$$v_e = c_w \frac{k_D^2}{\varepsilon_D} \tag{13}$$

$$\varepsilon_D = c_d \frac{k_D^{1.5}}{l_D} \tag{14}$$

where k_D is the kinetic energy and $l_D = \lambda\, d$ is the length scale (λ: turbulence length scale coefficient). For the model parameters, standard values are adopted: $c_w=0.09$, $c_d=0.17$, $\sigma_k=1.0$ and $\lambda=0.08$.

2.3. Method of numerical simulations

A set of the above equations is solved by the finite-difference method of a staggered leap-frog scheme, which is widely used in numerical simulations of tsunami (for example, Liu et al., 1994; Titov and Synolakis, 1997; Imamura et al., 1998; Koh et al., 2009). An upwind scheme was used for nonlinear convective terms in order to maintain numerical stability. A semi-Crank–Nicholson scheme was used for the terms of bed friction, drag, and turbulence-induced shear force. On the offshore sides, a wave generation zone with a constant water depth in which the governing equations were reduced to linear long-wave equations was introduced to achieve non-reflective wave generation by using the method of characteristics. A sinusoidal incident tsunami was given as a time-dependent boundary condition at the most offshore side of the wave-generation zone. For a moving boundary treatment, a number of algorithms were necessary so that the flow occurring when the water surface elevation is high enough can flow to the neighboring dry cells. The initial conditions were given for a waveless state in the computational domain including the wave-generation zone.

3. EXPERIMENTS AND VALIDATION OF NUMERICAL MODEL

3.1. Experimental setup and conditions

The present experiments are follow-up from Thuy et al. (2009a) in which the effect of gap width on flow around a simplified forest model of vertical cylinders with a fixed width and tree density was investigated by a fixed condition of long waves in a wave channel with 0.4 m wide. It was found that a 0.07 m-wide gap causes the largest velocity at the gap exit under their conditions. In this study, the effects of forest conditions on the flow velocity and water surface elevation at the gap exit and behind the vegetation patch are mainly investigated.

Fig. 1 shows the experimental setup in the wave channel where the forest model was set in the water area for the convenience of velocity measurements. Trees were simply modeled by wooden cylinders with a diameter of 0.005 m mounted in a staggered arrangement as seen in Fig. 2. The gap width b_G was fixed as 0.07 m in the present experiments. The forest width B_F was changed in cases of 0.2, 0.5, 0.7 and 1.0 m with the fixed density of 2200 trees/m^2 (0.22 trees/cm^2). The end of forest was fixed at x=11.36 m (see Fig. 1), where the still water depth is 0.037 m. Three cases of tree density for the fixed forest width of 1.0 m were tested; lower density (γ=500 tree/m^2), moderate density (γ=1000 trees/m^2), and higher density (γ=2200 trees/m^2). In addition to those cases, experiments for cases of no forest ($B_F=\gamma=0$) and full vegetation (no gap) were also conducted. Wave condition was fixed as that the incident wave height H_i at still water depth of 0.44 m is 0.02 m and the wave period T is 20 s as same as the previous experiments (Thuy et al., 2009a).
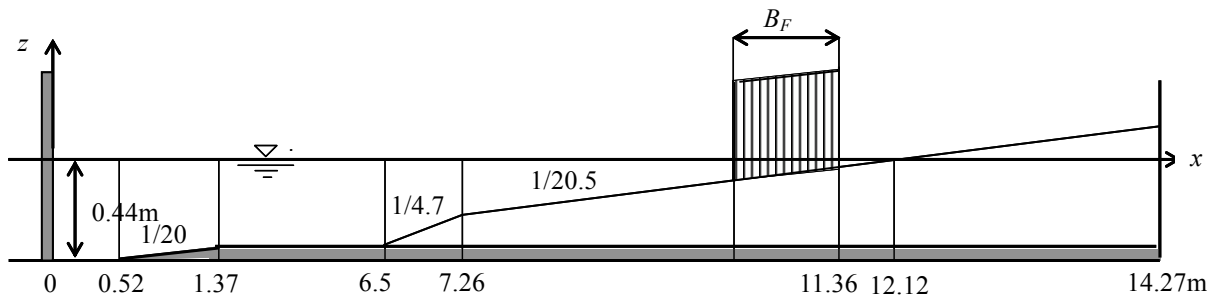
Fig. 1. Experimental setup in wave channel.
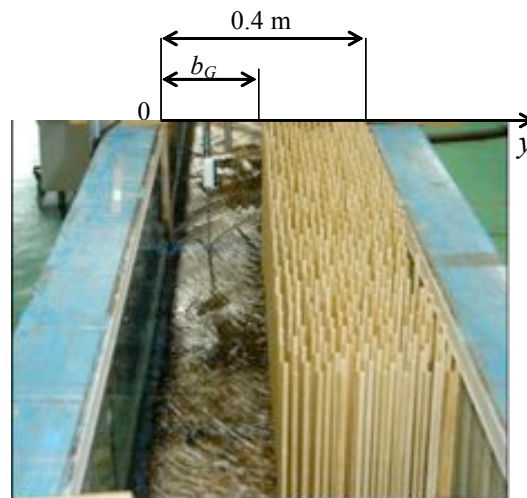
Fig. 2. Photo of forest model (example of b_G=0.15 m).

3.2. Conditions of numerical simulation for laboratory scale

For numerical simulations of the experimental conditions, the uniform grid size of 0.005 m and time step of 0.002 s were selected. The Manning roughness coefficient n was given as 0.012 s/m$^{1/3}$ for the relatively rough wooden bottom. For parameters in the turbulence model, standard values as indicated in *2.2.* were applied. The drag coefficient $C_{D\text{-}ref}$ depends on both the Reynolds number and relative spacing of vegetation (s/D), where s is the distance between cylinders and D is the diameter of cylinder. However, Chakrabati (1991) showed that the interaction between multiple cylinders becomes small when s/D is larger than 2, and the drag coefficient of multiple cylinders approaches to a single cylinder. In the present experimental conditions, the drag coefficient may be assumed as a single

cylinder because the s/D is considerably greater than 2. The drag coefficient C_{Dref} was determined to be 1.5 after some trial calculations, which is consistent with the drag coefficient of a circular cylinder in the laboratory scale corresponding to the Reynolds number of 300.

The measurements of water surface elevation and horizontal velocity in the experiments were made in a steady state in multi-reflection system of wave channel between reflective wave paddle and coastal model with forest. Consequently, the incident wave height in the numerical simulations must be given with consideration of the effect of reflected waves. Fig. 3 shows examples of wave height measured at six locations in cases of no vegetation and full vegetation. In the figure, two distributions simulated with the incident wave height H_i of 0.02 m are plotted for the actual channel length and for the channel length extended by 21 m, which corresponds to a half of wavelength at the still water depth of 0.44 m. Both results coincide well as the difference is not observed in the figure, because of non-reflective wave generation in the numerical simulations. The simulated distributions also agree well with measured wave heights and the separated incident wave heights on the basis of small amplitude theory at the extended channel are about 0.02 m. Therefore, H_i =0.02 m can be considered as the incident wave height at the still water depth of 0.44 m in the multi-reflection system of wave channel in the present experimental conditions.
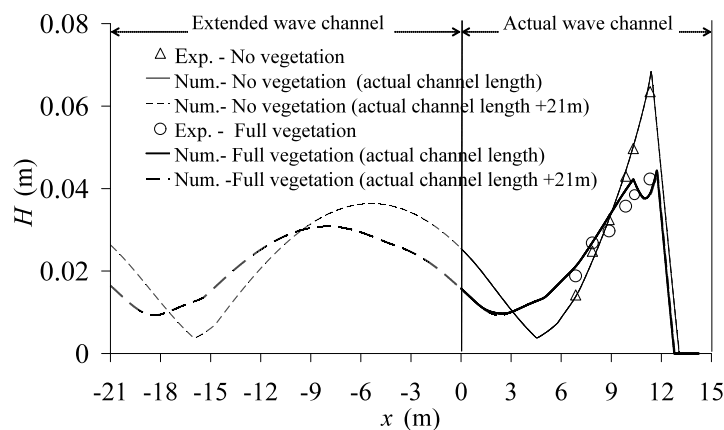
Fig. 3. Wave height distributions in wave channel.

Fig. 4 shows examples of time variation of velocity at the center of vegetation end (y=0.235 m) and the center of gap exit (y=0.035 m) at x=11.4 m during the analyzed time interval of measurements. It is confirmed that the flow velocity is almost steady and the simulated maximum value in particular agrees well with the measured maximum values as already shown in the previous study (Thuy et al., 2009a). The velocity is defined by the following equation because the tsunami flow dominated in the direction of the x-axis in the present study:

$$V = \text{sign}(V_x)|\vec{V}| \tag{15}$$
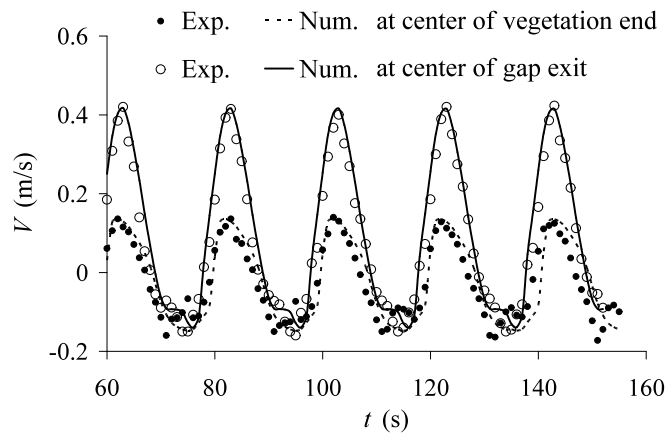
Fig. 4. Time variations of flow velocity (b_G=0.07 m).

3.3. Validation of numerical model with respect to forest conditions

Fig. 5 shows the distribution of maximum velocity in y-direction at the forest end (x=11.4m) for three cases of tree density. The change of velocity gradient around the edge of gap is remarkable, which suggests the importance of turbulence induced shear force at the gap as already discussed by Thuy et al. (2009a). It is also noted that the increase in tree density reduces the velocity behind the vegetation patch, whereas it increases in the velocity at the gap exit. Those are fairly well realized in the present numerical model simulations.
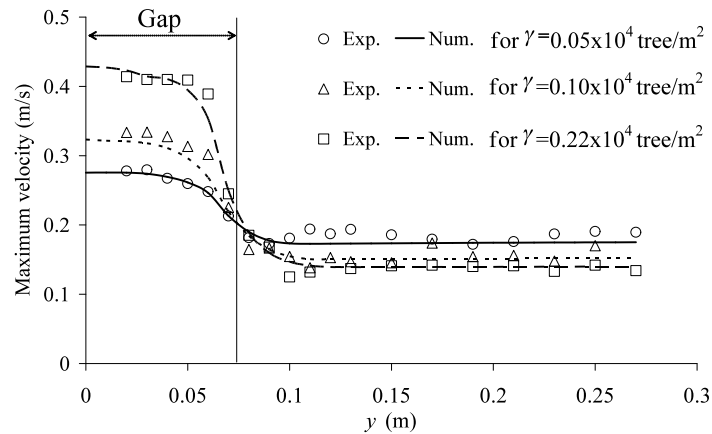
Fig. 5. Distribution of maximum velocity (x=11.4 m).

Fig. 6 shows the variation of the change of wave crest (ζ_{max}), maximum velocity at the gap exit (V_{Gmax}) and maximum velocity at the center behind the vegetation patch (V_{VPmax}) against the forest width. The wave crest and velocity behind the vegetation patch decreases and the maximum velocity at the gap exit increases as forest width increases. The numerical results agree fairly well with the experimental results.
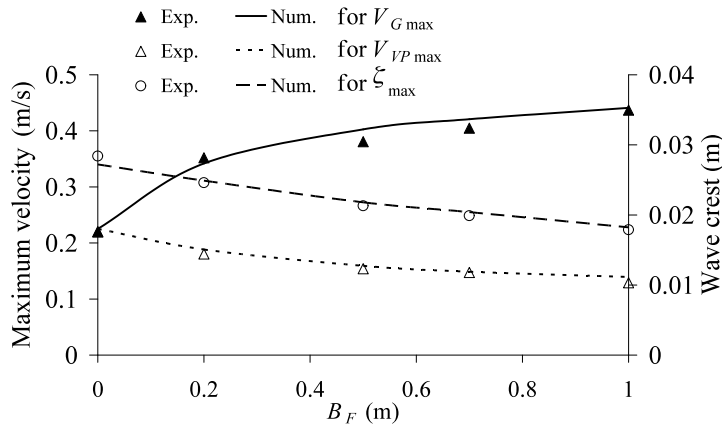
Fig. 6. Effect of forest width on maximum velocity and wave crest height.

4. EFFECT OF FOREST AND TSUNAMI CONDITIONS ON POTENTIAL TSUNAMI FORCES IN ACTUAL SCALE

4.1. Topography, forest and tsunami conditions, and definitions of potential tsunami force

4.1.1. Topography and forest conditions

A uniform coastal topography with the cross-shore section perpendicular (*x*-axis) to a straight shoreline, as shown in Fig.7 (a), was selected as a model case. The bed profile of the domain consists of four slopes, S=1/10, 1/100, 1/50, and 1/500. The offshore water depth at an additional wave-generation zone with a horizontal bottom is 100 m below the datum level of z=0. The tide level at the attack of the tsunami was considered to be 2 m, and therefore the still water level is 2 m above the datum level. The direction of the incident tsunami is perpendicular to the shoreline.

The coastal forest starts at the starting point of the 1/500 slope on the land (*x*=5700 m), where the ground is 4 m above the datum level (2 m above the tide level at the tsunami event). The forest was assumed to extend in the direction of the shoreline (*y*-axis) with the arrangement of a gap and vegetation patches with an along-shore unit length of L_F and a cross-shore width of B_F, as shown in Fig. 7(b). Both side boundaries, shown by dot-and-dash lines in the figure, are mirror image axes in which no cross flow exists. A gap with a width b_G is perpendicular to the shoreline and located at the center of the along-shore forest length. In the present study, the forest length L_F and gap width b_G were fixed as 200 m and 15 m respectively. The forest width B_F was changed from 0 m (no forest) to

200 m for selected cases, and the forest width of 1000 m was additionally considered in order to investigate an extreme condition. According to Thuy et al. (2009a), the forest (L_F=200 m) is long enough to avoid the effect of a gap around the mirror image boundary, so that tsunami flow becomes one-dimensional there as in the case of coastal forest without a gap. In the numerical simulations, the uniform grid size of 2.5 m was applied. In Fig. 7(b), representative checkpoints of simulated results are shown as A (x=5700+B_F+1.25 m, y=100 m), B (x=5700+B_F+1.25 m, y=156.25 m), C (x=5701.25 m, y=108.75 m) and D (x=5701.25 m, y=156.25 m). The Manning roughness coefficient n was set as 0.025 s/m$^{1/3}$ for a relatively rough bare ground, which is widely used in numerical simulations of tsunami runup (for example, Harada and Imamura, 2005).

(a)

(b)
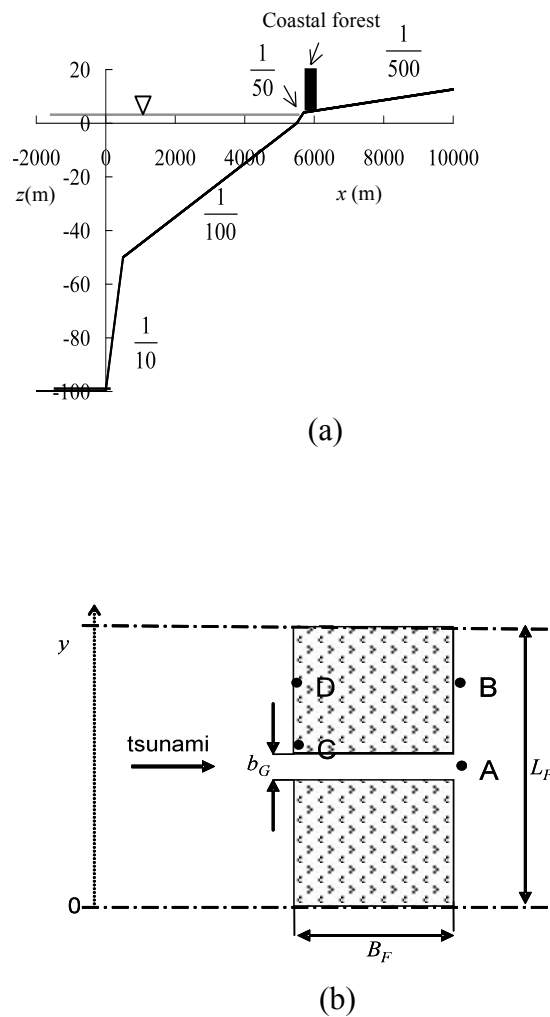
Fig. 7. Schematic topography. (a) Cross section, (b) sketch of forest and gap arrangement.

In the present study, a coastal forest consisting of *P. odoratissimus* was considered. As shown in Fig. 8(a), *P. odoratissimus* has a complex aerial root structure that provides additional stiffness and increases the drag coefficient. Fig. 8(b) shows the $b(z_G)/b_{ref}$, $C_D(z_G)/C_{Dref}$, and C_{D-all} of *P. odoratissimus* based on Tanaka et al. (2007) for the conditions of the tree height H_{Tree}=8 m (for a mature tree), the reference diameter b_{ref}=0.195 m. The reference drag coefficient C_{D-ref} of 1.0 was adopted for a trunk with a circular section and a rough surface in the region of high Reynolds number. The value of C_{D-all} varied with the total depth d (inundation depth) because the projected width b and the drag coefficient C_D vary with the height from the ground surface z_G as shown in the figure. The tree density γ was changed from 0 (no forest) to 0.4 trees/m^2 in numerical simulations.

(a)
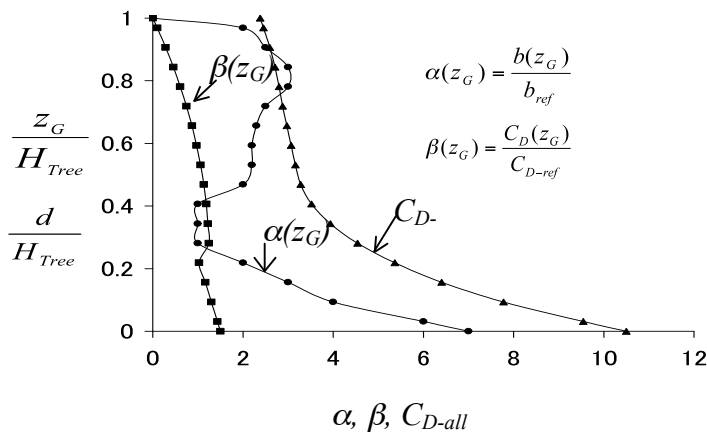
(b)

Fig. 8. Characteristics of *P. odoratissimus*. (a) Photographs of a stand, and (b) vertical distribution of α, β, and C_{D-all}.

4.1.2. Tsunami conditions

As already described, the tsunami attack on the coast is perpendicular to the shoreline at a tide level of 2 m. An incident tsunami at the offshore boundary is a sinusoidal wave starting positive with period T and height H_i from 600 to 3600 s and from 2 to 8 m, respectively. In the present paper, the runup of only the first wave was analyzed because it has the largest runup height among continuous waves.

The incident tsunami height (H_i) at the offshore boundary is rather arbitrary because the offshore boundary may be set at an arbitrary depth. Therefore, the tsunami height (H_{sl0}) above the ground surface at the shoreline was used instead of H_i and called the 'incident tsunami height' for the simplicity in the present paper. The range of H_{sl0} is from 3.08 to 8.51 m corresponding to H_i=2 to 8 m with T=1200 s. Note that the suffix 0 in the present paper indicates the absence of a coastal forest.

Fig. 9 shows the spatial distributions of water surface elevation ζ, mean velocity V and $\sqrt{gd}$ of the first runup wave of T=1200 s and H_i=6 m without forest at the time when the water surface elevation at the shoreline is the maximum as H_{sl0}=6.94 m. It is apparent that the runup tsunami is no more like a sinusoidal wave but a bore-like wave and the front is a super-critical flow.
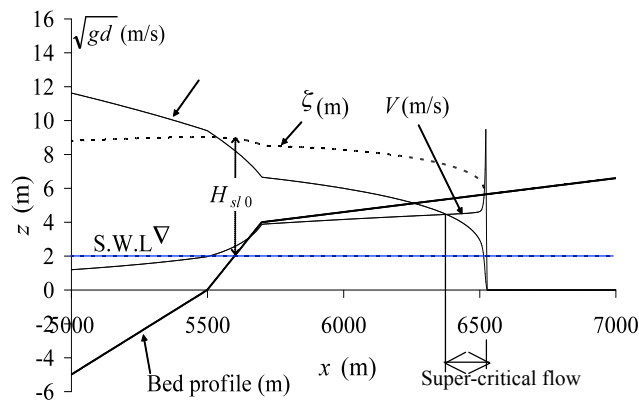
Fig. 9. Spatial distribution of runup tsunami (T=1200 s, H_i=6 m) in the case of no forest at the time when the water surface elevation at the shoreline is the maximum.

4.1.3. Summary of combined conditions of forest and tsunami

Table 1 summarizes combined condition of forest and tsunami in the numerical simulations.

Table 1. Summary of all simulation cases for combined conditions of forest and tsunami.

Series	B_F (m)	γ (trees/m^2)	H_{sl0} (m)	T (s)
Change of forest conditions				
1	0–200, 1000	0.226	6.94	1200
2	100	0–0.4	6.94	1200
Change of tsunami conditions				
3	100	0.226	3.08–8.51	1200
4	100	0.226	6.94	600–3600
Change of tree density and tsunami conditions				
5	100	0.05	4.21–7.73	1200
6	100	0.05	6.94	600–3600
7	100	0.1	4.21–7.73	1200
8	100	0.1	6.94	600–3600
Change of forest width and tsunami conditions				
9	20	0.226	4.21–7.73	1200
10	20	0.226	6.94	600–3600
11	50	0.226	4.21–7.73	1200
12	50	0.226	6.94	600–3600

4.1.4. Definition of a potential tsunami force and the time variation

The tsunami force vector ($\vec{F}^*$) in the present paper is defined by the following equation:

$$\vec{F}^* = \frac{1}{2}\rho d\vec{V}\left|\vec{V}\right| \tag{16}$$

This is a potential tsunami force integrated over the inundation depth and corresponds to the total drag force due to the tsunami acting on a virtual tall column of unit width and a unit drag coefficient. For an example, the integrated drag force vector ($\vec{F}_{Tree}$) on a single tree with a height of H_{Tree} can be calculated by the following relationship:

$$\begin{aligned}
\vec{F}_{Tree} &= C_{D-all}b_{ref}\vec{F}^*, & H_{Tree} \geq d \\
&= C_{D-all}b_{ref}\frac{H_{Tree}}{d}\vec{F}^*, & H_{Tree} < d
\end{aligned} \tag{17}$$

Similarly, the total drag force on a human body as an application may be calculated with appropriate $C_{D\text{-}all}$ and b_{ref} specified to the human body.

Fig. 10 shows the time variations of inundation depth d, mean velocity V, tsunami force F^* for the condition of B_F=100 m, γ=0.226 trees/m^2, H_{sl0}=6.94 m and T=1200 s at the representative checkpoint C. As observed in the figure, the temporal maxima appear at different times. In particular, the maximum of V appeared early in the tsunami arrival when the inundation depth is low, and consequently, the tsunami force was not maximal. Therefore, the representative inundation depth and velocity are defined as values at the time of the temporal maxima of tsunami force (F^*_{max}; hereafter, simply called 'tsunami force'). They are denoted as d_{F^*max}, V_{F^*max} .
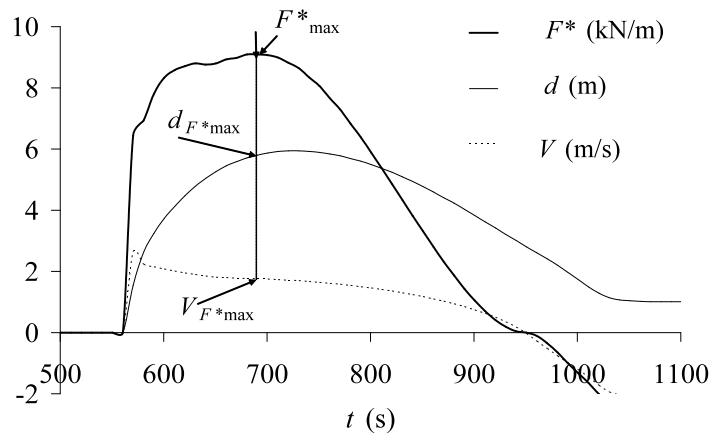
Fig. 10. Time profiles of inundation depth (d), mean velocity (V) and tsunami force (F^*) at C.

4.2. Results and discussions

4.2.1. Overview of tsunami runup around forest

In this section, the tsunami runup around a forest with a width of 100 m and a density of 0.226 trees/m^2 is summarized as an example for the incident tsunami conditions of T=1200 s and H_{sl0}=6.94 m. Fig. 11(a) and (b) show the x-y distributions of the maximum inundation depth d_{max} and the representative inundation depth d_{F^*max}, respectively. The distribution of the maximum inundation depth decreases monotonously from about 6 m at the front of the forest to about 3.5 m at the back of the forest. The distribution of the representative inundation depths for the maximum tsunami force is different from that of the maximum inundation depth. In particular, the representative inundation depth in front of the forest is small as 2–3 m. This is because the maximum tsunami force occurred early in the tsunami's arrival and the velocity at the time of the maximum inundation depth was reduced by reflected waves from the forest.
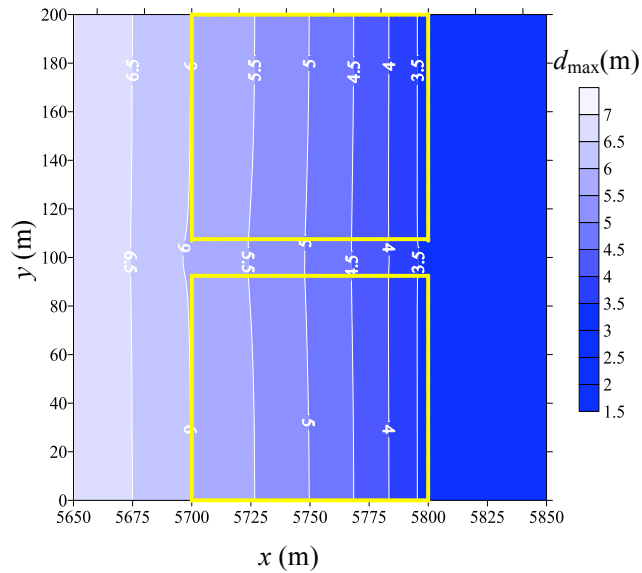
(a)
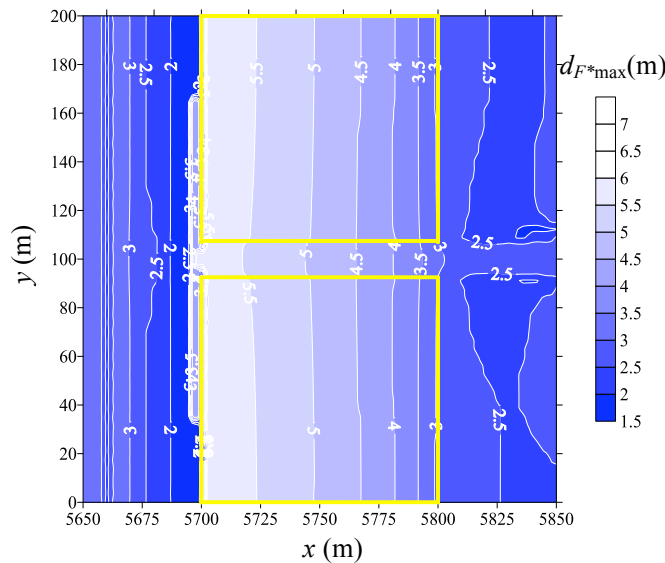
(b)

Fig. 11. Distributions of (a) maximum inundation depth (d_{max}), and (b) representative inundation depth (d_{F*max}).

Fig. 12 (a) and (b) show the distributions of the maximum and representative velocity, respectively. As already pointed out by Thuy et al. (2009a), the velocity increased in the gap and became large around the gap exit. The spatial maximum appears behind the gap exit and exceeds 7.5 m/s in the temporal maximum velocity and 7.0 m/s in the representative velocity for the maximum tsunami force. Fig. 13

shows the distributions of the maximum tsunami force. The spatial maximum tsunami force appears at the gap exit (checkpoint A) and exceeds 75 kN/m.

(a)

(b)
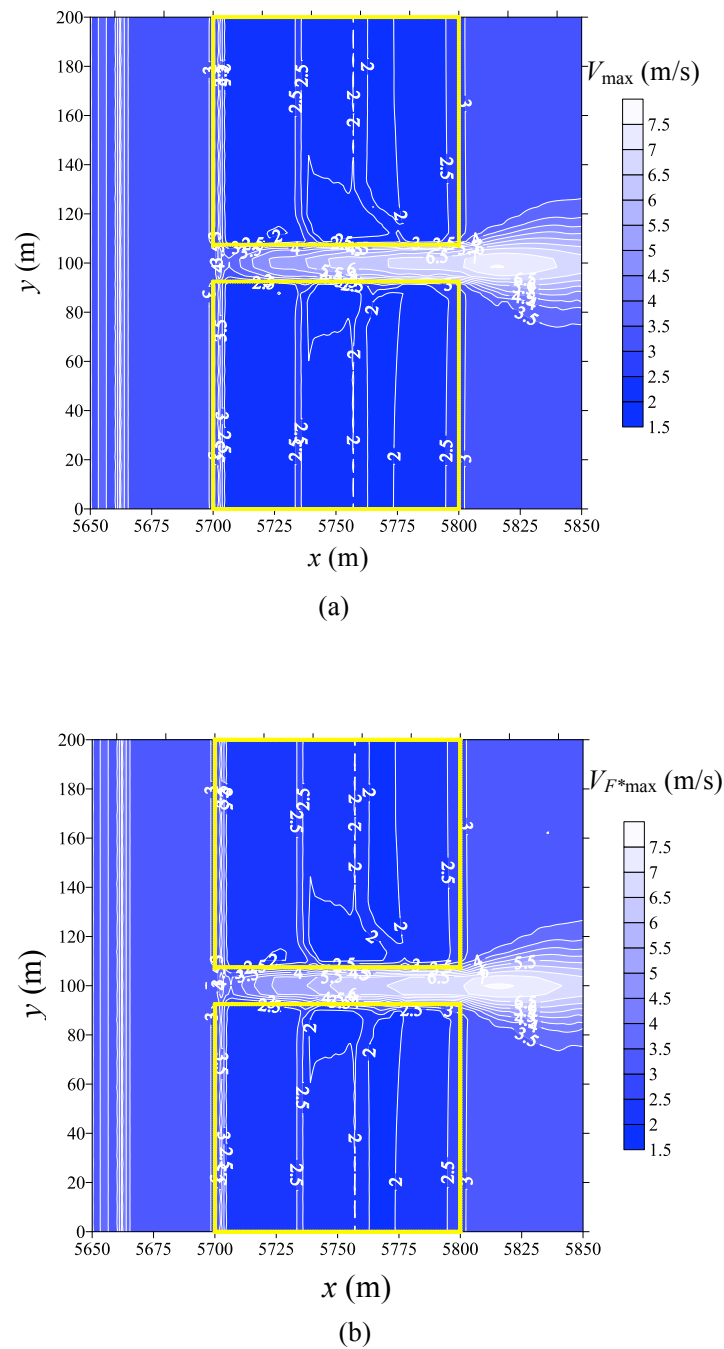
Fig. 12. Distribution of (a) maximum velocity (V_{max}), and (b) representative velocity (V_{F*max}).

Figs. 11-13 show that the contour line tends to become straight and parallel to the y-axis as the distance from the gap increases. This implies that the tsunami runup near the side boundaries is one-dimensional like the case with no gap. In the present paper, the representative checkpoints D and B were selected as corresponding to the case with no gap, although only a slight difference was apparent.
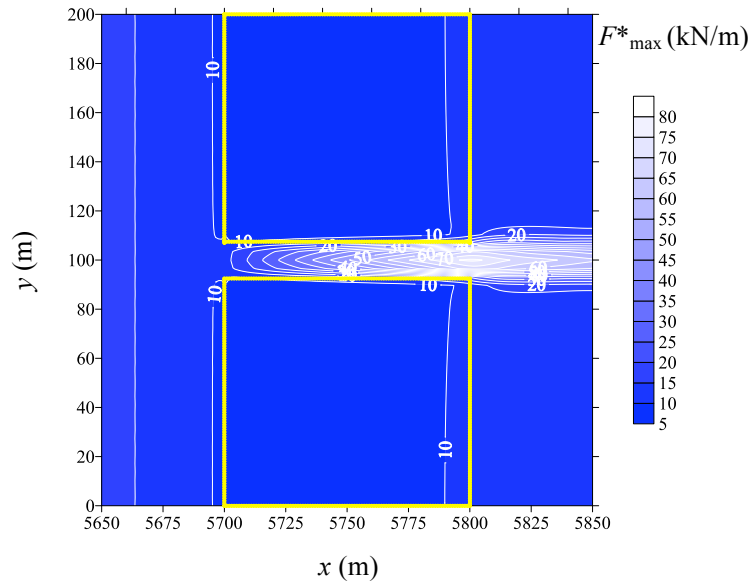
Fig. 13. Distribution of maximum tsunami force (F^*_{max}).

4.2.2. Effect of forest conditions

The tsunami force obtained by the incident tsunami condition of T=1200 s and H_{sl0}=6.94 m for different forest conditions were plotted in Fig. 14(a) and (b) against the following forest thickness B_{dNall}:

$$\begin{aligned} B_{dNall} &= \gamma \left(1 \times B_F\right) b_{ref} C_{D-all} \\ &= \gamma B_F b^*_{ref} C_{D-all} \end{aligned} \tag{18}$$

where, b_{ref} is the reference width per tree and b^*_{ref} is a logical reference width so that B_{dNall} has a unit of meters in the simple form (Note that b^*_{ref} has the same value as b_{ref}, but the unit is m^2/tree). The original form of forest thickness was proposed by Shuto (1987) for the combined effect of forest width and tree density. Tanaka et al. (2009) improved it to include resistance characteristic (C_{D-all}) due to the tree species as the upper expression in the right hand side of Eq.(18). In the present paper, the lower expression is used to make brief.

The forest width was changed with fixed tree density of 0.226 trees/m^2 and the tree density was changed with fixed forest width of 100 m. Tsunami forces F^*_{maxB}, F^*_{maxC} and F^*_{maxD} at points B, C and D decrease as the forest width and tree density increase due to mainly decrement of velocity with increase of forest resistance. On the other hand, the tsunami force F^*_{maxA} at point A is enhanced greatly but behaves in different ways by the forest width or tree density. This difference could be understood by the fact that the tsunami force with the increase of tree density increases to an extreme value corresponding to a rigid forest with the infinite density at the fixed point, while the tsunami force with the increase of forest width increases at first and then decreases to 0 finally because of the moving point. The enhancement of tsunami force at point A with the increase of density and width is due to the increase of velocity at the gap exit in spite of decrease of inundation depth as explained as the followings.

(a)

(b)
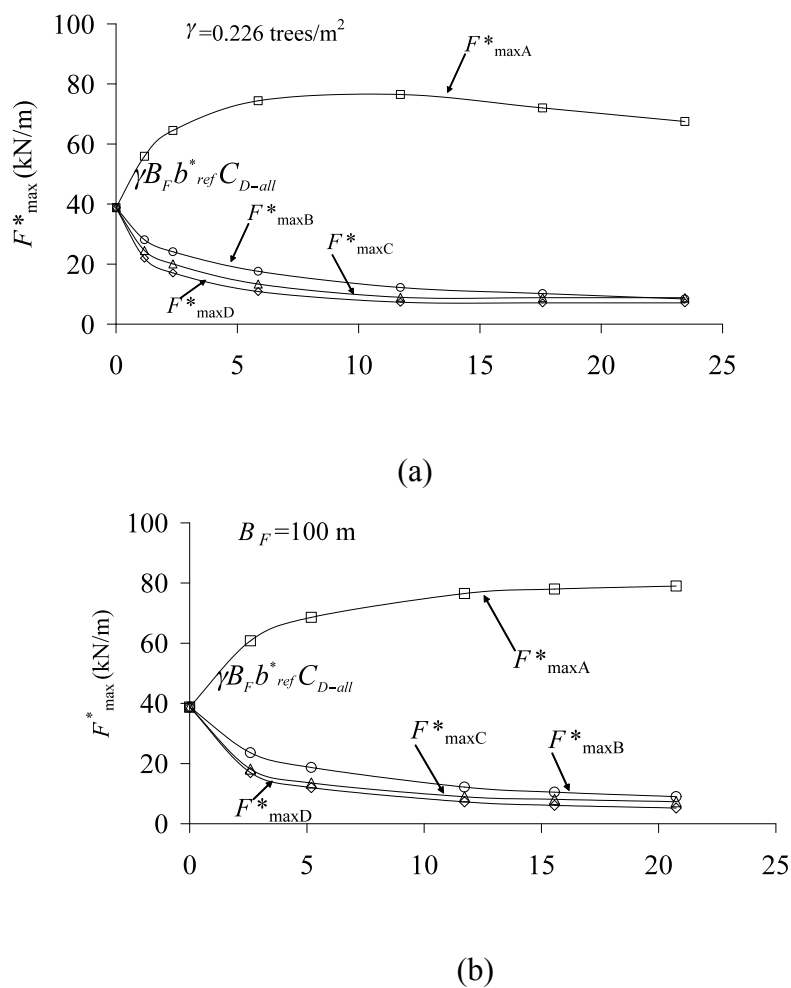
Fig. 14. Variation of tsunami force at A, B, C and D with (a) forest width (Series 1), (b) tree density (Series 2).

Fig. 15 (a) and (b) shows the variations of the representative velocity ($V_{F*\text{max}}$) and total depth ($d_{F*\text{max}}$) at the time of maximum tsunami force together with variations of average maximum discharge fluxes ($\bar{Q}_{in\text{max}}$, $\bar{Q}_{out\text{max}}$, and $\bar{Q}_{side\text{max}}$) against the forest width and the tree density, respectively, where $Q_{in\text{max}}$ and $Q_{out\text{max}}$ are the maximum inflow and outflow at the gap inlet and exit, and $Q_{side\text{max}}$ is the total inflow from both sides to the gap. The over-bar indicates the average discharge flux divided by the gap width. As the width and density increase, the inflow at the gap inlet decreases because of the increase of resistance of forest (in other word, the increase of reflection). In contrast, the outflow at the gap exit is increased slightly at first and does not decrease so much due to the increasing inflow from sides. On the other hand, the inundation depth behind the forest decreases due to the increase of forest resistance. Consequently, the representative velocity at the gap exit increases to result in the increase of tsunami force there. For the change of forest width, however, the point A moves as the forest width increases, while it is fixed in the change of density. Therefore the tsunami force decreases as the forest width becomes considerably wide and reduces to 0 as the forest width reaches to about 1000 m in the present condition.
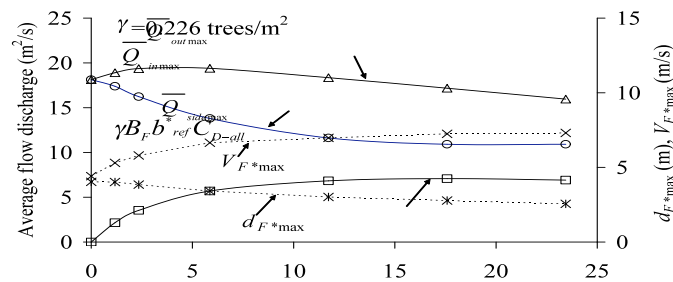
(a)
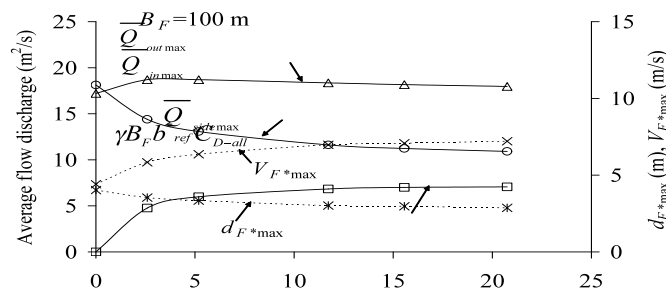
(b)

Fig. 15. Variation of representative water depth, representative velocity and maximum average discharge fluxes against (a) forest width (Series 1), (b) tree density (Series 2).

4.2.3. Effects of incident tsunami conditions

Fig. 16 (a) and (b) shows tsunami forces at four check points and the tsunami force F^*_{max0} in the case of no forest against the incident tsunami height and period. The conditions are B_F=100 m, γ=0.226 trees/m^2, T=1200 s (for the change of tsunami height) and H_{sl0}=6.94 m (for the change of tsunami period). The tsunami force in the case with no forest was taken at D, but it is almost the same with the tsunami force at B in the present forest condition. The tsunami force increases as the incident tsunami height increases. The relationship between the tsunami force and incident tsunami height can be expressed in the form of the following equation:

$$F^*_{max} = a_{Hf}\left(H_{sl0} - H_{cf}\right)^{b_{Hf}}, \quad H_{sl0} \geq H_{cf} \tag{19}$$

where H_{cf} is the threshold incident tsunami height at which the tsunami force becomes 0 and a_{Hf} has a dimension. In the present study, b_{Hf} was fixed as 2, because it may be reasonable to assume that tsunami force is proportional to the second power of the inundation depth and that the inundation depth is proportional to (H_{sl0}-H_{cf}). H_{cf} was also fixed as 2.5 m in the present study after considering the effect on the result and simplicity although, strictly speaking, it is a function of forest condition and tsunami period. The empirical constant of a_{Hf} is given in Fig.16 (a).
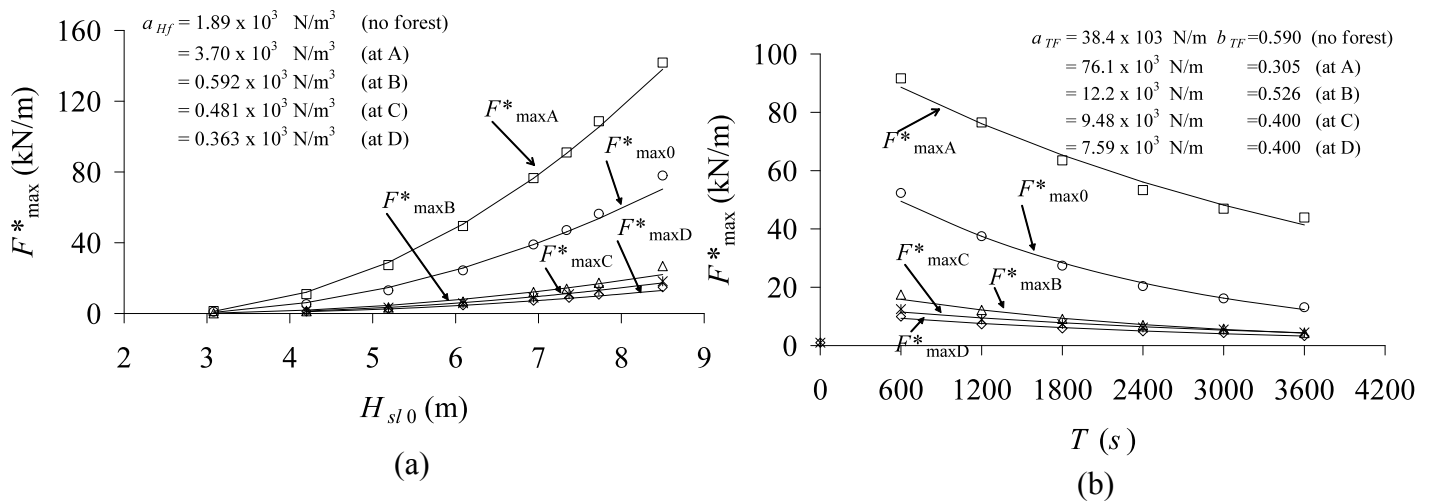
Fig. 16. Tsunami forces against (a) incident tsunami height (Series 3), and (b) tsunami period (Series 4).

On the other hand, the tsunami force decreases as the tsunami period increases in case of the fixed incident tsunami height. The relationship of the tsunami force and the tsunami period can be expressed in the form of the following equation:

$$F^*_{max} = a_{Tf} \exp\left\{-b_{Tf}\left(\frac{T}{T_{rep}} - 1\right)\right\}$$

(20)

where T_{rep} is the representative tsunami period and was taken as 1200 s in the present study, and a_{Tf} has a dimension. The determined empirical constants of a_{Tf} and b_{Tf} are given in Fig.16 (b). Both curve-fit relations against the incident tsunami height and period agree well with numerical results.

4.2.4. Non-dimensional tsunami forces for all simulation results

In the present paper, the following non-dimensional forest thickness combining forest and tsunami conditions is considered:

$$\frac{B_{dNall}}{T_{rep}\sqrt{gH_{rep}}} = \frac{\gamma B_F b^*_{ref} C_{D-all}\left(H_{rep}\right)}{T_{rep}\sqrt{gH_{rep}}}$$

(21)

where $T_{rep}\sqrt{gH_{rep}}$ corresponds to a wavelength of long waves with period of T_{rep} at the depth of H_{rep}. It should be noted, however, that the non-dimensional forest thickness represents the forest condition only, since the tsunami condition is fixed to the representative tsunami condition in Eq.(21). The representative tsunami height H_{rep} is arbitrary as well as the representative tsunami period T_{rep} and was taken as 7 m in the present study.

On the other hand, the tsunami force F^*_{max} is made dimensionless by the following relationship in consideration of the curve-fit equations in 4.2.3 as:

$$\frac{F^*_{max}}{\rho g H_{sl0}^2} = \frac{a_f\left(H_{sl0} - H_{cf}\right)^{Hf} \exp\left\{-b_{Tf}\left(T/T_{rep} - 1\right)\right\}}{\rho g H_{sl0}^2} \frac{F^*_{max\,rep}}{a_f\left(H_{rep} - H_{cf}\right)^{Hf}}$$

$$= \alpha_f f_{Hf} f_{Tf}$$

(22)

where $\rho g H_{sl0}^2$ (unit: N/m) corresponds to double the hydrostatic force acting on a virtual high wall per unit length by inundation depth of H_{sl0}, and $F^*_{max\,rep}$ is the representative tsunami force by incident tsunami with the representative height H_{rep} and arbitrary period T. α_f, f_{Hf} and f_{Tf} are non-dimensional and expressed as follows:

$$\alpha_f = \frac{F^*_{max\,rep}}{\rho g H_{rep}^2} = \frac{F^*_{max}}{f_{Hf} f_{Tf} \rho g H_{sl0}^2}$$

(23)

$$f_{Hf} = \left(\frac{1 - H_{cf}/H_{sl0}}{1 - H_{cf}/H_{rep}} \right)^{b_{Hf}} = 2.42 \left(1 - \frac{2.5}{H_{sl0}} \right)^2 \tag{24}$$

$$f_{Tf} = \exp\left\{ -b_{Tf} \left(\frac{T}{T_{rep}} - 1 \right) \right\} \tag{25}$$

The empirical constant of b_{Tf} at A, B, C and D was determined based on the numerical results as:

$$\left. \begin{aligned} b_{Tf} &= 0.307 + 0.279 \exp\left(-3.13 \times 10^3 \frac{\gamma B_F b^*_{ref} C_{D-all}(H_{rep})}{T_{rep}\sqrt{gH_{rep}}} \right), && \text{at A} \\ &= 0.526, && \text{at B} \\ &= 0.400, && \text{at C and D} \end{aligned} \right\} \tag{26}$$

The empirical constant b_{Tf} at A is given as function of forest condition (B_F and γ), because the relation of tsunami force and forest condition is complex as shown in Fig.14 (a) and (b). The meaning of modification factors will be explained later.

All simulated results of non-dimensional value of α_f in Eq. (22) are plotted against the non-dimensional forest thickness of Eq. (21) in Fig. 17 (a) and (b). As being apprehensible by Eq. (23), f_{Hf} and f_{Tf} are modification factors so that the non-dimensional tsunami force is normalized to the non-dimensional tsunami force due to the incident tsunami with the representative height of H_{rep}. The α_f is called the normalized tsunami force. Due to the changes in tsunami conditions, many data were plotted at the same point on the abscissa, and some data are superimposed.

In Fig. 17(a) and (b), relationships calculated by the following curve-fit equations are shown:

$$\left. \begin{aligned} \alpha_f &= 0.164 - 0.0824 \exp\left(-4.09 \times 10^3 \frac{\gamma B_F b^*_{rep} C_{D-all}(H_{rep})}{T_{rep}\sqrt{gH_{rep}}} \right), && \text{at A} \\ &= 0.0794 \exp\left(-0.0311 \times 10^3 \left[\frac{\gamma B_F b^*_{ref} C_{D-all}(H_{rep})}{T_{rep}\sqrt{gH_{rep}}} \right]^{0.492} \right), && \text{at B} \\ &= 0.0186 + 0.0633 \exp\left(-4.22 \times 10^3 \frac{\gamma B_F b^*_{ref} C_{D-all}(H_{rep})}{T_{rep}\sqrt{gH_{rep}}} \right), && \text{at C} \\ &= 0.0139 + 0.0678 \exp\left(-4.05 \times 10^3 \frac{\gamma B_F b^*_{ref} C_{D-all}(H_{rep})}{T\sqrt{gH_{rep}}} \right), && \text{at D} \end{aligned} \right\} \tag{27}$$
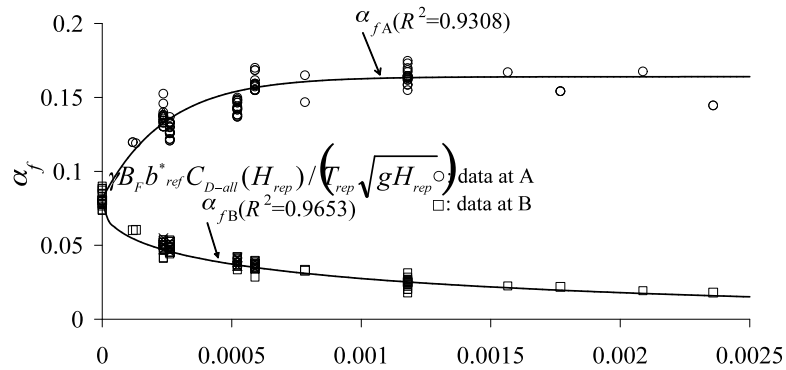
(a)
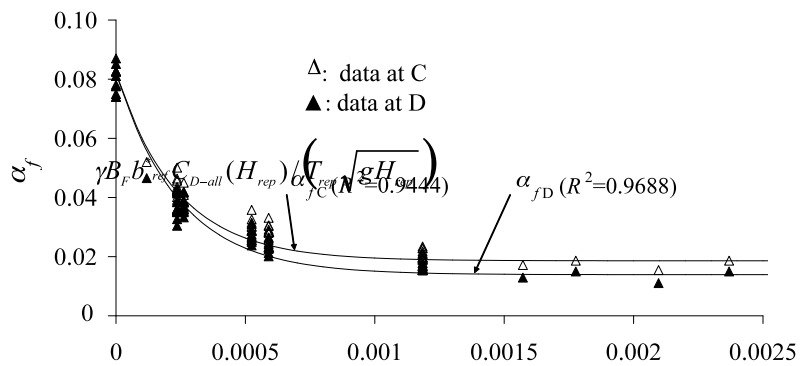
(b)

Fig. 17. Normalized tsunami force against non-dimensional forest thickness, (a) at A and B, (b) at C and D (Series 1-12).

In the figure, the relationships are indicated with the subscript A, B, C and D. Those curve-fit equations represent the average relationship of the non-dimensional tsunami force against non-dimensional forest thickness fairly well although the data are considerably scattered due to variety of conditions.

Fig. 18 shows the correlation of tsunami force at A, B, C and D estimated from the normalized tsunami force by Eq. (27) and tsunami force obtained by a numerical simulation with the absolute values. The agreement is fairly good. In the figure, the relations for $y=1.1x$ and $y=0.9x$ are also shown.

The error was within 10%. Eq. (27) can be applied to calculate tsunami force at A, B, C and D respectively if all information of forest and tsunami conditions are available. Note, however, that α_f at A is effective for the condition of B_F<200 m.
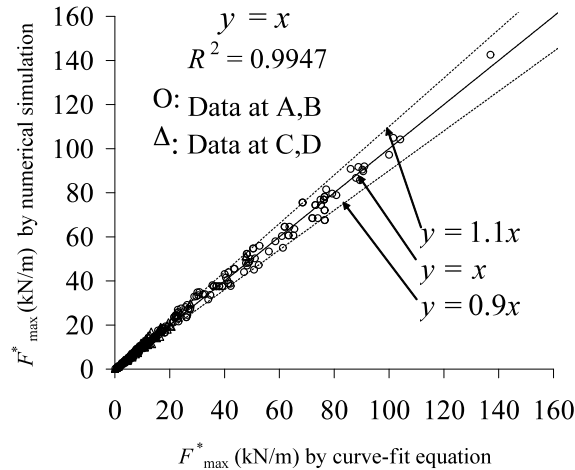
Fig. 18. Correlation of tsunami force by numerical simulations and by curve-fit equation at A, B, C and D (Series 1-12).

5. SUMMARY AND CONCLUSIONS

The summary and conclusions of the present study are as follows:

1. Laboratory experiments were carried out to validate the applicability of numerical model based on two-dimensional nonlinear long-wave equations including drag resistance of trees and turbulence induced shear forces to flow around a simplified forest model with a gap. It was confirmed that the water surface elevation and flow velocity by the numerical simulations agree well with the experimental results for various forest conditions of width and tree density.

2. The numerical model was applied to a prototype scale condition of a coastal forest of *Pandanus odoratissimus* with a gap to investigate the effects of forest conditions (width B_F and tree density γ) and incident tsunami conditions (period T and height at shoreline H_{sl0}) on a potential tsunami force which is defined as the total drag force on a virtual high column with unit width and unit drag coefficient. The potential tsunami force at the gap exit is greatly enhanced due to mainly the inflow to the gap through sides of vegetation patch and the maximum in the spatial distribution around and inside the forest, which reaches to twice of the potential tsunami force in the case of no forest in unfavorable conditions.

3. The potential tsunami forces at four representative points at front and back of forest including the center of gap exit were analyzed for various conditions and formulated as function of forest and tsunami conditions in the non-dimensional form. The potential tsunami forces at the gap exit increases as the increase of forest resistance due to the increase of forest width (B_F<100 m) and tree density, as the incident tsunami height increases and as the tsunami period decreases. The potential tsunami force at other points behind the vegetation patch and the front of forest decreases as the forest resistance increases. The potential tsunami forces calculated by the curve-fit formula in the non-dimensional form agree well with the simulated potential tsunami forces within ±10% error (B_F<200 m).

In the present paper, mature *P. odoratissimus* trees distributed uniformly in a forest were considered. However, tree conditions are not uniform in the actual forest and differ in the growth stage. To investigate the effects of non-uniform distribution of the various growth stages on tsunami forces is an exciting subject to be studied. Further, including the breaking of trees in numerical simulations is another subject of future study, as well as verification of the method of numerical simulations including tree breaking by field data.

REFERENCES
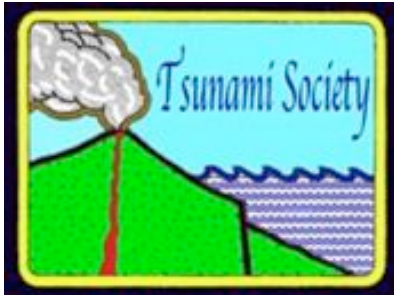
Chakrabati, SK., 1991. Wave force on offshore structures. In: J.B. Herbich, Editor, Handbook of Coastal and Ocean engineering, Vol. 2 (1991), pp. 1-54.

Danielsen, F., Sorensen, M.K., Olwig, M.F., Selvam, V., Parish, F., Burgess, N.D., Hiraishi, T., Karunagaran, V.M., Rasmussen, M.S., Hansen, L.B., Quarto, A., Suryadiputra, N., 2005. The Asian tsunami: A protective role for coastal vegetation. Science 310, 643.

Fernando, H.J.S., Samarawickrama, S.P., Balasubramanian, S., Hettiarachchi, S.S.L., Voropayev, S., 2008. Effects of porous barriers such as coral reefs on coastal wave propagation. Journal of Hydro-environment Research 1, 187-194.

Harada, K., Imamura, F., 2005. Effects of coastal forest on tsunami hazard mitigation – A preliminary investigation, Tsunamis: Case studies and Resent Development, ed. K. Satake (Advances in natural and Technological Hazards Research, Springer) pp. 279-292.

Imamura, F., Shuto, N., Goto, C., 1998. Numerical simulation of the transoceanic propagation of tsunami. Proceedings of paper presented at the Sixth Congress of the Asian and Pacific Regional Division, Int. Assoc. Hydraul. Res., Kyoto, Japan.

Kathiresan, K., Rajendran, N., 2005. Coastal mangrove forests mitigated tsunami. Estuarine, Coastal and Shelf Science 65, 601-606.

Kerr, A.M., Baird, H.B., 2007. Natural barriers to natural disasters. BioScience. 57(2), 102-103.

Koh, H.L., Tek, S.Y., Liu, P.L., Ismail, A.I., Lee, H.L., 2008. Simulation of Andaman 2004 tsunami for assessing impact on Malaysia. Journal of Asian Earth Sciences 36, 74-83.

Liu, P.L., Cho, Y.S., Yoon, S.B., Seo S.N., 1994. Numerical simulations of the 1960 Chilean tsunami propagation and inundation at Hilo, Hawaii. In: M.I. El-Sabh, Editor, Recent Development in Tsunami Research, Kluwer Academic Publishers (1994), pp. 99–115.

Mascarenhas, A., Jayakumar, S., 2008. An environmental perspective of the post-tsunami scenario along the coast of Tamil Nadu, India: Role of sand dunes and forests. Journal of Environmental Management 89, 24-34.

Nadaoka, K., Yagi, H., 1998. Shallow-water turbulence modeling and horizontal larger eddy computation of river flow. Journal of Hydraulic Engineering 124(5), 493-500.

Nandasena, N. A. K., Tanaka, N., Tanimoto, K., 2008. Perspective of coastal vegetation patches with topography variations for tsunami protection in 2D-numerical modeling. Annual Journal of Hydraulic Engineering, JSCE 52, 133-38.

Shuto N., 1987. The effectiveness and limit of tsunami control forests. Coastal Engineering in Japan. 30(1), 143-153.

Tanaka, N., Sasaki, Y., Mowjood, M.I.M., Jinadasa, K.B.S.N., 2007. Coastal vegetation structures and their functions in tsunami protection: Experience of the recent Indian Ocean tsunami. Landscape and Ecological Engineering 3, 33-45.

Tanaka, N., 2009. Vegetation bioshields for tsunami mitigation: review of the effectiveness, limitations, construction, and sustainable management. Landscape and Ecological Engineering 5, 71-79.

Tanaka, N., Nandasena, N. A. K., Jinadasa, K. S. B. N., Sasaki, Y., Tanimoto, K. Mowjood, M. I. M., 2009. Developing effective vegetation bioshield for tsunami protection. Journal of Civil and Environmental Engineering Systems 26, 163-180.

Thuy, N.B., Tanimoto, K., Tanaka, N., Harada K., Iimura, K., 2009a. Effect of open gap in coastal forest on tsunami run-up – Investigations by experiment and numerical simulation. Ocean Engineering 36, 1258-1269.

Thuy, N.B., Tanaka, N., Tanimoto, K., Harada K., Iimura, K., 2009b. Tsunami flow behind the coastal forest with an open gap-effects of tsunami and tree condition. Proceedings of the 6th International Conference on Coastal Dynamic, Tokyo-Japan (CD-Rom). DOI No: 10.1142/9789814282475_0050

Titov, V.V., Synolakis, C.E., 1997. Extreme inundation flows during the Hokkaido Nansei-Oki tsunami. Geophys. Res. Lett. 24(11), 1315-1318.

TSUNAMI HAZARD AND TOTAL RISK IN THE CARIBBEAN BASIN

X. William Proenza
National Oceanic and Atmospheric Administration
National Weather Service
Fort Worth, Texas 76102

and

George A. Maul
Florida Institute of Technology
Department of Marine and Environmental Systems
Melbourne, Florida 32901

ABSTRACT

Deadly western North Atlantic Ocean tsunami events in the last centuries have occurred along the east coast of Canada, the United States, most Caribbean islands, and the North Atlantic Coast of South America. The catastrophic Indian Ocean tsunami of 2004 reminded natural hazards managers that tsunami risk is endemic to all oceans. *Total Risk* is defined as *hazard* (frequency of tsunami events) times measures of *elements at risk* (human exposure) times measures of *vulnerability* (preparedness) in a given epoch (Nott, 2006). While the tsunami *hazard* in the Caribbean (averaging 19 ± 22 years between deadly events) is lower than Pacific coastal areas, the *total risk* to life and property is at least as high as the USA West Coast, Hawaii, or Alaska, because of the higher Caribbean population density and beach tourism so attractive to more than 35 million visitors a year. Viewed in this light, the allocation of resources by governments, industry, and insurers needs to be adjusted for the better protection of life, for coastal engineering, and for infrastructure.

INTRODUCTION

Atlantic tsunami hazard and risk have been of major concern to the Subcommission for the Caribbean and Adjacent Regions (IOCARIBE) of the Intergovernmental Oceanographic Commission (IOC) of UNESCO and the United Nations Environment Programme's Caribbean Environment Programme since they co-sponsored a workshop on Small Island Oceanography in 1993 (Maul, 1996). IOCARIBE has been proactive in creating a tsunami warning system for the Intra-Americas Sea since the 1993 Martinique workshop, although the Atlantic hazard has been well recognized for many years (Bryant, 1991, 2005; Smith and Shepherd, 1993; Watlington and Lincoln, 2001; Ruffman, 2001; O'Loughlin and Lander, 2003 amongst others). Gonzalez (1999) doesn't mention the Atlantic, nor the Caribbean Sea in particular, in his writing (see the many pre-1999 references in Lockridge *et al.,* 2002).

Caribbean Sea tsunami events have been recorded since the coming of European explorers in the 15th century. Table 1, extracted from O'Loughlin and Lander (2003) and UNESCO (2010), summarizes the major deadly events from 1498 to the present. There are n = 26 events in the last 500+ years wherein drownings are reported or are very probable, and many more tsunamis where deaths are not reported or simply not recorded. On average, the time difference (Δt) between tsunami-related drowning events is 19 ± 22 years (± one standard-deviation). The frequency distribution of Δt is positively skewed (Figure 1), and suggests that one event is likely to have another close in time followed by a much longer Δt until the next event. The two tsunamis in the Dominican Republic in 1946 where 1,790 persons died one day, and four days later another tsunami claimed 75 more souls, is an example of such a statistical distribution.

Frequency of Occurrence

	0	10	20	30	40	50	60	70	More
Frequency	2	10	7	1	2	1	2	0	1

Time between Events (Δt)

Number of Tsunami
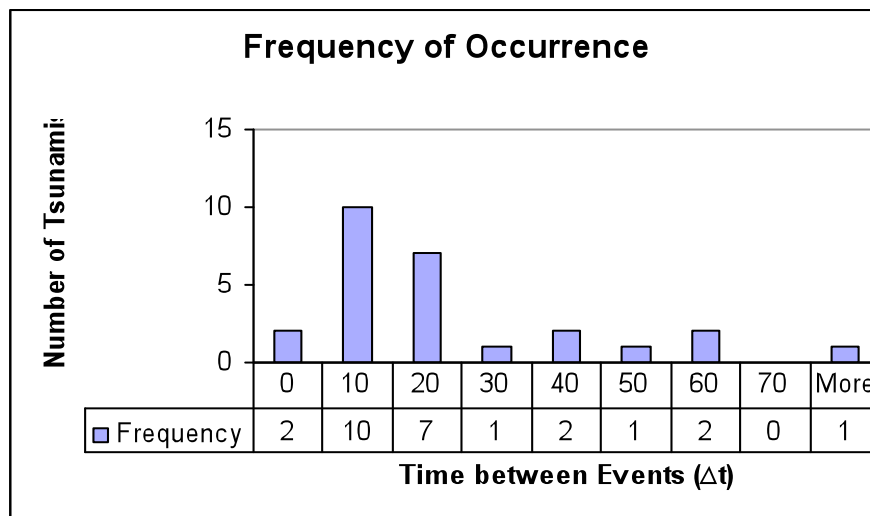
Figure 1: Frequency distribution of death-causing tsunamis in the Caribbean Sea since 1498. Frequency upper row labeled "10" includes all events $1 \le \Delta t \le 10$ years; upper row "20" includes all $11 \le \Delta t \le 20$ years, etc.

As IOCARIBE matured in its appreciation of the tsunami hazard, efforts to encompass the entire western Atlantic Ocean began to emerge (Maul, 2003; Mercado and Liu, 2006). IOCARIBE created a Tsunami Steering Group of Experts in 1995, and there have been annual meetings since. The parent body of IOCARIBE, the IOC, raised the level of attention to that in the Pacific and Indian Oceans in 2006 by creating an Intergovernmental Coordinating Group (ICG) for the Caribbean (and another ICG for the Indian Ocean) that is on a level with the ICG for the Pacific (called "ITSU"). Thus the IOC, the international agency responsible for tsunami warnings and information, is actively engaged in developing mechanisms to prevent a repeat of the horrific event of 2004, yet Teeuw *et al.* (2009) make no mention of the Caribbean IGC.

Table 1: Summary of death-causing tsunamis in the Caribbean Sea

Year	Location	Notes
1498	Venezuela	Opened Gulf of Cariaco
1530	Venezuela	Affected entire north coast of South America
1543	Venezuela	City of Cumaná destroyed
1599	Venezuela	Cumaná; frequent inundations by the sea over the low shore
1690	Virgin Islands	Deaths in Antigua, Guadalupe, and St. Kitts
1692	Jamaica	Port Royal 1,000-2,000 drown
1751	Dominican Republic	Town of Azua de Compostela destroyed
1751	Haiti	Part of Port-au-Prince submerged
1755	Lesser Antilles	Lisbon Tele-tsunami; deaths in Saba and Martinique
1761	Barbados	Tele-tsunami from same region as 1755 Lisbon event
1770	Haiti	The sea inundated 7 km onto the shore
1775	Hispaniola and Cuba	Great damage from waves at Haiti and Cuba
1780	Jamaica	Savanna-la-Mar swept away by 3 m wave; 300-1,000 deaths
1812	Venezuela	Exceptional rise of the sea at La Guaira; 3,000 killed
1822	Nicaragua	Punta Chica lagoons dried, canoes left dry
1842	Haiti	Port-de-Paix, 200-300 perished; 2-3 m tsunami
1853	Venezuela	Loss of life in Cumaná area estimated between 600-4,000
1856	Honduras	Criba Lagoon bottom dry
1867	Danish West Indies	Loss of life was probably great; 23-50 dead in USVI
1882	Panama	San Blas coast; 75-100 drowned
1902	Martinique	Dead bodies floated singly and in groups
1906	Venezuela	Death toll estimated at 500 victims
1907	Jamaica	Port Royal; submarine cable broken in three places
1918	Puerto Rico	Aguadilla and Mayaguez; 116-140 dead
1946	Dominican Republic	Matancitas coast; approximately 1790 killed
1946	Dominican Republic	Sabana la Mar; 75 perished
1991	Costa Rica	At Moin the sea withdrew 200 m; 2 drowned at El Matina
2010	Haiti	Petit Paradis; 3 m wave; at least 7 drownings

RISK ASSESSMENT

Whitmore *et al.* (2009) discuss Atlantic tsunami risk primarily in the context of probability of occurrence. Risk assessment is a complex process that is much more than simply calculating the probability of occurrence such as that from Table 1 with Δt summarized in Figure 1. Nott (2006) explains the issue of risk by defining *Total Risk* as follows:

Total Risk = Hazard x Elements at Risk x Vulnerability

where *Hazard* is the frequency of occurrence, *Elements at Risk* measures population, infrastructure, and economies that would be affected by an event, and *Vulnerability* measures societal attitudes and preparedness. Using this approach, a clearer understanding emerges for the possibility of a major catastrophe in the wider Caribbean and other ocean basins.

Three cases of *Total Risk* for the Caribbean are investigated: a tele-tsunami such as the 1755 Lisbon event which sent waves across the Atlantic to the Americas; a comparison with Hawaii (a similar climate and, as with the Caribbean, at risk from tele-tsunami as well as near-field events); and with a cold climate, Alaska. The results are given in Tables 2, 3, and 4 respectively. Data for estimating *Elements at Risk* is gleaned from tourism databases (*e.g.* CTO, 2010) and governmental reports, which often are unofficial, but the only sources available (according to the Caribbean Tourism Organization, there were 17,919,000 stop-over arrivals in 2009, and 17,210,000 cruise passenger arrivals in 2009). *Vulnerability* can be judged in part by the number of Tsunami-Ready communities in a given area.

In Table 2, the coasts of California, Oregon, and Washington are compared with the Caribbean region for tsunami *Hazard* and for *Total Risk*. The Lisbon event of 1755 (Mader, 2004) is used as the Atlantic event that might be compared with the Chilean event of 1960 in the Pacific. Certainly the statistics (*cf.* Bryant, 2005) support that the *Hazard* to the USA Pacific states is substantially higher than that for the Caribbean. However, factoring in the much higher beach population on any given day in the Caribbean (*Elements at Risk*) and the lack of Tsunami-Ready communities (*Vulnerability*), the *Total Risk* is estimated to be at least as high or higher for the Caribbean and its peoples than for the United States west coast partly due to the warm water draw of the Caribbean Sea over the cold upwelling waters of the Pacific States.

Table 2: Comparison of the *total risk* from a tele-tsunami in the northeastern Pacific Ocean and in the Caribbean Sea.

	Frequency of Occurrence	Water Temperature	Daily Beach Attendance	Impact with 10% Loss of life	Hazard	Total Risk
Caribbean Region	1/250 years	Warm	500,000	20,000 per Century	Low	Very High
West Coast USA	1/50 years	Cold	40,000	4,000 per Century	High	High

Hawaii as a state is well prepared for tsunamis with many Tsunami-Ready communities, beachfront sirens to warn swimmers and sunbathers, and political appreciation of the risk (Bernard, 2005). The Tsunami Warning System in the Pacific (ITSU) is headquartered in Oahu and the warning system has been operational for over half a century. While Hawaii is at risk from tele-tsunami (*cf.* Table 2) it also is at risk from locally generated events. As a comparison to the Caribbean, consider the case of the (now) US Virgin Islands which had a 6 meter wave sweep into St Thomas and into St. Croix minutes after the 1867 earthquake in the Anegada Passage (Watlington and Lincoln, 2001). In Table 3 the *Hazard* and the *Total Risk* for the Caribbean and for Hawaii are compared, and it is seen that the *Total Risk* for the Caribbean is higher than for Hawaii not only due to larger beach attendance (*Elements at* Risk), but to the much higher *Vulnerability* due to lack of preparedness and warning infrastructure.

Table 3: Comparison of the *total risk* from a local tsunami in Hawaii and in the Caribbean Sea.

	Frequency of Occurrence	Water Temperature	Daily Beach Attendance	Impact with 10% Loss of life	Hazard	Total Risk
Caribbean Region	1/20 years	Warm	500,000	50,000 per Century	High	Very High
Hawaii	1/25 years	Warm	100,000	40,000 per Century	High	Very High

Alaska is the site of the United States' second tsunami warning center, with responsibility to warn all states in the Pacific except Hawaii and (Whitmore *et al.,* 2009), as an interim to a Caribbean Tsunami Warning Center, the east coast of the USA including Puerto Rico and the US Virgin Islands. The *Hazard* to Alaska is high due to the proximity of the Aleutian Trench subduction zone, but it is a cold-water environment compared to say Puerto Rico. The Puerto Rico Trench is seismically active and was the source of deadly waves for Puerto Rico in 1918 and the Dominican Republic twice in 1946 (Lockridge *et al.,* 2002; O'Loughlin and Lander, 2003) in the last century (*cf.* Table 1). As with most Pacific-coast communities, Alaska is well-prepared for a tsunami, and to a lesser extent, so is Puerto Rico and the US Virgin Islands (Mercado-Lrizarry and Liu, 2006). Clearly the *Hazard* in Alaska (Table 4) is higher than Puerto Rico, but equally clear is that the *Total Risk* to the Caribbean is much higher due to the *Elements at Risk* and the *Vulnerability*.

Table 4: Comparison of the *total risk* from a local tsunami in Alaska and in the Caribbean Sea.

	Frequency of Occurrence	Water Temperature	Daily Beach Attendance	Impact with 10% loss of life	Hazard	Total Risk
Caribbean Region	1/20 years	Warm	500,000	50,000 per Century	High	Very High
Alaska	1/25 years	Very Cold	5,000	2,000 per Century	High	High

DISCUSSION

The Caribbean Sea and its environs are tsunami hazard zones (*cf.* Table 1) due to near-field events (*e.g.* Dominican Republic in 1946), subaerial landslides (*e.g.* Montserrat in 1998), submarine volcanoes (Smith and Shepherd, 1993), and tele-tsunami (*e.g.* Lisbon in 1755); submarine slumping and subaerial volcanoes add to the potential for death-causing tsunami (Mercado- Lrizarry and Liu, 2006). Knowledgeable local residents even have a term for it: "El Peligro Olvidado" The Forgotten Danger! The NOAA National Weather Service has taken action by assigning the Pacific Tsunami Warning Center in Hawaii to issue warnings for our Caribbean neighbors to Puerto Rico and the US Virgin Islands, but no local warning center is yet funded to holistically address all aspects of the danger (education, warning, management, and research (Maul, 2003)).

Analyzing *Total Risk* (Nott, 2006) as the product of probability of occurrence (*Hazard*) times population and other *Elements at Risk*, times preparedness and political awareness (*Vulnerability*), it is seen that the Caribbean tsunami danger is Very High in all three cases analyzed: tele-tsunami (Table 2), Hawaii comparison (Table 3), and Alaska comparison (Table 4). While the *Hazard* in the Caribbean is one death-causing event every 19 years on average (based on about 500 years of data), the statistical distribution (19 ± 22 years) has high positive skewness (*cf.* Figure 1). Skewness suggests that one or more events have occurred close together and then there is a long time (Δt) before the next event. Using the very deadly tsunami in the Dominican Republic of 1946 as a guide, there are in 2010, +2.9 standard deviations in Δt since the last multihundred-death event. Thus the *Hazard* of a death-causing Caribbean tsunami in the near future is high and the *Total Risk* is very high.

High *Total Risk* coupled with the increasing coastal population (Duedall and Maul (2005) estimated that the coastal population of the North Atlantic for 2025 is 40 million more persons above that in 2000, and mostly in the Caribbean and North Africa) further increases the *Elements at Risk*. That, coupled with lack of awareness and political inaction, increases the *Vulnerability*. The stage seems set for a catastrophe of unimaginable proportions that humankind experienced in the 2004 event in all its horror. Since 2004, there has been another global disaster. This time in the Caribbean country of Haiti where an earthquake on January 12, 2010, killed more than 200,000 people. Had the earthquake been more tsunamigenic, the death toll (6 or 7 persons drowned) would have been even more horrific.

Depending upon tsunami warnings from half a world away, further increases *Total Risk* from lack of local expertise, cultural knowledge, language, and a presence that demonstrates regional commitment to safeguarding the lives and property of inhabitants and visitors in the Caribbean.

CONCLUSIONS

The Indian Ocean and the southwestern North Atlantic Basin have much in common besides warm waters and similar low-lying coastal topography. The NOAA Geophysical Data Center reports that the Caribbean Basin has had 8% of the world's tsunami events (*cf.* Bryant (2005) who reports 13.8%), and the Indian Ocean, 7% (Bryant reports 0.8 % for the Bay of Bengal). Yet an Indian Ocean tsunami on December 26, 2004 caused well over 250,000 deaths by drowning. The Caribbean has had 6 times more deaths in the last 168 years than Alaska, Hawaii, Washington, Oregon, and California combined

(O'Loughlin and Lander, 2003). With numerous close-field tsunamigenic sources, the Caribbean has dire need of a local-expertise Tsunami Warning Center with multi-national (thirty three independent states), trilingual (English, French, and Spanish) preparedness to best assure protection of life and property. Anything less will lead to unnecessary loss of life and worldwide criticism.

The views expressed are those of the author(s) and do not necessarily represent those of NOAA.

REFERENCES

Bernard, E.N. (editor). *Developing Tsunami-Resistant Communities*, the National Tsunami Hazard Mitigation Program. ©Springer, Dordrecht, 184 pp., 2005.

Bryant, E.A. *Natural Hazards,* 2nd edition. ©Cambridge University Press, Cambridge, New York, Melbourne, 312 pp., 2005.

CTO (Caribbean Tourism Organization). Latest Statistics, 2009. CTO_MAY6Lattab09.pdf, April 27, 2010.

Duedall, I.M., and G.A. Maul. Future Coastal populations. In: M. Schwartz, (editor), *Encyclopedia of Coastal Science*, ©Kluwer Academic Publishers, Dordrecht, pp: 368-374, 2005.

Gonzalez, F.I. Tsunami! *Scientific American*, 280(5): 56-65, 1999.

Lockridge, P.A., L.S. Whiteside, and J.F. Lander. Tsunamis and Tsunami-Like Waves of the Eastern United States. *Science of Tsunami Hazards*, 20(3): 120-157, 2002.

O'Loughlin, K.F., and J.F. Lander. *Caribbean Tsunamis: a 500-year history from 1498-1998*. ©Kluwer Academic Publishers, Dordrecht, Boston, 263 pp., 2003.

Mader, C.L. Modeling the 1755 Lisbon Tsunami. *Science of Tsunami Hazards*, 19(2): 93-99, 2004.

Maul, G.A., (editor). *Small Islands: Marine Science and Sustainable Development.* © American Geophysical Union, Coastal and Estuarine Studies No. 51, Washington, 476 pp., 1996.

Maul, G.A. Atlantic Tsunami Warnings Are Needed. Guest Editorial, *Sea Technology*, 44(3), pp: 7, 2003.

Mercado-Lrizarry, A. and P. Liu (editors), *Caribbean Tsunami Hazard - Proceedings of the National Science Foundation Caribbean Tsunami Workshop*, World Scientific Publishing, Co., Singapore, 341 pp., 2006.

Nott, J. *Extreme Events – Physical Reconstruction and Risk Assessment*, ©Cambridge University Press, Cambridge, 297 pp., 2006.

Ruffman, A. Comment on "Potential for large-scale submarine slope failure and tsunami generation along the U.S. mid-Atlantic coast: comment". *Geology*, 29, pg. 967, 2001.

Smith, M.S., and J.B Shepherd. Preliminary investigations of the tsunami hazard of Kick'em Jenny submarine volcano. *Natural hazards*, 7: 257-277, 1993.

Teeuw, R., D. Rust, C. Solana, C. Dewdney, and R. Robertson. Large Coastal Landslides and Tsunami Hazard in the Caribbean. *EOS*, Transactions, American Geophysical Union, 90(10): 81-82, 2009.

UNESCO Tsunami and other Coastal Hazards Warning System for the Caribbean and Adjacent Regions (CARIBE EWS) 12 January 2010 Haiti Earthquake and Tsunami Event Post-Event Assessment of CARIBE EWS Performance, IOC Information Series No. 90, 2010.

Watlington, R.A., and S.H. Lincoln. *Disaster and Disruption in 1867: Hurricane, Earthquake, and Tsunami in the Danish West Indies*. ©University of the Virgin Islands, St. Thomas, USVI 00803, 134 pp., 2001.

Whitmore, P., U. ten Brink, M. Caropolo, V. Huerfano-Moreno, W. Knight, W. Sammler, and A. Sandrik. NOAA/West Coast and Alaska Tsunami Warning Center Atlantic Ocean Response Criteria. *Science of Tsunami Hazards,* 28(2): 86-107, 2009.

OPTIMAL LOCATION OF TSUNAMI WARNING BUOYS AND SEA LEVEL MONITORING STATIONS IN THE MEDITERRANEAN SEA

Layna Groen, Anthony Joseph, Eileen Black, Marianne Menictas, Winson Tam, Mathew Gabor
Department of Mathematical Sciences,
University of Technology,
PO Box 123 Broadway, Sydney, NSW
AUSTRALIA

ABSTRACT

The present study determines the optimal location of detection components of a tsunami warning system in the Mediterranean region given the existing and planned infrastructure. Specifically, we examine the locations of existing tsunameters DART buoys and coastal sea-level monitoring stations to see if additional buoys and stations will improve the proportion of the coastal population that may receive a warning ensuring a timely response. A spreadsheet model is used to examine this issue. Based on the historical record of tsunamis and assuming international cooperation in tsunami detection, it is demonstrated that the existing network of sea level stations and tsunameters enable around ninety percent of the coastal population of the Mediterranean Sea to receive a 15 minute warning. Improvement in this result can be achieved through investment in additional real-time, coastal, sea level monitoring stations. This work was undertaken as a final year undergraduate research project.

Key words: tsunami warning system, spreadsheet modelling, optimal location.

1. INTRODUCTION

The historic record documents that numerous large destructive earthquakes and tsunamis have occurred from antiquity to the present in the Mediterranean Sea. The record goes as far back as 1628 BC when an ultra-Plinian explosion of the Santorin volcano in the Aegean Sea and the subsequent collapse of its caldera generated tsunami waves that reached up to 60 meters in height. The waves generated by this explosion/collapse and subsequent flank failures of the volcano are believed to have contributed to the destruction of the Minoan empire and civilization (Pararas-Carayannis, 1973, 1974, 1992). On July 21, 365 A.D., a great earthquake with magnitude estimated at 8.3 near the west coast of the island of Crete generated a catastrophic tsunami that was responsible for extensive destruction on Crete, Peloponnese, Eastern Sicily, Cyprus, Northern Africa, Egypt and elsewhere. The historical accounts indicate that as many as 50,000 people lost their lives in Alexandria alone. The combined catastrophic impacts of the earthquake and of the tsunami, are believed to have been a significant catalyst in the declination of the Roman Empire and its subsequent division between the East and the West (Byzantine) in 395 A.D. (Pararas-Carayannis & Mader, 2010). On October 1790, a destructive earthquake occurred near Oran city in the western part of Algeria generated a tsunami that inundated the Spanish and North Africa coasts (Amir and Cisternas, 2010).

Tsunami activity in the region has continued to the present. For example, the earthquake of 17 August 1999 in Turkey generated a destructive earthquake in the Gulf of Izmit and the Marmara Sea. The combined effects of the earthquake and tsunami were responsible for about 17,000 deaths of people and thousands of injuries. (Tsunami Institute 2009). On the Western Mediterranean, a tsunami near the Algerian coast in May 2003, "destroyed over 100 boats on Mallorca and flooded Palmas Paseo Maritimo" (Tsunami Institute 2009).

The ongoing complex interactive tectonic activity raises questions about the recurrence of another great tsunamigenic earthquake and its potential impact in the Eastern Mediterranean region (Pararas-Carayannis & Mader, 2010). The University of Cambridge notes that "the fault near Crete is accumulating strain energy " and that subsequent earthquakes could result in another tsunami having a catastrophic impact on the more populated coastal cities of the Eastern Mediterranean region (University of Cambridge 2009).

Figure 1 shows the shows source regions in the Mediterranean Sea that generated destructive tsunamis, dating back to 1628BC. Apparently all coastal regions in both the Eastern and Western Mediterranean are vulnerable to tsunamis generated from distant as well as local earthquakes. However, the record indicates that the west coast of Greece and coastal areas bounding the Aegean Sea, have the highest vulnerability. In spite of the high risk, vulnerability and high probability for the generation of destructive tsunamis, no tsunami warning system exists presently in the region (Belfast Telegraph 2009; Westall, 2008), although an implementation plan has been proposed (ICG/NEAMTWS-III 2007).

The present study investigates the best configuration of existing and new tsunami warning detectors that are needed – DART buoys and sea level monitoring stations – to maximise the effectiveness of an early warning system that could alert promptly the maximum number of people in the region of an impending tsunami. The potential performance of such as system is evaluated, based on the established historical records of tsunamis in the region.

In the following sections, we first provide a brief background of the problem as well as an outline of previous work in determining the optimal locations for the placement of tsunami detectors. Subsequently, we present an approach that can be used to assess the effectiveness of the current and expanded detector placement configurations. We then describe the data and solution approach and present the results and analysis of the current and expanded configurations. Included in the analysis is a brief discussion on the sensitivity of our results to different tsunami wave travel times and response times. We conclude the paper with a discussion of our findings.
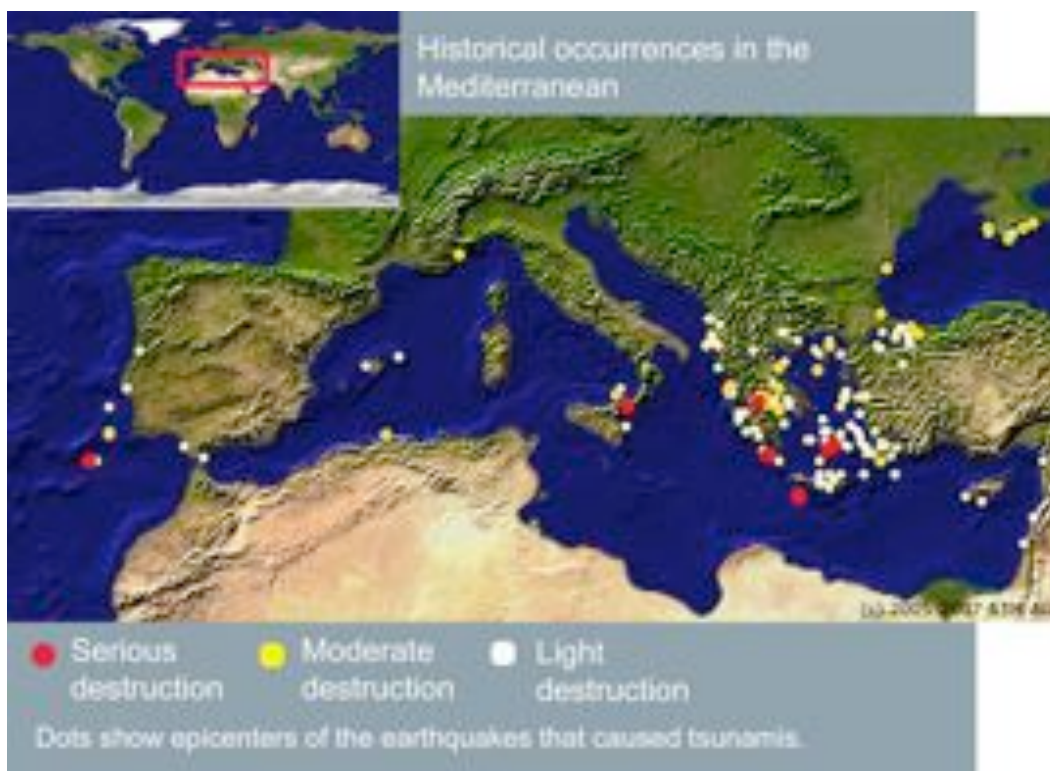
Figure 1 – Historical occurrences of Tsunamis in the Mediterranean Sea
Image Source: (Tsunami Institute 2009)

2. BACKGROUND

The seismotectonics of the Mediterranean region are dominated by the collision of Eurasia, Africa and Arabia plates and of two microplates - the Anatolian and the Aegean (Pararas-Carayannis & Mader 2010). A number of plate boundaries occur in the Mediterranean – a subduction zone runs east from Sardinia, across the southern extremity of Italy along the southwestern coast of Greece and across the Aegean Sea towards Israel. Transform faults are also associated with the Anatolian and the Aegean microplates in the eastern Mediterranean region. The majority of tsunami sources in the Mediterranean are associated with these plate boundaries (Figure 1).

Current tsunami warning systems (TWSs) make use of seismographic recordings to detect the occurrence of earthquakes, volcanic eruptions, detonations of nuclear devices at sea, or underwater explosions (ITIC 2005). However, not all such events generate tsunamis. Given that unnecessary large-scale evacuations are costly and disruptive, it is necessary to confirm whether a potentially destructive tsunami has been generated by supplementing the seismic data with data on sea level changes at coastal tide gauge stations as well pressure fluctuations recorded on sensors on the sea floor.

Tsunami waves have long periods so that changes in hydrostatic pressure can be detected on the sea floor by an anchored seafloor bottom pressure recorder (or tsunameter) and a companion moored surface buoy for real-time communications (National Data Buoy Centre 2009). The surface buoy relays information between the tsunameter and a satellite network using an Iridium transceiver. The Iridium Satellite Network is a worldwide system capable of transmitting tsunami alerts throughout the Mediterranean quickly and efficiently. DART buoy data are then used to confirm the generation of a tsunami and to predict the tsunami hazard for locations where the waves will probably strike.

Coastal sea level gauges nearest the tsunami source are frequently destroyed by the waves. However, this action by itself is indicative that a destructive tsunami has been generated. Where coordination of information via a communication network component of a tsunami warning system exists, events at coastal sea-level monitoring stations can be used to provide warning to other coastal communities (Audet et al. 2008). Thus, the combination of coastal tide stations and DART buoys provide real-time sea level data that confirms tsunami generation and thus form the backbone of the detection component of tsunami warning systems.

3. MEASURING THE PERFORMANCE OF A TSUNAMI WARNING SYSTEM

The present paper examines the effectiveness of the current detection infrastructure (tsunami warning buoys and sea level monitoring stations) that may be employed as part of the proposed tsunami warning system for the coastal regions of the Mediterranean Sea. The measure of performance used in this analysis is the proportion of the coastal population that can receive a timely warning of the arrival of a tsunami, called the warning potential. This potential first appears in Braddock and Carmody (2001), where the concept was applied to the measurement of performance of an augmented tsunami warning system for the Pacific Ocean. Here, we modify their definition slightly to reflect the relative frequency of tsunamis generated.

In order to determine the warning potential for a particular tsunami, we must make a small number of time calculations. These include: a) the time taken by the tsunami to travel from the generation point to the population centre; b) the time taken by the tsunami to travel from the generation point to the nearest detector; and c) the time taken for the detection site to communicate with the warning centre and the population and a response to be undertaken. This latter time sum (b+c) must then be less than the tsunami travel time for a timely warning to be effectively issued. Populations potentially issued a timely warning are then summed and the proportion of the total population that could have been warned constructed (details follow). This is the warning potential.

To solve this problem, let the index set of detection sites (buoys and sea-level stations) be denoted $w =1, \ldots, W$, where W describes the total number of detection sites. Let the index set for tsunami generation points (based on the historical record) be denoted by $u =1, \ldots, U$, where U represents the total number of generation points. Let the index set for the population centres be $v =1, \ldots, V$ and P_v denote the population size. We use population size as a proxy for the number of people that may be affected by a tsunami as the actual population at risk depends on the height of the tsunami and the geography of the population centre. The time taken for the tsunami to travel to each population centre will be represented by $t_{u,v}$.

The first component in determining the time taken for a warning to reach a population centre is the time taken by the tsunami generated to reach a detection site. Let $t_{u,w}$ be this time. Let $t_{w,d}$ be the processing and transmission time to confirm the detection of a tsunami ($t_{w,d}$ will depend on whether the detector is a sea level station or a DART buoy). We define $t_w = t_{u,w} + t_{w,d}$ as the total time taken to issue a warning from the detection site at w for a tsunami generation point, u. The minimum value of t_w across all detection sites would then be the time taken to issue a tsunami warning for tsunami generation u. We denote this minimum time by $t_w{}^*$. It follows that the population at v will be provided with a timely warning as long as $t_w{}^* + r_v < t_{u,v}$, where r_v is the response time of the population at v.

The warning potential for a population centre v, for a tsunami generated at u is

$$
p_{u,v} = \begin{cases} 0, & t_w{}^* + r_v \geq t_{u,v} \\ P_v, & t_w{}^* + r_v < t_{u,v} \end{cases}
\tag{1}
$$

That is, if timely warning is not received $p_{u,v}$ takes the value of 0, while if a population can receive a timely warning, the size of the population is taken. The warning potential for a given tsunami generation point is then calculated by summing the warning potentials for all population centres and standardising over the total population of all centres. That is, the warning potential for a generation point (P_u) is the proportion of the total population warned for a given tsunami generation point:

$$
P_u = \left[\frac{\sum_{v=1}^{V} p_{u,v}(y)}{\sum_{v=1}^{V} P_v} \right]
\tag{2}
$$

We obtain a measure of the average performance of the TWS for all tsunami generation points by taking the average over the generation points or by summing the products of the relative frequency of tsunami generation and the warning potential over all generation points. The warning potential for each generation point and the average and weighted average warning potentials are thus dimensionless numbers between 0 (least preferable) and 1 (most preferable).

4. DATA

In order to solve this problem we will need data on existing stations and buoys, possible generation sites, and communication times.

4.1 Communication and response times

When changes in sea pressure reach the Bottom Pressure Recorder (BPR) of a DART buoy, the buoy can communicate data to tsunami warning centres in less than 3 minutes (Meinig et al 2005). Real-time sea level monitoring stations currently expect to transmit data within 6 minutes.

As different populations centres may require different response times, we consider a range of values for the population response time (though we use the same value of response time for each set of calculations) – 0 minutes, 15 minutes, 30 minutes, and 1 hour. These times were selected based on the minimum time it might take to move to an elevation above 10 meters, and the maximum time that could be utilized given the likely speeds of travel of a tsunami in the Mediterranean.

4.2 Tsunami wave speed, height and range

We compute tsunami travel times assuming an average wave speed. In the deep ocean, tsunami waves travel at speeds between 500 to 1000 km/hr (ITIC 2009). The wave speed of a tsunami may be approximated by $\sqrt{9.8*depth}$. With a maximum depth in the Mediterranean of approximately 5150 metres, it follows that a tsunami wave may travel at approximately 225 metres per second, or approximately 800 km/hr (Nelson 2009). We examine a range of average speeds, from 200 km/hr to 800 km/hr, to accommodate variability in sea depth.

As previously mentioned, tsunami wave heights can vary widely. In order to estimate populations that may be affected by a tsunami, we considered only coastal populations below 100 metres and within 2 kilometres of the shoreline.

4.3 Population centres

One hundred and sixty-one population centres on the coast of the Mediterranean Sea were selected as potentially being affected by tsunami inundation. Without inundation maps and detailed geographical population data, we could not determine the exact figures for the population that may be affected by a tsunami. As a consequence, we used the population of the entire centre as a proxy for the population affected. Further, we decided to admit the possibility that any population centre could be affected by a tsunami generated at any of the points considered. This is unlikely as not all populations centres would be directly affected by tsunamis generated by some of the generation points considered (as, for example, a tsunami may only reach a centre following diffraction). We ignored this last point in calculating the travel times of tsunamis to population centres – the resulting times are then more than worse case scenarios of tsunami arrival.

The population centre data collected included the latitude and longitude, and population size. This data was based on the Gridded Population of the World from The Trustees of Columbia University in the City of New York. An initial filter was applied to this data to remove locations that were not a part of the countries surrounding the Mediterranean Sea. A second filter was manually applied to remove locations that were unlikely to be affected by a tsunami. The populations centres used can be found in Table A1 of the Appendix.

4.4 Locations of sea level stations and DART buoys

The location of sea level stations and DART buoys for the existing TWS can be found in the Global Sea Level Observing System (2009) and NOAA National Data Buoy Center (2009). The current full configuration of the TWS includes 2 tsunameter buoys and approximately 24 coastal sea-level stations (Table A2 and Figure 2). A further 4 candidate DART buoy locations were included later in the analysis to see if performance in the warning potential could be improved. These candidate locations were selected based on DART buoy bathymetric requirements (Spillane et al 2008) as well as whether they provided coverage of the region (with bathymetric data from the National Geophysical Data Center (2009a)). As far as possible, we selected potential DART buoy sites so as to avoid major shipping lanes and areas associated with piracy (National Geospatial Intelligence Agency 2009). Location information for the DART buoys sites and the sea-level stations are listed in Tables A2 of the Appendix and represented in Figure 2. A further 6 locations for real-time sea-level monitoring stations were also examined as part of an extended (and improved) TWS.
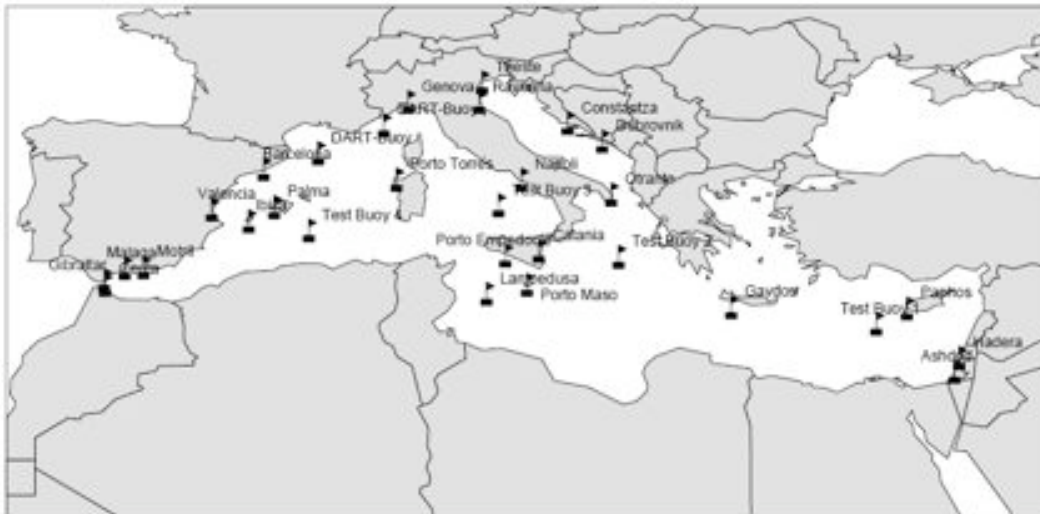
Figure 2 – Existing Sea level stations and existing and possible DART buoys sites

4.5 Potential tsunamigenic event locations

We based selection of tsunami generation points in the Mediterranean region on the historical record of magnitude and frequency of earthquakes and coastal volcanic activity available from the National Geophysical Data Center (2009) (Figure 1). The location of the tsunami generation points used in this study is a representative sample of these historical points. They are listed in Table A3 of the Appendix. With regard to the relative frequencies of tsunami events in the historical record, the Adriatic and Aegean Seas were approximately twenty-times more likely to generate a tsunami than the seas near Spain, France, Croatia, Egypt, Algeria, Israel, the Lebanon and Cyprus, while the seas surrounding southern Italy were approximately twice as likely to generate a tsunami.

5. SOLUTION APPROACH

We undertook the calculations of the times in Equation (1) and the warning potentials and average warning potentials (in Equations (2) and (3) respectively) using Excel spreadsheets. Workbooks were constructed for each of the tsunami wave speeds examined. Within each workbook, we constructed spreadsheets for undertaking the time calculations – generation point to detection site and generation site to population centre – with different response times. Travel times were determined using the Method of Great Circles (included as a cell formula). We then determined the time differences, and an "IF" statement was used to determine the $p_{u,v}$. The warning potentials for each generation point were then simply column sums divided by the sum of all populations, with the average warning potential, the average of these quotients. We then calculated the weighted average warning potentials also using the column sums. By undertaking the calculations in this fashion we were able to easily identify critical buoys and sea-level stations as well as identify regions requiring greater detector coverage.

6. RESULTS

6.1 The current configuration of sea-level stations and DART buoys

The table below shows the warning potentials for the TWS for each of the tsunami generation points when the estimated speed of the tsunami is 800 km/hr with the current detector configuration.

Table 1. Warning Potentials for a wave speed of 800 km/hr
(reported to four significant figures)

Generation Point		Nearest detector	Response Time			
Location	ID		0	15 min	30 min	1 hr
Tyrrhenian Sea	1	23	0.9124	0.7025	0.5842	0.3984
Adriatic Sea	2	20	0.9917	0.8827	0.6439	0.3878
Algeria	3	5	0.9678	0.9266	0.8023	0.6645
Croatia	4	24	0.9937	0.8181	0.6969	0.4330
Cyprus	5	10	0.9964	0.9740	0.8291	0.6909
Egypt	6	25	0.9022	0.8327	0.7641	0.6461
France	7	29	0.9968	0.9968	0.8058	0.4536
Greece	8	14	0.8598	0.8200	0.7245	0.3169
Israel	9	10	0.9439	0.8623	0.8349	0.8179
Italy	10	19	0.9242	0.6745	0.6088	0.4262
Aegean Sea	11	20	0.8211	0.7382	0.5284	0.2378
Spain	12	3	0.9899	0.9467	0.9403	0.8086
Lebanon	13	13	0.9106	0.8607	0.8349	0.7693
Total average warning potential	-	-	0.9440	0.8539	0.7458	0.5444
Total weighted average warning potential	-	-	0.9139	0.8311	0.6872	0.4139

The following discussion should be considered recalling the qualification on the more than worst-case performance described previously (Section 4.3). From Table 1, we can see that the obvious result that increasing the population response time decreases the warning potential, in many cases substantially. For example, each 15 minutes of response time means that, for an estimated wave speed of 800 km/hr, the tsunami has travelled an additional 200 km. For near-shore tsunami events (and the historical record of tsunami generation points in the Mediterranean Sea are indeed near-shore), this has a significant impact on the proportion of the population that will be able to utilise the full response time. From Table 1 it can be seen that this is particularly true for tsunamis generated in and near the Adriatic Sea, while the warning potential is more robust for tsunamis generated near Algeria, Israel, Spain and Lebanon. This observation concerning the Adriatic Sea is of particular interest given the density of its coastal population and the fact that its bathymetry precludes locating DART buoys in much of its length. We are of the view that this suggests that sea-level monitoring stations on the coast of the Adriatic Sea play a crucial role in tsunami warning for the (coastal) population centres of the region. This result is reinforced when considering the differences between the average warning potentials and the weighted average warning potentials. The poorer performance on the weighted average potentials is a consequence of the poorer warning potentials of the Adriatic Sea, Greece, and Aegean Sea tsunami generation points. This also suggests that further sea level monitoring stations may be required on these coasts.

By examining the "Nearest detector" column in Table 1, it is clear that only one DART buoy (off the coast of France) is the nearest detector to a tsunami generation point. It may also be noted that sea-level station 10, at Paphos, plays a vital role in early warning as seen in its proximity to tsunami generation points in Cyprus and Israel. These results highlight the significant role played by coastal sea-level monitoring stations in the effectiveness of a TWS, as also found by Groen, Botten and Blazek (2010) in their study of the Indian Ocean tsunami warning detector system.

It should be obvious that a reduction in wave speed will result in an increase in warning potential. We will consider a response time of 30 minutes, and examine reductions in tsunami wave speed (though calculations have been done for all the response times described previously).

From Table 2, we can see that as speed increases, warning potentials decrease. Increasing the tsunami wave speeds for the Adriatic Sea and the Aegean Sea generation points (Points 2 and 4, and Point 11 respectively) yield more significant losses in warning potential (an average of 32.35% and 36.7% respectively) than for the other generation points (an average of 16.4%). We are again of the view that this result is a function of the relatively long and narrow shape of the Adriatic Sea and the relative lack of sea-level monitoring stations on the respective coasts.

For wave speeds of 200km/hr, 400km/hr and 600km/hr, best system performance in warning potential occurs for the tsunami generated near France, while best system performance for a wave speed of 800km/hr occurs for tsunamis generated by earth movements off the coast of Spain. This can be explained by the location of a DART buoy near the French tsunami generation point and the Spanish generation point being at an extreme of the Mediterranean.

Table 2. Warning Potentials for a response time of 30 minutes
(reported to four significant figures)

Generation Point		Wave Speed (km/hr)			
Location	ID	200	400	600	800
Tyrrhenian Sea	1	0.8367	0.7775	0.6565	0.5842
Adriatic Sea	2	0.9899	0.8890	0.7361	0.6439
Algeria	3	0.9504	0.9266	0.8208	0.8023
Croatia	4	0.9920	0.8347	0.7193	0.6969
Cyprus	5	0.9913	0.9740	0.9111	0.8291
Egypt	6	0.9588	0.9022	0.8673	0.7641
France	7	0.9996	0.9968	0.9653	0.8058
Greece	8	0.8557	0.8254	0.8124	0.7245
Israel	9	0.9223	0.8924	0.8623	0.8349
Italy	10	0.8501	0.7601	0.6665	0.6088
Aegean Sea	11	0.8348	0.7414	0.6577	0.5284
Spain	12	0.9548	0.9515	0.9467	0.9403
Lebanon	13	0.9030	0.8648	0.8349	0.8349
Total average warning potential	-	0.9261	0.8720	0.8044	0.7458
Total weighted average warning potential	-	0.9461	0.8417	0.7653	0.6872

6.2 A possible expansion of the current configuration of sea-level stations and DART buoys

The current detector configuration was augmented by 4 DART buoys (Figure 2) using the criteria described in Section 4.4. It was found that one of the four additional buoys replaced an existing TWS detector – proposed DART buoy location (25) replaced a sea-level station (10) – as the nearest detector for the Egyptian tsunami generation point. For an estimated wave speed of 800km/hr, there was an 8.89% increase in warning potential for a 30-minute response time for that generation point. This increase amounts to approximately 5.25 million additional people across the coastal Mediterranean receiving a timely warning. Slightly smaller increases were observed for a one-hour response time (4.09% approx. or 2.41 million people approx.) and a 15-minute response time (7.76% approx. or 4.58 million people approx.). For slower tsunami wave speeds, the increase in performance of the TWS improved up to approximately 6% (for a tsunami wave speed of 200km/hr). Thus it can be seen that the addition of appropriately sighted DART buoys can have a significant impact on the warning potential of the Mediterranean TWS.

The relatively poor warning potentials for tsunamis generated in and near the Adriatic Sea suggest that further detectors on the coast of the Adriatic might improve average and weighted average warning potentials. It was also apparent that a real-time sea-level monitoring station(s) sited on the Turkish coast might also improve warning potentials. For this reason, we added six sites for coastal sea-level stations – two on the west coast of Turkey, one on the east coast of Greece, one on

the southern tip of Greece, and one on the west coast of Greece, with one on the coast of Albania. The following table shows the impact of these additions to the TWS on the warning potentials.

Table 3 includes the warning potentials as well as the change in warning potential from the current configuration of tsunami detectors (in brackets). From Table 3 we can see that while the improvement in total average warning potential is of the order of a few percent, significant gains in weighted average warning potentials and generation point-specific warning potentials are achieved. This confirms the previous suggestion that the deployment of real-time sea-level monitoring stations on the coasts of Greece and Turkey will improve the times available for populations responding to an impending tsunami.

Table 3. Updated Warning Potentials for a wave speed of 800 km/hr
for additional stations
(Warning potentials reported to four significant figures)

Generation Point		Nearest detector	Response Time			
Location	ID		0	15 min	30 min	1 hr
Adriatic Sea	2	35 (20)	0.9950 (<1%)	0.8849 (<1%)	0.7132 (10.8%)	0.3962 (2.2%)
Greece	8	34 (14)	0.9439 (9.8%)	0.8384 (2.2%)	0.8135 (12.3%)	0.5103 (60.0%)
Aegean Sea	11	33 (20)	0.9910 (20.7%)	0.8900 (20.6%)	0.8211 (55.4%)	0.5583 (134.8%)
Total average warning potential	-	-	0.9625 (1.9%)	0.8671 (1.5%)	0.7782 (4.3%)	0.5846 (4.0%)
Total weighted average warning potential	-	-	0.9673 (5.8%)	0.8694 (4.6%)	0.7807 (13.6%)	0.5300 (28.1%)

7. CONCLUSIONS

In this study we examined the performance of the current available infrastructure of a Mediterranean TWS. This study utilized the historic record of tsunamis of the region, and the locations of existing sea level monitoring stations and DART buoys to conclude that, for short response times (15 minutes and 30 minutes) and a wave speed of 800 km/hr, the existing infrastructure will enable between 57% and 94% of the coastal populations of the Mediterranean to respond. For slower wave speeds, 600 km/hr for example, the performance improves, with the lower limit increasing to 65% for a 30-minute response time.

Performance at the regional level under the existing detection infrastructure is variable, with notably lower warning potentials associated with tsunamis generated in and near the Adriatic Sea. This is primarily a consequence of the geography and bathymetry of the sea, which prevents the effective deployment of DART buoys. This is exacerbated by the lack of real-time sea-level monitoring stations in Greece. In the coastal Adriatic then, more reliance must be placed on sea level monitoring, direct observation and seismic alerts. Poor warning potential is also noted for tsunamis

generated near the west coast of Italy. This is primarily a consequence of the fact that the tsunami generation points are close to the coast in this area and hence coastal populations in this region must rely more heavily on direct observation and seismic alerts to inform their response. If we consider the warning potentials for tsunamis generated in areas other than these, the lower limit of the warning potential increases to 72% of the coastal population (for a wave speed of 800 km/hr and response time of 30 minutes).

The performance of the Mediterranean TWS can be improved by the addition of a DART buoy at or near 34.07726N 30.96548E. Calculations suggest that the improvement in the number of people warned in the Mediterranean region could increase by as much as approximately 9% over the current TWS detector configuration. Further improvement can be achieved through the addition of three coastal sea-level monitoring stations. These results suggest that the existing infrastructure can provide an acceptable level of 15 or 30 minute warning but that improvement is possible. All results presuppose the coordination of real-time information from the countries bounding the rim of the Mediterranean Sea, and assume the historical record of tsunami generation is repeated into the future.

Acknowledgments

REFERENCES

Amir L. and A. Cisternas, 2010, APPRAISAL OF THE 1790 ALBORAN TSUNAMI SOURCE IN THE WEST MEDITERRANEAN SEA AS INFERRED FROM NUMERICAL MODELLING: INSIGHTS FOR THE TSUNAMI HAZARD IN ALGERIA. Fourth International Tsunami Symposium of Tsunami Society International, 9th U.S. National and 10th Canadian Conference on Earthquake Engineering, July 25-29, 2010, Toronto, Ontario, Canada • Paper No. 1838.

Audet, C., G. Courtue, J. Dennis, M. Abramson, F. Gonzalez, V. Titov and M. Spillane (2008), Optimal Placement of Tsunami Buoys Using Mesh Adaptive Direct Searche, viewed 19 September 2009, <http://www.gerad.ca/Charles.Audet/Slides/Tsunami_JOPT.pdf >.

Braddock, R.D. and O. Carmody (2001), Optimal Location of deep-sea tsunami detectors, International Transactions in Operations Research, 8 249-258.

ESRI Australia, ArcGIS Version 9.3, <http://www.esriaustralia.com>.

Groen, L., L. C. Botten and K. Blazek (2010), Optimising the location of tsunami detection buoys and sea level detection sites in the Indian Ocean, International Journal of Operational Research, 4 (2) 174-188.

ICG/NEAMTWS-III (2007). Implementation Plan for the Tsunami Early Warning and Mitigation System in the North-Eastern Atlantic, the Mediterranean and Connected Seas (NEAMTWS), 2007–2011, UNESCO, viewed September 9 2009 <http://ioc3.unesco.org/ioc-24/documents/TS_73_NEAMTWSDraftImPlan.pdf>. IOC Technical Series No. 73 Action Plans. I.O.C.T. Series. Bonn, Germany.

International Tsunami Information Center (2005), "How we save lives", viewed 12 September 2009, <http://ioc3.unesco.org/itic/categories.php?category_no=140>.

International Tsunami Information Center, NOAA-UNESCO/IOC (2009), "Tsunami, Great Waves", viewed 12 September 2009, <http://ioc3.unesco.org/itic/files.php?action=viewfile&fid=808&fcat_id=137>.

MedGLOSS 2009, Last readings from MedGLOSS stations network , MedGLOSS, viewed 9 September 2009 <http://medgloss.ocean.org.il/map.asp>.

Meinig, C., S.E. Stalin, A.I. Nakamura, H.B. Milburn (2005), Real-Time Deep-Ocean Tsunami Measuring, Monitoring, and Reporting System: The NOAA DART II Description and Disclosure, viewed 12 September, available at <http://nctr.pmel.noaa.gov/Dart/dart_ref.html>.

National Data Buoy Centre, Deep-ocean Assessment and Reporting of Tsunamis (DART®) Description, viewed 14 December 2009, <http://www.ndbc.noaa.gov/dart/dart.shtml>.

National Geophysical Data Center NOAA 2009, Tsunami Events Full Search, sort by Date, Country, NOAA, viewed 12 September 2009 <http://www.ngdc.noaa.gov/nndc/struts/results?bt_0=&st_0=&type_8=EXACT&query_8=50&op_14=eq&v_14=&st_1=&bt_2=&st_2=&bt_1=&bt_10=&st_10=&ge_9=&le_9=&bt_3=&st_3=&type_19=EXACT&query_19=None+Selected&op_17=eq&v_17=&bt_20=&st_20=&bt_13=&st_13=&bt_16=&st_16=&bt_6=&st_6=&bt_11=&st_11=&d=7&t=101650&s=70>.

National Geophysical Data Center NOAA 2009a, NGDC/MGG - 2 minute bathymetry/topography image selector, NOAA, viewed 23 November 2009 <http://www.ngdc.noaa.gov/mgg/image/2minsurface/>.

National Geospatial-Intelligence Agency 2009, Anti-Shipping Activity Messages, National Geospatial-Intelligence Agency, viewed 9 September 2009 <http://www.nga.mil/portal/site/maritime/?epi_menuItemID=7c1695cead727e6e36890127d32020a0&epi_menuID=e106a3b5e50edce1fec24fd73927a759&epi_baseMenuID=e106a3b5e50edce1fec24fd73927a759>.

Nelson, S. 2009, Tsunami , Tulane University, viewed 9 September 2009 <http://www.tulane.edu/~sanelson/geol204/tsunami.htm>.

Pararas-Carayannis, G., 1973. The waves that destroyed the Minoan empire, Sea Frontiers 1972, 94-106.

Pararas-Carayannis, G.: 1974. The waves that destroyed the Minoan empire, Revised for Grolier Encyclopedia, Science Supplement, pp. 314-321.

Pararas-Carayannis, G., 1992. The Tsunami Generated from the Eruption of the Volcano of Santorin in the Bronze Age Natural Hazards 5:115-123,1992. 1992 Kluwer Academic Publishers (Netherlands.)

Pararas-Carayannis, G. 2006. The Potential for Tsunami Generation in the Eastern Mediterranean Basin and in the Aegean and Ionian Seas in Greece
http://www.drgeorgepc.com/TsunamiPotentialGreece.html

Pararas-Carayannis G. & Mader, C.L. 2010. THE EARTHQUAKE AND TSUNAMI OF 365 A.D. IN THE EASTERN MEDITERRANEAN SEA, Fourth International Tsunami Symposium of Tsunami Society International, 9th U.S. National and 10th Canadian Conference on Earthquake Engineering, July 25-29, 2010, Toronto, Ontario, Canada • Paper No 1846

Pararas-Carayannis, G., Theilen-Willige, B. , & Helmut Wenzel, 2010. LOCAL SITE CONDITIONS INFLUENCING EARTHQUAKE INTENSITIES AND SECONDARY EFFECTS IN THE SEA OF MARMARA REGION - Application of Standardized Remote Sensing and GIS-Methods in Detecting Potentially Vulnerable Areas to Earthquakes, Tsunamis and Other Hazards, Fourth International Tsunami Symposium of Tsunami Society International, 9th U.S. National and 10th Canadian Conference on Earthquake Engineering, July 25-29, 2010, Toronto, Ontario, Canada • Paper No 1845

ScienceMaster 2009, ScienceMaster - Physical Science - Glossary of Earthquake Terms, ScienceMaster, viewed 12 September 2009
<http://www.sciencemaster.com/physical/item/earthquake_glossary.php#tsunami>.

The Belfast Telegraph 2009, Millions at risk from Mediterranean tsunami , The Independent, viewed 12 September 2009 <http://www.independent.co.uk/news/world/europe/millionsat-risk-from-mediterranean-tsunami-1712767.html>.

The Trustees of Columbia University in the City of New York 2009, Gridded Population of the World - GPW v3, CIESIN - Columbia University, viewed 9 September 2009 <http://sedac.ciesin.columbia.edu/gpw/global.jsp>.

Tsunami Institute 2009, Mediterranean, Tsunami Institute, viewed 12 September 2009 <http://www.tsunami-alarm-system.com/uploads/pics/tsunami_mediterranean.jpg>.

University of Cambridge 2009, Tsunami risk in the Mediterranean, University of Cambridge, viewed 12 September 2009 <http://www.researchhorizons.cam.ac.uk/researchnews/tsunami-risk-in-the-mediterranean.aspx>.

Westall, S. 2008, "Mediterranean tsunami warning system set for 2011." Viewed 12 September 2009, <http://www.reuters.com/article/idUSL1685238820080416>.

APPENDIX

Distance calculation

The calculation of the following distances is based on the Method of Great Circles. The Method of Great Circles calculates spherical distances from pairs of latitude and longitude values using the shortest. A great circle is a circle defined by the intersection of the surface of the Earth and any plane that passes through the centre of the Earth. The great circle (geodesic) distance between two points, P_1 and P_2, located at latitude x_1 and longitude x_2 of (x_{11}, x_{21}) and (x_{12}, x_{22}) on a sphere of radius a is

$$d = a \cos^{-1} \cos x_{11} \cos x_{12} \cos (x_{21} - x_{22}) + \sin x_{11} \sin x_{12}$$

Here a is the radius of the Earth (assuming it is spherical).

Input Data

Table A1 – Population Centres

Population Centre	Lat. (N)	Long. (E)	Pop^n	Population Centre	Lat. (N)	Long. (E)	Pop^n
Israel				*Turkey*			
Khefa	32.59875	34.9531	416500	Hatay Province	36.51361	36.205	1386224
Ha Merkaz	32.09817	34.89002	1200800	Icel	36.53417	33.93917	989635
Telaviv	32.07477	34.81803	1136900	Mugla	36.90381	28.6319	185175
Hadaron	31.6125	34.65417	69100	Aydin	37.76917	27.53667	313041
Cyprus				Izmir	38.47627	27.18134	2682948
Ammochostos District	35.03333	33.92738	32090	Canakkale	40.07556	26.72333	171578
Larnaka District	34.93776	33.56823	92857	*Syria*			
Lefkosia District	35.09171	33.27422	210808	Tartus	34.9	35.9	52589
Lemesos District	34.72279	33.00172	168360	Ladhaqiyah	34.66556	35.84778	365968
Pafos District	34.80357	32.42976	43121	*Serbia and Montenegro*			
Greece				Montenegro	41.92972	19.20806	13145
Dodekanisos	36.55781	27.60813	156609	*Lebanon*			
Samos	37.72778	26.79556	23100	Albiqa	33.92394	36.0735	136600
Lesvos	39.225	26.233	61300	Assamal	34.34	35.77	210000
Hios	38.37761	26.11381	33879	Jabal Lubnan	33.93771	35.60264	173100
Lasithi	35.13565	25.79076	40700	Annabatiyah	33.385	35.525	98900
Rodopi	41.08769	25.47846	64486	Bayrut	33.87194	35.50972	1100000
Kiklades	37.01963	25.21273	53300	Aljanub	33.46963	35.40037	261600
Iraklion	35.21731	25.14731	202212	*Egypt*			
Xanthi	41.14	24.89643	65618	Sina Ash Shamaliyah	31.20389	34.01694	125147
Rethimni	35.29429	24.68429	38887	Bur Said	31.26667	32.3	469533
Kavala	40.89808	24.45654	113002	Dumyat	31.35889	31.7325	236716
Hania	35.47765	23.94569	97073	Al Garbiyah	30.88397	31.03329	1029842

Population Centre	Lat. (N)	Long. (E)	Pop^n	Population Centre	Lat. (N)	Long. (E)	Pop^n
Attiki	37.99476	23.7429	3729385	Kafr Ash Shaykh	31.23377	30.86065	495804
Evvoia	38.53778	23.68694	143384	Matruh	31.19	27.83667	73547
Halkidiki	40.27203	23.49553	71900	*Slovenia*			
Magnisia	39.28375	23.05	168139	Divaca	45.68778	13.97167	3829
Thessaloniki	40.64427	22.99854	1020945	Komen	45.81361	13.74667	3515
Argolis	37.54721	22.9325	71700	Obalnokraska	45.57874	13.71046	90688
Fthiotis	38.71469	22.8825	44600	*France*			
Korinthia	37.94898	22.8143	98487	Saint Maxime	43.3167	6.65	15565
Lakonia	36.83533	22.726	42200	Saint Tropez	43.26667	6.633333	8154
Larisa	39.74857	22.62	13100	Languedoc-Roussillon	43.19167	2.852083	647714
Pieria	40.28214	22.56064	88109	Corsedusud	42.30972	9.091667	153726
Imathia	40.61	22.536	8500	*Croatia*			
Arkadia	37.43286	22.50571	39800	Sibenikknin	43.87787	16.08713	51460
Messinia	37.07737	21.87368	95350	Zadarknin	44.04324	15.33139	78756
Ilia	37.74483	21.44241	97400	Likasenj	44.80167	15.17269	15988
Arta	39.1575	20.93375	27900	Primorjegorskikotar	45.17685	14.51639	183900
Aitoliakaiakarnania	38.91333	20.89833	11400	Istra	45.14208	13.73438	104780
Zakinthos	37.77	20.84333	17700	Dubrovnik Neretva	42.83685	17.53324	62036
Levkas	38.83	20.7	6900	Split Dalmacija	43.48668	16.57762	279990
Preveza	39.17714	20.69714	30400	*Tunisia*			
Kefallinia	38.245	20.57	15600	Halqalwadi	36.85	10.32	61600
Thesportia	39.5	20.32429	18800	Bardo	36.82	10.13	65669
Kerkira	39.58397	19.90304	50400	Mahdia	35.36556	10.97299	95115
Tripoli	32.8925	13.18	1250000	Monastir	35.67154	10.83436	273089
Albania				Sfax	34.72167	10.76301	355148
Sarande	39.88	20	14548	Nabeul	36.65171	10.74212	315584
Kruje	41.52333	19.73	36653	Sousse	35.82561	10.57761	249692
Lushnje	40.95	19.71	38341	Tunis	36.83875	10.28875	809908
Kurbin	41.64	19.71	23508	Benarous	36.73056	10.25611	238613
Lezhe	41.79	19.65	16670	Manouba	36.80778	10.10111	21799
Fier	40.69889	19.64778	82700	Gabes	33.84083	10.0625	72630
Vlore	40.51	19.57	92089	Ariana	36.87311	10.04172	231565
Kavaje	41.2	19.56	28269	Bizerte	37.18597	9.879722	255882
Durres	41.25333	19.55667	132338	Jendouba	36.62889	8.737153	88200

Population Centre	Lat. (N)	Long. (E)	Pop^n	Population Centre	Lat. (N)	Long. (E)	Pop^n
Shkoder	42.07	19.51	86122	*Algeria*			
Malsiemadhe	42.2	19.43	4080	Tarf	36.88333	8.483333	21254
Libya				Annaba	36.86667	7.8	352523
Bardiyah	31.75	25.07	7500	Skikda	36.88333	6.888889	210649
Tubruq	32.08361	23.97639	92000	Jijel	36.65333	5.902222	196813
Darnah	32.765	22.63917	73000	Bejaia	36.60833	4.816667	177196
Sahhat	32.83	21.86	28100	Tiziouzou	36.70167	4.066667	140407
Albayda	32.76639	21.74167	74500	Boumerdes	36.73333	3.538889	106543
Almarj	32.5	20.83333	97000	Alger	36.74167	3.219167	218024
Alcquriyah	32.53	20.57	15500	Chlef	36.31667	1.308333	202504
Suluq	31.67111	20.25111	10400	Mostaganem	35.91667	0.1	125911
Azzwaytinah	30.95	20.12	12200	Oran	35.75	-0.53333	730530
Bangaz	32.12	20.07	500000	Aintemouchent	35.18333	-1.25	92557
Marsaalburayqah	30.41667	19.57861	8000	Tlemcen	35.05833	-1.575	46723
Surt	31.20611	16.59472	38500	*Spain*			
Misratah	32.37833	15.09056	135000	Girona	42.00179	2.862564	304896
Zeleiten	32.46667	14.56667	26000	Balears	39.55938	2.789583	647458
Zitan	32.48	14.56	100000	Baleares	39.56667	2.65	333801
Alhums	32.66	14.26	120000	Cataluna	41.5	2.216667	160262
Azzwiyah	32.76	12.72	116000	Barcelona	41.49908	2.138495	4223710
Sabratah	32.79194	12.48472	46500	Tarragona	41.00417	1.036111	371368
Italy				Castello	40.32333	0.31	55113
Calabria	39.0237	16.27778	1082147	Alacant	38.75763	0.105009	79542
Campania	40.8436	14.47082	4467955	Murcia	37.41	-1.59	27771
Palermo, Sicilia	38.11667	13.36668	657935	Almeria	36.97939	-2.4797	387701
Abruzzo	42.44322	14.02897	738754	Melilla	35.3	-2.95	66411
Marche	43.38017	13.39274	962202	Malaga	36.71368	-4.56579	1121504
Lazio	41.78436	12.82868	4378693	Ceuta	35.9	-5.29	71505
Puglia	40.76781	17.15583	3491037	*Morocco*			
Calgliari, Sardegna	39.24639	9.0575	400000	Oriental	35.17	-2.95	112450
Porto Torres, Sardegna	40.83333	8.4	22217	Tazaalhoceimat aounate	35.19958	-3.89972	80716
Bosnia and Herzegovina							
Serb Republic	42.71	18.34	28500				

Table A2 – Locations of Detectors

Location	ID	Latitude	Longitude	Location	ID	Latitude	Longitude
Existing Real-time Sea-level Stations							
Gibraltar	1	36.117	-5.35	Hadera	13	32.47053	34.86306
Malaga	2	36.7	-4.4	Gavdos	14	34.848	24.119
Motril	3	36.716	-3.516	Trieste	15	45.42268	12.4235
Valencia	4	39.45	-0.31	Ravenna	16	44.49645	12.27978
Ibiza	5	38.9	1.43	Genova	17	44.49645	8.92568
Barcelona	6	41.35	2.15	Porto Empedocle	18	37.29016	13.52432
Ceuta	7	35.9	-5.317	Napoli	19	40.83962	14.26913
Palma	8	39.55	2.63	Otranto	20	40.14617	18.49672
Porto Maso	9	35.909	14.519	Porto Torres	21	40.84071	8.40437
Paphos	10	34.78333	32.401	Lampedusa	22	35.48333	12.61667
Constantza	11	43.507	16.442	Catania	23	37.49699	15.09344
Ashdod	12	31.811	34.635	Dubrovnik	24	42.65	18.06667
DART Buoys							
Test Buoy 1	25	34.07726	30.96548	Test Buoy 4	28	38.46404	4.281104
Test Buoy 2	26	37.2073	18.83862	DART-Buoy	29	43.4	7.8
Test Buoy 3	27	39.63586	13.19198	DART-Buoy	30	42.103	4.703
Proposed Real-time Sea-level Stations							
Test SlS 1 (near Mugla)	31	36.56256	28.01476	Test SlS 4 (Laconia)	34	36.80529	22.62476
Test SlS 2 (east of Lesvos)	32	39.07627	26.09159	Test SlS 5 (west of Kerkira)	35	39.59183	19.80302
Test SlS 3 (east of Larissa)	33	39.57667	22.93225	Test SlS 6 (vicinity of Lezhe)	36	41.82766	19.5448

Table A3 – Tsunami Generation Points

Location	ID	Latitude	Longitude	Location	ID	Latitude	Longitude
Tyrrhenian Sea	1	38.6929	15.259	Greece	8	37.222	23.756
Adriatic Sea	2	39.934	19.371	Israel	9	33.805	32.9125
Algeria	3	36.754	1.554	Italy	10	40.67053	13.78057
Croatia	4	42.445	17.326	Aegean Sea	11	39.4	22.3
Cyprus	5	34.8	32	Spain	12	36.44433	-2.589
Egypt	6	31.901	30.582	Lebanon	13	33.624	34.992
France	7	43.04	6.937				

THE EARTHQUAKE AND TSUNAMI OF 27 FEBRUARY 2010 IN CHILE –
Evaluation of Source Mechanism and of Near and Far-field Tsunami Effects

George Pararas-Carayannis
Tsunami Society International, Honolulu, Hawaii 96815, USA
tsunamisociety@hawaiiantel.net

ABSTRACT

The great earthquake of February 27, 2010 occurred as thrust-faulting along a highly stressed coastal segment of Chile's central seismic zone - extending from about 33ºS to 37ºS latitude - where active, oblique subduction of the Nazca tectonic plate below South America occurs at the high rate of up to 80 mm per year. It was the 5th most powerful earthquake in recorded history and the largest in the region since the extremely destructive May 22, 1960 magnitude $M_w9.5$ earthquake near Valdivia. The central segment south of Valparaiso from about 34º South to 36º South had been identified as a moderate seismic gap where no major or great, shallow earthquakes had occurred in the last 120 years, with the exception of a deeper focus, inland event in 1939. The tsunami that was generated by the 2010 earthquake was highest at Robinson Crusoe Island in the Juan Fernández archipelago as well as in Talchuano, Dichato, Pelluhue and elsewhere on the Chilean mainland, causing numerous deaths and destruction. Given the 2010 earthquake's great moment magnitude of 8.8, shallow focal depth and coastal location, it would have been expected that the resulting tsunami would have had much greater Pacific-wide, far field effects similar to those of 1960, which originated from the same active seismotectonic zone. However, comparison of the characteristics of the two events indicates substantial differences in source mechanisms, energy release, ruptures, spatial clustering and distributions of aftershocks, as well as in geometry of subduction and extent of crustal displacements on land and in the ocean. Also, the San Bautista and the Juan Fernández Islands - ridges rising from the ocean floor – as well as the O'Higgins seamount/guyot may have trapped some of the tsunami energy, thus accounting for the smaller, far field tsunami effects observed elsewhere in the Pacific. Apparently, complex, localized structural anomalies and interactions of the Nazca tectonic plate with that of South America, can account for differences in the spatial distribution and clustering of shallow event hypocenters, as well as for seismic gaps where large tsunamigenic earthquakes could strike Chile's Central Seismic zone in the future.

Key Words: Tsunami, Chile, seismotectonics, Peru-Chile subduction, energy trapping.

1. INTRODUCTION

Continuous crustal deformation associated with ridge collision and oblique convergence of the Nazca tectonic plate with the continental block of South America in the central Chile region had caused substantial deformation and strain accumulation which culminated in the great earthquake of February 27, 2010 (Fig. 1). The quake caused several hundred deaths and injuries and great destruction to property. Shortly thereafter, a destructive tsunami impacted coastal towns and villages in south-central Chile and the Juan Fernández Islands. There was substantial tsunami damage at Talcahuano, Constitución, Concepcion, Dichato and Pichilemu. A Pacific-wide tsunami warning was issued for the countries bordering the Pacific Basin. Although the tsunami's source region was immediately to the north of the destructive 1960 event and there were many similarities, the far-field impact was not as severe as anticipated.
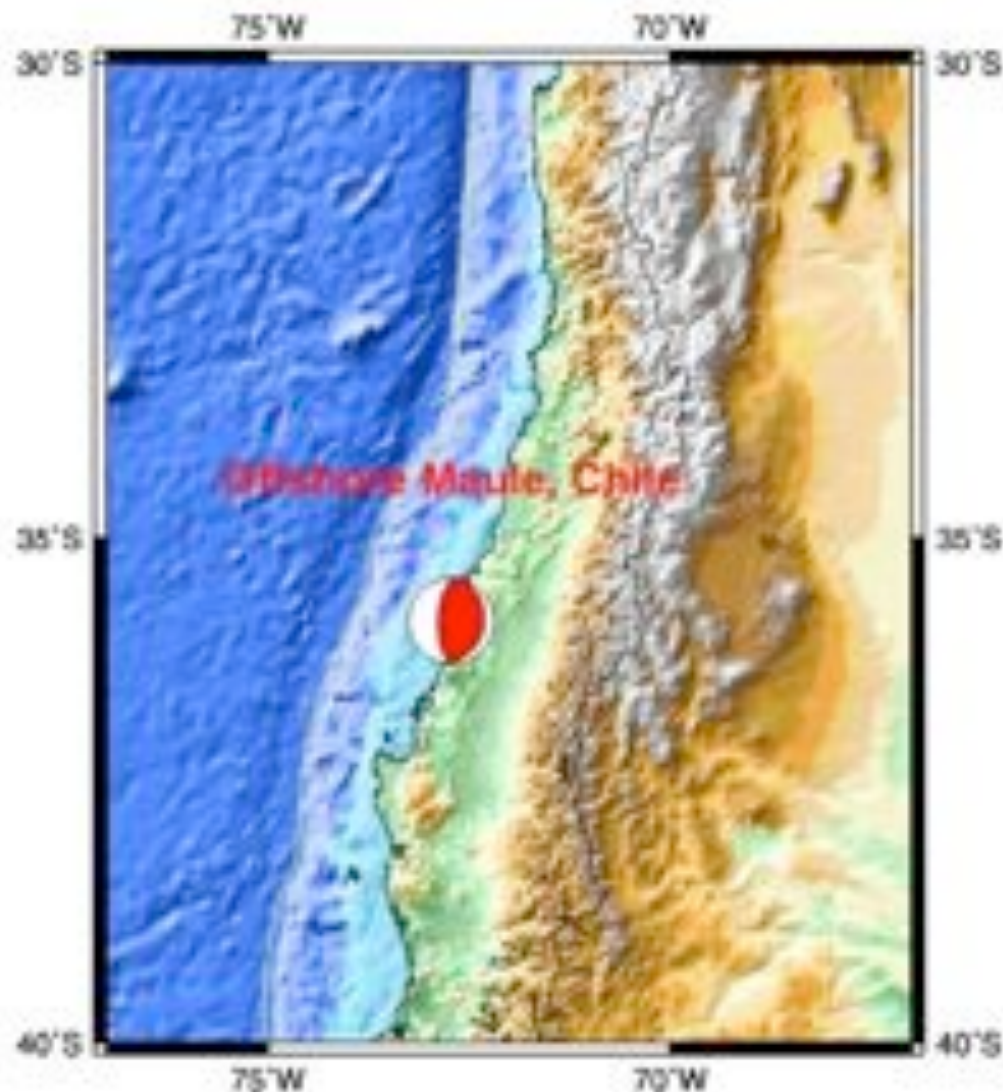

Fig. 1. Epicenter and focal mechanism of the Earthquake of 27 February 2010.

The present study examines the source characteristics of the February 27, 2010 earthquake and the possible reasons for the tsunami's less severe, far-field effects. Specifically examined are the seismotectonics of Chile's central seismic zone, the focal mechanism of the earthquake, the extent of ground and ocean floor displacements, the aftershock hypocenter space/time distribution, the geometry of subduction, the quake's tsunamigenic efficiency, the tsunami energy flux directivity, the absorption, trapping, reflection and ducting of wave energy by the Juan Fernández submarine ridge, the O'Higgins seamount and other submarine features and finally the potential for future destructive tsunamis from Chile's central seismic zone. Also, a comparison is made of similarities and differences of the source characteristics of the of February 27, 2010 tsunami with those of the destructive, Pacific-wide tsunami of May 22, 1960.

2. THE EARTHQUAKE

The Peru-Chile Trench is a manifestation of very active subduction along the South American continent. Most of the destructive tsunamis along the South American coast have been generated from major or great shallow earthquakes in close proximity to the Peru-Chile Trench. The great earthquake (magnitude Mw=8.8) that struck the Bio-Bio Province (population: 1.7 million) of Central Chile on early Saturday morning of February 27, 2010, 6:34:17 AM UTC (3:34 a.m. local time) was a subduction zone event which occurred as thrust-faulting near the interface of convergence, where the Nazca tectonic plate subducts landward below the South American continent plate at a rate of up to 80 mm per year. Its epicenter was at 35.909 S, 72.733 W offshore from Maule; 99 km (61 miles) of Talca; 117 km (73 miles) NNE of Concepción; and 317 km (197 miles) SW of Santiago. Its focal depth was given as 35 km. (21.7 miles) (USGS). Many cities in Maule region were seriously affected.

Aftershocks - A large vigorous aftershock sequence followed the main earthquake. There was unusual clustering of aftershocks in the first few minutes, which supports an anomalous rupture. An aftershock of $M_w6.2$ was recorded 20 minutes after the initial quake. A 6.9-magnitude offshore earthquake struck approximately 300 kilometers southwest less than 90 minutes after the initial shock; however, this may have been a separate event that may not have been related to the main shock. Two more aftershocks with magnitudes 5.4 and 5.6 followed within an hour. In the 2 1/2 hours following the 90-second main shock, 11 more were recorded. By March 1, 2010, a total of 121 aftershocks with magnitude 5.0 or greater were recorded (USGS NEIC). Eight of these had magnitudes of 6.0 or greater. By March 29, 2010, a total 458 aftershocks had been recorded. The significance of the aftershock distribution and of their spatial clustering as it relates to tsunami generation, is discussed in a subsequent section.

Rupture - The earthquake had a complicated rupture process. The total rupture was about 550 km long, more than 100 km wide and extended to about 50 km in depth. It paralleled the coast of Chile and affected an area of about 82,500 square kms.

Fig. 2. Epicenter of the February 27, 2010 earthquake and distribution of aftershocks up to 18:00 UTC Mar 3. (Modified image from UNAVCO's Jules Verne Voyager).

Ground Motions and Earthquake Intensity - Ground shaking levels lasted for 90 seconds. Maximum acceleration of 0.65g was recorded at Concepción (USGS). The quake was strongly felt in six regions of Chile, from Valparaíso in the north to Araucanía in the south. The cities experiencing the strongest shaking were Concepción (IX) and Arauco and Coronel (VIII). In Santiago the intensity was VII. Intensities of VIII were experienced at Chiguayante, Coronel, Lebu, Nacimiento, Penco, Rancagua, Santiago, San Vicente, Talca, Temuco and Tome; Intensities of VII were felt from La Ligua to Villarrica and VI as far as Ovalle and Valdivia to the south. The quake was strongly felt in Argentina - including Buenos Aires, Córdoba, Mendoza and La Rioja - and in Ica in southern Peru about 2,400 km away. It was also felt in parts of Bolivia, southern Brazil, Paraguay, Peru and Uruguay (USGS).

Crustal Movements - Based on GPS Geodetic measurements, a team from Ohio State University and other institutions documented that the continental block moved westward. Specifically, it was determined that the city of Concepción moved 3.04 meters (10 ft) west, Santiago 28 centimeters (10 in) to the west-southwest and even Buenos Aires - about 1,350 kilometers (840 mi) from Concepción - moved westward by 3.9 centimeters (1.5 in). Maximum uplift of more than 2 m was observed along the coast Arauco.
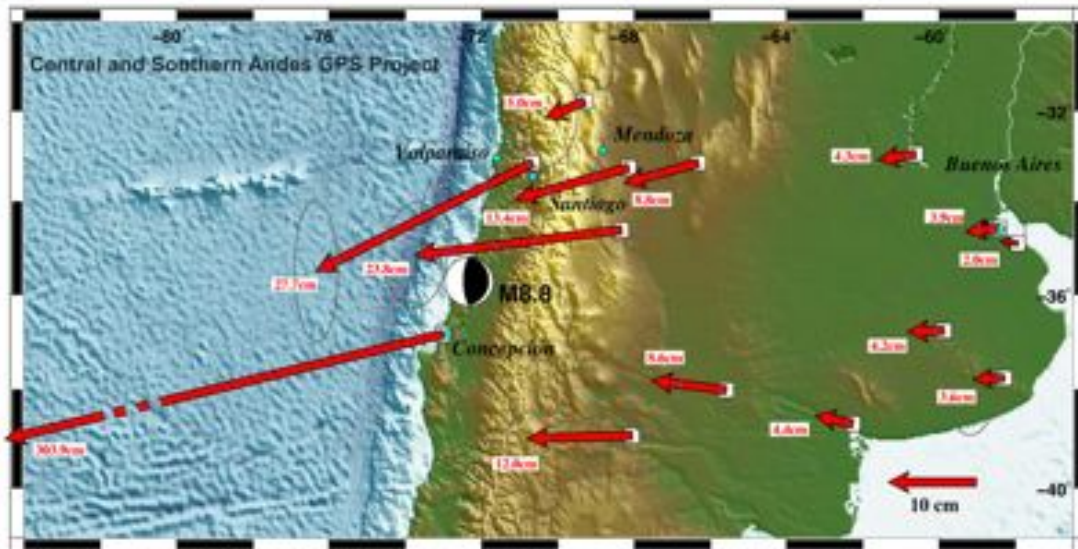
Fig. 3. Preliminary solution for the coseismic displacement field associated with the February 27, 2010 Maule earthquake in south-central Chile, based on GPS Geodetic measurements (as determined by James Foster and Ben Brooks of the University of Hawaii).

Due to the large extent of the epicentral region, the geologic conditions vary in the region from mountainous terrain and valleys to river and coastal terrains. Since the earthquake occurred towards the end of the southern hemisphere's summer season, the ground water conditions were favorably low. Thus, there were fewer landslides and ground related failures related to liquefaction, lateral spreading and bearing capacity. However, certain areas with soft soils were subjected to higher seismic energy focusing and ground motion amplification.

Closing of Seismic Gap - The region south of Valparaiso from about 34º to 36º South had been identified as a moderate seismic gap because it has not ruptured since1835 (Barrientos, 1987; Campos et al., 2002). The quake relieved stress by rupturing this seismic gap segment of the South American subduction zone, which separated the source regions of the great earthquakes of 1960 and 1906. However the area affected included portions of both the 1960 and 1906 events.

Fig. 4. Epicenter of the February 27, 2020 quake in relation to the 1960 and 1906 quakes. Seismic gap from about 34° South to 36° South (Modified web figure)
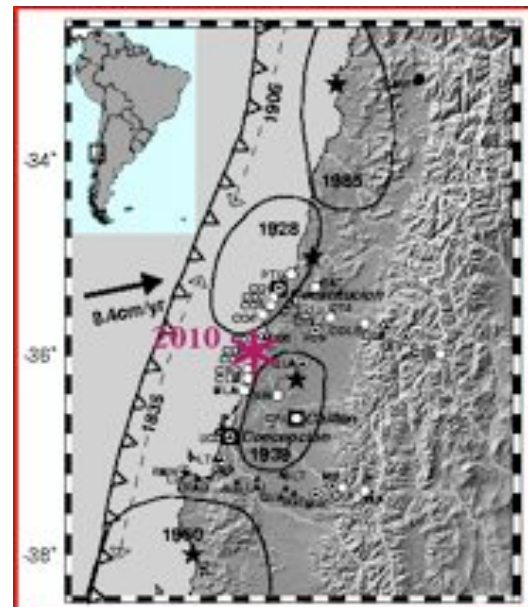
Planetary Impact – According to NASA, the 2010 earthquake resulted in a tiny shift in the Earth's axis estimated at three inches (8 cms), which affected the rate of its rotation, thus shortening the length of a day by 1.26 microseconds. It is believed that great earthquakes have a large enough moment to affect the earth's polar motion and that the impact is cumulative, not only on the Earth's axis of rotation and free nutation (due to non rigidity and spinning dynamics of the aspheric earth), but on the Chandler wobble (the Chandler Oscillation) of the earth's axis.

Additionally, great earthquakes such as that of 2010, are known to generate self-excited, long period, toroidal and spheroidal oscillations on the Earth's surface that tend to resonate over long periods of time, lasting many hours and days. The most important of the spheroidal oscillations have a fundamental mode estimated at 58 to 60 minutes. For example, the August 9, 1952 Kamchatka Earthquake had a fundamental frequency mode of 57 minutes (Benioff *et al.,* 1961). Similar frequency modes were determined for the May 1960 tsunami in Chile (Bogert, 1961; Ness *et al.,* 1961; Alsop *et al.,* 1961; Alsop, 1964b; Bolt, 1963; Connes *et al.,* 1962; Nowroozi and Alsop, 1968; and Dziewonski and Landisman, 1970), for the Kurile Islands earthquake of October 13, 1963 (Alsop, 1964a; Abe *et al.,* 1970; Dziewonski and Landisman, 1970), for the great earthquake of March Alaska, 1964 (Nowroozi, 1965; Smith, 1966; and Slichter, 1967), for the Rat Islands, February 4, 1965 (Nowroozi, 1966) and reported for the December 26, 2004 great Sumatra earthquake (Pararas-Carayannis, 2005).

Since spheroidal oscillations form standing waves with vertical excursion, these could contribute to tsunami-like sea level fluctuations along certain coastal areas. For example, 11 minutes after the earthquake in Chile there were oscillations of about 5 inches observed in Lake Pontchartrain, in Louisiana. However these were caused probably by the arrival of surface seismic waves rather than from Earth spheroidal oscillations. Slow crustal deformation and displacements associated with great earthquakes - such as the one in 1960 - can generate seismic waves with unusually long-periods (Kanamori & Cipar, 1974).

3. THE TSUNAMI

Based on the great magnitude of the February, 27, 2010 earthquake, its epicentral location and a confirmed initial tsunami height of 1.5m at a buoy near the source region (Talcahuano), a Pacific-wide tsunami warning was issued for Chile, Peru, Ecuador, Colombia, Antarctica, Panama, Costa Rica, Nicaragua, Pitcairn, Honduras, El Salvador, Guatemala, French Polynesia, Mexico, the Cook Islands, Kiribati, Kermadec Island, Niue, New Zealand, Tonga, American Samoa, Jarvis Island, Wallis-Futuna, Tokelau, Fiji, Australia, Palmyra Island, Johnston Island, Marshall Island, Midway Island, Wake Island, Tuvalu, Vanuatu, Howland-Baker, New Caledonia, Solomon Island, Nauru, Kosrae, Papua New Guinea, Pohnpei, Chuuk, Marcus Island, Indonesia, North Marianas, Guam, Yap, Belau, Philippines and Taiwan. Also, regional tsunami centers in the Pacific issued warnings. All tsunami warnings were canceled less than 18 hours later, except for those issued by Russia, Japan and the Philippines.

The tsunami damaged or destroyed many structures in Central Chile, including Constitución, Concepcion, Dichato and Pichilemu. There was a report of some damage to boats and a dock in San Diego, California and of flooding damage in northern Japan.

Tsunamigenic Area - A review of IRIS broadband data the earthquake aftershock distribution and of the moment tensor analysis of the February 27, 2010 earthquake indicate a general trend striking at 18^0 with a dip of $18^{0.}$ and a slip of almost 10 meters on the fault plane. The total rupture was about 550 km long, more than 100 km wide and extended to about 50 km in depth. Fig. 5 shows the approximate dimensions and orientation of the tsunamigenic area. It paralleled the coast of Chile and affected an area of about 82,500 square kms**.**
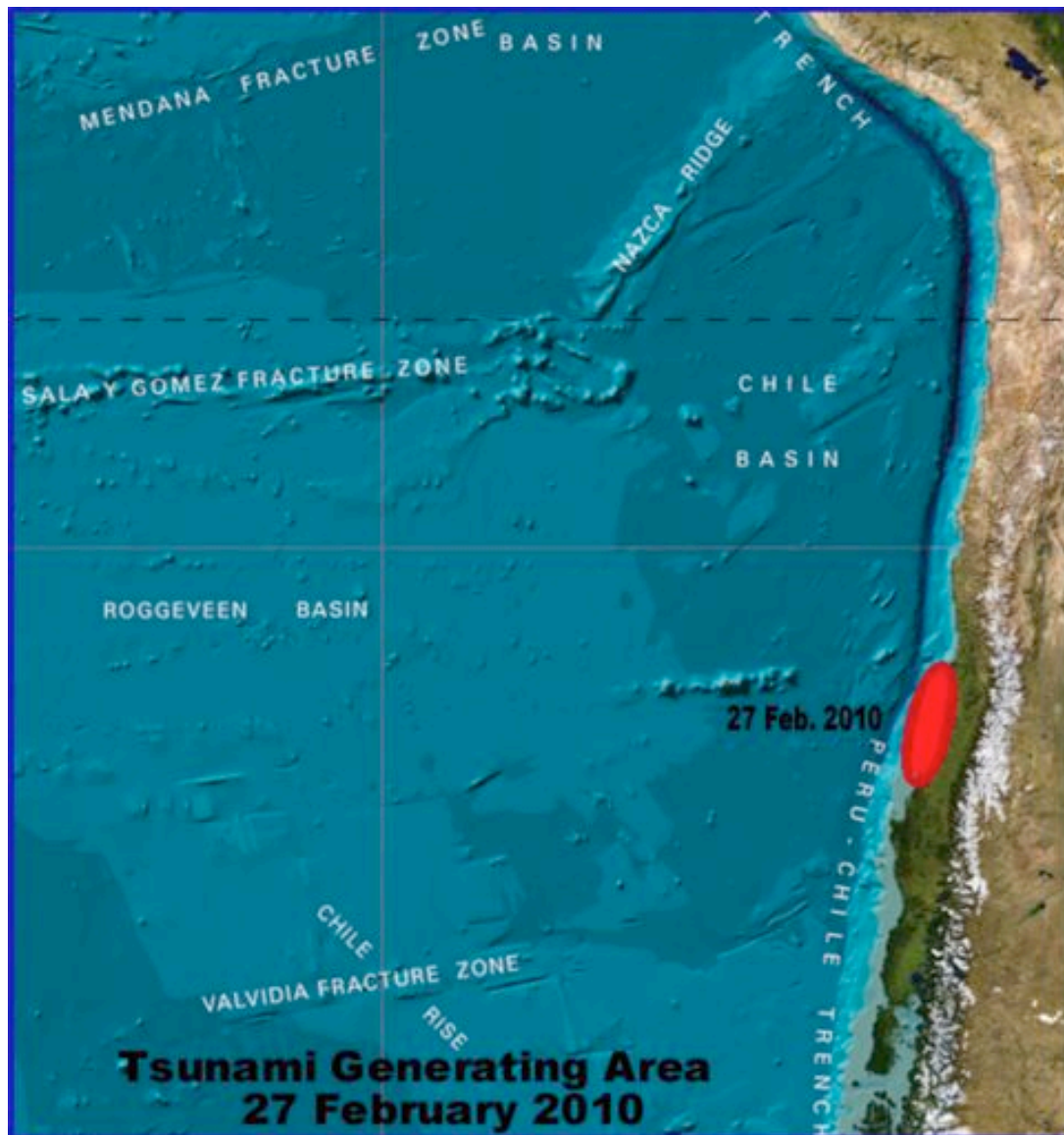

Fig. 5. Generating area of the February 27, 2010 tsunami based on earthquake aftershock distribution.

Ocean Floor Displacements and Initial Tsunami Height

The quake had a predominantly lateral strike slip with a smaller component of vertical dip slip motion. Crustal displacements were of a dipole nature (negative and positive) along a thrust fault approximately paralleling the Chilean coast in N18E orientation. There was a great deal of variation in the extent of vertical crustal displacements. Maximum displacements of up to 200 cms occurred in the offshore region north of Concepción. The maximum vertical uplifted portion (about 2 m) was on the continental side of the rift and the downward portion (about 1.8m) on the oceanic side of the rift. The 2 m uplift was the same as that of the 1835 earthquake, which was parallel to the strike of active faults and antiforms in the Arauco-Concepción region (Melnick et al., 2006). However, these represent maximum crustal displacement values diminishing away from the rift zone. In the region closer to Concepción the offshore vertical displacements were in the order of 50 cms. Upward, ground displacements must have also occurred on land along the affected coastal area - but these remain to be determined by geological surveys. The earthquake was very shallow in depth and this may have limited the extent of the tsunamigenic area.

The ocean area affected by such displacements, the tsunami generating area, is an approximate ellipse in which the fault occupies the major axis. Based on the above assumptions of vertical ocean floor displacements, the initial tsunami height in the generating area is estimated at a maximum of 1.5 - 1.78 meters above the undisturbed sea level.

3.1 Near-field Tsunami Effects

Shortly after the earthquake destructive tsunami waves struck the coastal areas of Central Chile. Coastal cities as Talcahuano, Coquimbo, Antofagasta and Caldera as well as the Juan Fernández Islands, were hardest hit. The largest wave was 9 feet near the quake's epicenter. North and south of the epicentral area at Valparaiso and at Coquimbo, the tsunami lost height rapidly. Overall, the death toll from the tsunami was relatively low in Chile as the waves arrived at night when most people were at home, away from the coastal areas.

Extensive tsunami reconnaissance conducted in the days following the earthquake by the USGS, the NSF funded Tsunami Ocean Sciences Group of the University of Southern California and of Georgia Tech, by EERI and many other groups. The survey findings have been extensively reported on the Internet. The survey by a USGS team determined that the tsunami caused substantial erosion and deposition, which caused local changes of almost 1 m in coastal elevations. The team found clear evidence at two open-coast sites that multiple waves arrived at different times and from different directions and that at an alluvial valley the tsunami inundation was as much as 2.35 km inland. The tsunami run-up heights along the open coast were higher thus differing from those recorded by tide gauges.

Curanipe – Curanipe - that was only 8 km (5 mi) from the epicenter – as well as Pichilemu, Cobquecura, Cauquenes and Parral were hit hard by the tsunami.

Talcahuano - A tsunami struck the port city, which is part of greater Concepción. The greatest impact was along Bahia Concepción and Rio Andalien. The first wave arrived

about 19 minutes after the earthquake. Maximum-recorded wave was 2.34 m (7.7 ft) high. The tsunami was very damaging at the port where large boats and shipping containers were carried inland and piled upon one another. The waves damaged buildings, knocked down trees and blanketed the coastal area with extensive deposits of mud. There were unconfirmed reports of a 15-m-high wave at a beach along the Tumbes Peninsula.

Dichato - A total of seven waves were observed, the sixth being the largest and most damaging. Maximum, reported tsunami wave height was 10 meters and 90% of the town was destroyed. About 50 people were missing and presumed dead. Maximum reported inundation was 2.2 km into a valley.

Constitución - Both the earthquake and subsequent tsunami caused damage at Pelluhue and Constitución. A wave estimated as much as 2m high swept about five blocks into the city about 30 minutes after quake. As many as 350 people are believed to have to have died from the combined effects of the earthquake and the tsunami and hundreds more were reported as missing.

Lioca - Tsunami waves swamped the coastal village of Lloca.

Valparaiso - A 1.29 meter tsunami was observed 20 minutes after the main earthquake at Valparaiso, to the north of the epicentral area. Maximum-recorded height was 2.61 meters 261 at Valparaiso,

Coquimbo - A maximum of 1.64-meter tsunami was recorded at Coquimbo, to the south of the epicentral area.

San Juan Bautista, Juan Fernández Islands - Destructive waves struck the sparsely populated volcanic island group located about 667 km (360 nautical miles; 414 miles) off the coast of Central Chile. The Juan Fernández Archipelago consists of three islands: Robinson Crusoe, Alejandro Selkirk and the small Santa Clara. According to local reports, most of the tsunami fatalities and losses occurred on Robinson Crusoe Island, the largest of the group. There were unconfirmed reports that a gigantic 40-meter (130 feet) high wave hit Robinson Crusoe Island (Spinali, 2010; Newsolio, 2010).   However, later reports indicated that tsunami waves of up to 3 m (10 ft) swept into Cumberland Bay and inundated almost 2 miles into the town of San Juan Bautista, the capital. The waves destroyed the local inn, homes along the water, the school, municipal offices, fishermen's shacks, shops, and a church. According to local reports, fifteen people died and twenty-two more were missing.

3.2 Far-field Tsunami Effects

Hawaiian Islands - Waves of up to 5 ft were reported in Kahului, Maui, and in Hilo about 15 hours after the earthquake, but did little damage.

California - The tsunami was up to 0.53 m in height high and reportedly did some damage. Navigational buoys in Ventura County, California, sustained minor damage as a result of a 2-foot surge and waves, according to the Alaska Tsunami Warning Center. The Ventura

County Fire Department had one report of damage to a resident's dock from the surge. Minor damage occurred in San Diego.

Mexico - In Acapulco the recorded tsunami height in was 0.62 m.

French Polynesia - At the Marquesas Islands, the tsunami measured at 1.79 m (5 ft), but apparently did little damage.

Tonga - Up to 50,000 people evacuated inland in anticipation of the tsunami. There were report of a wave of up to 6.5 feet hitting a small northern island, but no damage occurred.

New Zealand and Australia - Tide gauges recorded a rise of up to 15 cm only.

Japan - Based on experience from the destructive 1960 tsunami which resulted in many deaths, waves of at least 9 ft. in height had been predicted for northern Hokkaido Thousands of people were evacuated from low-lying coastal areas in anticipation of a destructive tsunami. The waves that reached Japan's harbors 24 hours after the quake, raised the water level by up to 0.82 m. Extensive localized flooding occurred in Kesennuma and in Shichigahama, Miyagi Prefecture (state), in northern Japan. At the Tōhoku region damage to the fisheries business was estimated at US $66.7 million.

4. ANALYSIS AND EVALUATION OF THE FEBRUARY 27, 2010 TSUNAMI

The tsunami of February 27, 2010 was generated from an earthquake in the same active seismotectonic zone as that of May 22, 1960 – the latter being extremely destructive, not only locally in Chile but throughout the Pacific Ocean Basin. Given the 2010 earthquake's great magnitude, shallow focal depth and coastal location, it was expected that the far field tsunami impact would have been somewhat similar to that of 1960. However, it was not as severe as anticipated. The following is a cursory review and evaluation of the tsunami generating source characteristics, of the near-field impact and of the possible reasons for the diminished far-field effects. Specifically, the present study examines structural anomalies in the geometry of subduction along Chile's central seismic zone and of source characteristics of past tsunamigenic earthquakes along this segment of the subduction zone. Furthermore, it provides a comparison of similarities and differences of the 2010 event with those which occurred in 1960 and in 1575 - in terms of focal mechanisms, extent of ground and ocean floor displacements, aftershock hypocenter space/time distribution, subduction geometry, absorption, tsunamigenic efficiency, tsunami energy trapping and ducting, as well as of tsunami heights recorded by tide gauge stations.

4.1 Chile's Central Zone Seismicity and Potential for Tsunamigenic Earthquakes.

The Peru-Chile Trench - also known as the Atacama Trench - is the active boundary of collision of the Nazca Plate with the South American Plate. Subduction of the Nazca plate beneath the South America continent is not homogeneous. As a result, asperities and structural complications have caused segmentation along the entire margin, resulting in zones with different rates of slip, seismic activity, volcanism, uplift, terracing and orogenic

processes. Different sections of the margin are segmented by great fractures. Each segment along the Great Peru-Chile Trench has its own characteristic parameters of collision and structural geometry and thus, different potential for large earthquakes and destructive tsunamis. Based on seismicity patterns and clustering of events, Chile can be divided into three distinct seismic regions.

Along central Chile, active tectonic convergence results in extreme seismicity and crustal deformation. The extensive central zone is of particular interest because of its a long history of great subduction zone earthquakes of magnitude 8 or larger that have generated destructive tsunamis.   The central zone extends from 33ºS to 41ºS and this too can be divided into segments that have their own distinct tectonic characteristics, depending on the geometry of subduction, angle of dip and local anomalies. Compressional, tensional and large thrust seismic events have occurred along the entire central zone. Only the large thrust earthquakes are capable of generating significant tsunamis. The following are the distinct segments of Chile's central seismic zone and historic records of tsunami activity.

1. The northern end of the central seismic zone from 33º-34ºS is delineated by the oblique subduction of the leading edge of the Juan Fernández ridge with the Peru-Chile Trench near Valparaiso and the appearance of volcanism at the southern end. Five tsunamigenic earthquakes have occurred in this area in historic times: November 19, 1811; November 19, 1822; October 16, 1868; August 17, 1906 and March 3, 1985.

    The collision of the ridge plays an important role in the development of the forearc features in this region, in the landward deflection of the Peru-Chile trench axis and in the crustal deformation of the convergent margin. For example, a major (Mw 6.7), outer-rise earthquake with a tensional focal mechanism and an unusually high, clustered aftershock sequence occurred on April 9, 2001 (Fromm et al., 2006), supports the existence of preexisting fractures along the ridge that extend to the mainland. Outer rise, compressional and tensional seismicity and ridge collision can be expected to induce uplift of the leading edge of the overriding plate, steepen the inner wall of the trench, compress the sediments along the accretionary wedge and result in additional deformations (McCann & Habermann, 1989). Ridge collision and outer rise events can also nucleate thrust faulting by acting as conduits to hydrate the subducting slab and generate events such as that of 1906 in the vicinity of Valparaiso, or the 1960 at the southern end of the central zone, near Valdivia. However, earthquakes in this northern part of the central seismic zone can be expected to generate local destructive tsunamis, but it is very unlikely that these would have a significant far-field impact in the Pacific basin.

2. South of Valparaiso from 34º-36ºS, a seismic gap existed (Barrientos, 1987). This is the segment that was ruptured by the February 27, 2010 earthquake. Four earthquakes with magnitudes of 7.5 or larger have occurred previously.

3. The Concepcion Region extends from 36º to 37ºS. This region generated two large earthquakes in 1835 and 1939 with magnitudes greater than 8.0. The 1835 quake generated a destructive tsunami. Lesser magnitude earthquakes occurred in 1751, 1868, 1878, 1953 and 1971.

4. The forearc of the active convergent margin of south-central Chile from 37º to 41ºS is

located within the rupture zone of the 1960 Chile earthquake and is characterized by distinct structural changes caused by the geometry of subduction (Rehak et al., 2008). This southern region generated large earthquakes, on October 28, 1562; February 8,1570; December 16, 1575, March 15, 1657, and May 22, 1960. Of these, the 1562, the 1570, the 1575, and the 1960 earthquakes generated destructive tsunamis, locally and in the Pacific Basin.

4.2 Historic Tsunamis of Chile's Central Seismic Zone

The historic record of earthquakes and tsunamis in Chile begins with the arrival of the Spaniards in 1541. The record shows that at least thirty-five tsunamis were generated along the entire subduction zone of Chile by earthquakes of different magnitudes. The first documented tsunamigenic quake occurred near Concepción in 1562 (Iida et al., 1967; Pararas-Carayannis, 1968; Pararas-Carayannis & Calebaugh, 1977) Since then, earthquakes generated tsunamis of various intensities along Chile's coastlines. Great earthquakes along Chile's northern region in 1586, 1687, 1868, and 1877 generated tsunamis that had far-field impact in the Pacific. Seventeen significant tsunamis had their origin along Chile's central seismic zone. Specifically, three tsunamis were generated near the Coquimbo region in 1849, 1943 and 1955. Four more were generated in the Valparaiso region in 1730, 1822, 1871 and 1906. One tsunami originated in the Maule region in 1928. Five more tsunamis originated in the Bio-Bio region in 1562, 1570, 1657, 1751 and 1835. Finally, four more occurred in the Los Lagos region in 1575, 1737, 1837 and 1960. Since 1973, there have been thirteen earthquakes with M>7 along Chile's central seismic zone. The following events generated the more destructive tsunamis in the region.

October 28, 1562 - Great earthquake (Mw8) with epicenter at 38.0 S, 73.5 W. generated a destructive tsunami, which reached a maximum height of up to 16 meters near Concepción.

February 8, 1570 - Great earthquake with estimated magnitude Mw8.8 and epicenter at 37.0 S, 73.0, W. generated tsunami with maximum height of 4 meters.

December 16, 1575 - Extremely severe, great earthquake (similar to 1960) had its epicenter at about 40.0 S., 70.0 W. Strong aftershocks lasted for forty days. There was destruction of five Indian territories south of the Bio-Bio River (Imperial, Valdivia, Villarrica, Osorno and Castro). The quake generated very destructive tsunami waves, which reached Valdivia, 25 km up the river by the same name, destroying houses, uprooting trees and sinking two galleons at the port. Along the coast of La Imperial, north of Valdivia, the tsunami killed 100 people. Landslides blocked the river. A subsequent break of a dam killed 1200 more.

March 15, 1657 - A great earthquake (estimated Mw8.0) and epicenter at about 37.0 S., 73.0 W. generated a tsunami with maximum height of 8.0 meters.

1730 - An earthquake near Valparaíso generated a tsunami, which caused flooding, and damage in Japan.

1751 - Great earthquake (Mw8) near Concepción (36.5S. 74.0W) generated destructive tsunami.
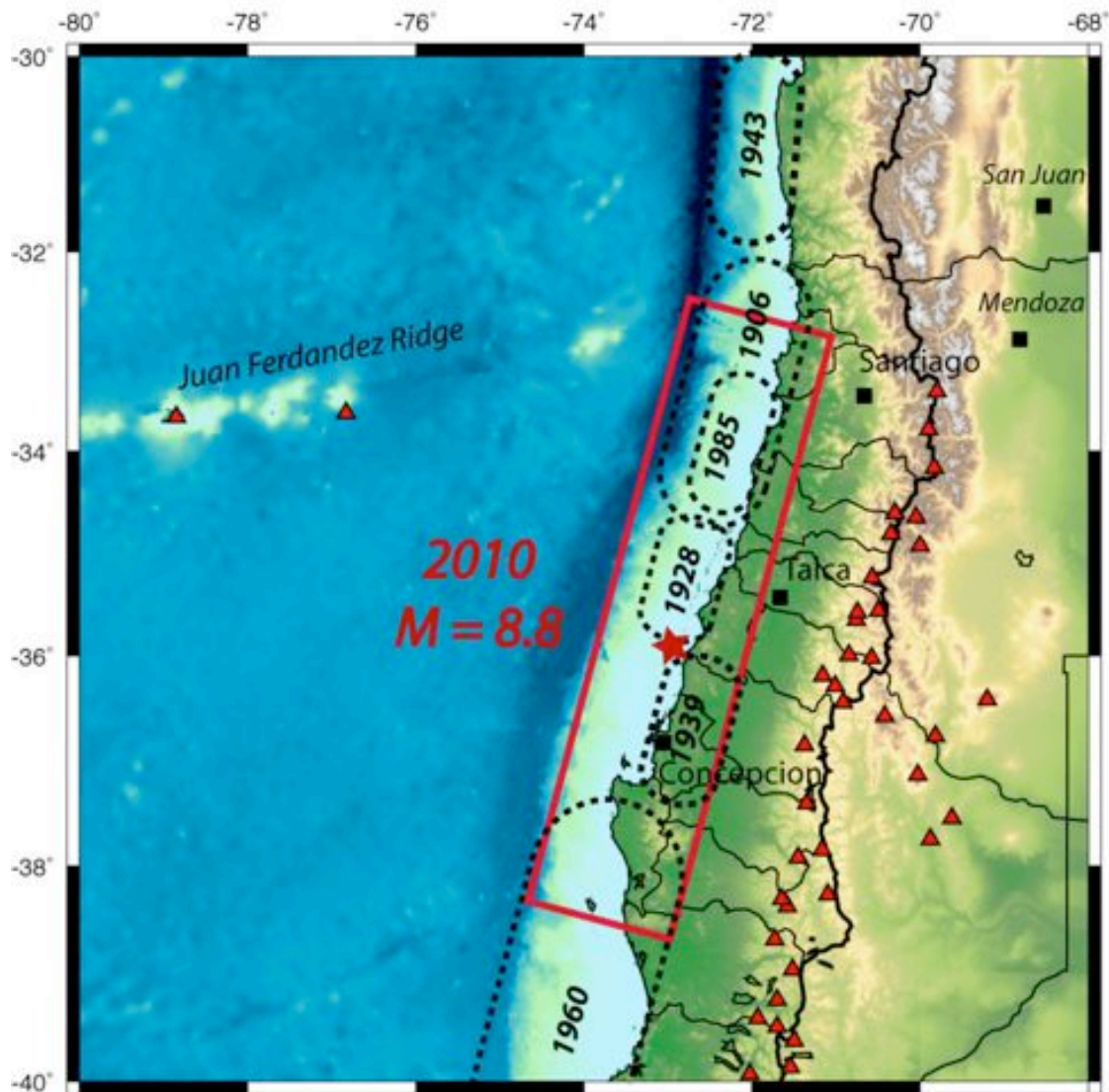
Fig. 6. Area affected by the February 27, 2010 earthquake in relation to historic earthquakes and tsunamis along Chile's central seismic zone. Overlap with the 1960, 1928, 1985 and 1906 events (modified after Beck et al., 1998).

Nov. 19, 1822 - A great earthquake with estimated magnitude Mw8.5 and epicenter at about 33.0S. 71.4W. generated destructive tsunami of 3.5 meters.

February 20, 1835 - Great earthquake (Mw8.2) with epicenter at 36.8S, 73.0W. generated destructive tsunami.

August 17, 1906 - A great earthquake (Mw8.6) with epicenter at 33.0 S., 72.0 W. generated a Pacific-wide destructive tsunami. In Hawaii, waves of 3.5 meters caused damage.

November 27, 1922 - Great earthquake (Mw8.5) with epicenter north of Valparaiso generated a destructive tsunami that significantly impacted central Chile, killing several hundred people and causing severe property damage. A 9-meter local tsunami was particularly damaging near the town of Coquimbo. The tsunami crossed the Pacific and impacted Hawaii, washing away boats in Hilo harbor, Hawaii.

May 22, 1960 - This was the largest earthquake in recorded history and occurred about 240 nautical miles to the SSW of the February 27, 2010 quake. Its magnitude was Mw9.5. It was extremely destructive and very similar to the December 16, 1575 event in same region. Its rupture was estimated to be more than 1,000 kms. The Pacific-wide tsunami that was generated caused extremely devastation in Chile, Hawaii, California, Pitcairn Island, New Guinea, New Zealand, Japan, Okinawa, Philippines and as far away as Australia (4.5m). In Chile, the 1960 quake/tsunami killed 1,655 people and left 2 million people home less. The tsunami accounted for around 200 fatalities in Chile, 61 in Hawaii, 32 in the Philippines, and another 138 in Japan.

4.3 Pre-existing Seismic Gap and Subsequent Stress Release

There are narrow belts of high seismic activity with characteristic clustering of earthquakes near the surface along Chile's entire seismic zone. These are indicative of anomalies that can influence tsunamigenic efficiency. Also, intermediate-depth earthquakes tend to cluster in space. For example, there is a known gap in activity between focal depths of 320 and 525 kms, between latitudes 25.5º and 27ºS. This particular northern region has generated many large shallow earthquakes. The deeper earthquakes are indicative of complex interaction of tectonic plates and anomalies, which can account for differences in the spatial distribution and clustering of the shallower events, as well as for seismic gaps where future large tsunamigenic earthquakes could strike. The same type of shallow and deep hypocenter clustering occurs further south.

The 2010 earthquake involved thrust faulting in the coastal segment of Chile's central seismic zone, where similar anomalies are evident. As mentioned, the region south of Valparaiso from about 34º to 36º South had been identified as a moderate seismic gap where no great earthquake had occurred for many years. With the exception of a 1939 earthquake - inland and deeper - there had been no major or great earthquake in this area for about 120 years. This segment was highly stressed because of the active and oblique subduction of Nazca tectonic plate below South America at high rate of 6.8 cms/yr. The February 27, 2010 earthquake closed the gap.

4.4 Examination of the Rupture Process

Earthquakes along the entire shallow South American subduction zone exhibit heterogeneous and complex rupture characteristics that can be linked to certain Nazca Plate features and subduction zone structure (Bilek, 2009). The February 27, 2010 quake had such a complicated rupture process, which must be examined to help understand the generation of tsunamis from Chile's central seismic zone from about 33º to 37ºS.

The length of the total rupture of the earthquake was about 550 km long and extended to about 50 km in depth. It affected an area of about 82,500 square kms. The

rupture connected directly to that of the great (M=9.5) 1960 tsunamigenic earthquake, which had its origin near Valdivia, immediately to the south. The largest amounts of the 2010 quake's rupture occurred in the first 60 seconds, but smaller displacements continued for up to 200 seconds. A preliminary review of seismic waves radiated by the quake and the distribution and clustering of aftershocks in the following three days, as observed by the GEOFON-measuring network of the GFZ up to March 3, 2010, indicated that the rupture was not continuous. During the first 134 seconds after the start of the rupture and during the first minute, only the immediate region around the actual epicenter appeared to be active. In the second minute the zone of activity moved north towards Santiago. After that the region south of Concepción became active for a short time.

The anomalous rupture process of this earthquake is indicative of complexity in moment release and in slip distribution that can be related to structural variations within the subducting and the overriding plates. It is also significant in understanding how the tsunami's source mechanism is affected by such anomalous process and whether it can be related to the less intense far-field effects of the tsunami.

Also, the numerous strong aftershocks that followed the main shock - some over M6 in magnitude – occurred over a large area. The unusual clustering and chronological sequencing of these aftershocks, as discussed in the next section, are indicative of a segmented and gradual release of tectonic stress. Segmented ruptures and gradual release of energy result in sea floor displacements that will affect significantly tsunamigenic efficiency and near and far-field tsunami impacts. For example, the September 12, 2007 event off Sumatra involved two successive earthquakes, numerous aftershocks and a later strong shock further south/southeast within the same segment that was ruptured by a single great earthquake (Mw=8.7) in 1833 - which generated a very destructive tsunami. However the two Sumatra earthquakes in 2007 which occurred in sequence, released the tectonic stress gradually, thus contributing to the relatively smaller tsunami that was observed in Padang and elsewhere (Pararas-Carayannis, 2007). The unusual rupturing process of the 2010 earthquake also released energy gradually, which could partially account for the less severe near and far-field tsunami effects.
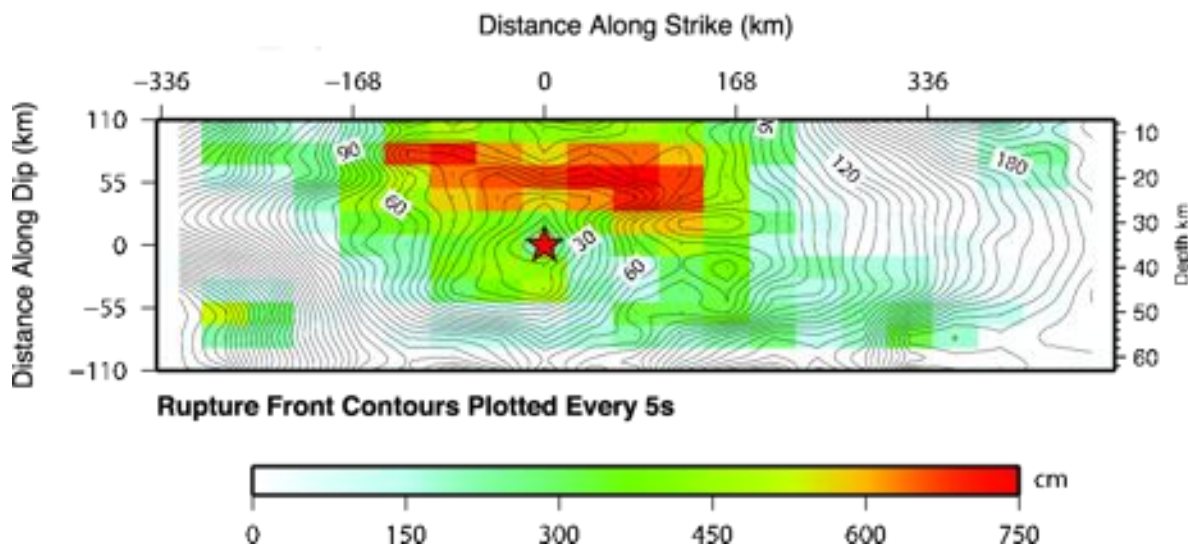

Fig. 7. Rupture process of the February 27, 2010 Earthquake (NEIS)

4.5. Examination of Aftershock Hypocenter Spatial Distribution and Focal Mechanisms

A tsunami's generating area can be determined from the distribution of aftershocks over a coastal area and offshore following a large earthquake, as the aftershocks usually indicate gravitational adjustments of crustal material that contributed to tsunami generation.

As previously stated, there was a vigorous aftershock sequence following the main February 27, 2010 shock. The range of aftershocks over the next days and weeks extended from 33.062^0- 38.5840 South and from 71.574^0-75.199^0 West. There was an unusual clustering in the spatial distribution of the aftershocks in the first few minutes. The initial aftershock sequence indicated the anomalous rupture associated with the earthquake - which must be examined as it may provide clues as to tsunami generation mechanisms in this Central Region of Chile. Furthermore, the swarms, which occurred near the Libertador O'Higgins and Bio-Bio regions following the main shock, appear to have acted as independent families of sequential seismic events. However, it should be pointed out that it is not uncommon for this region to experience clusters of earthquakes which may be perceived as aftershocks, but which in fact may be separate events on adjacent faults, triggered by stress transference.

Application of statistical procedures - such as clustering of groupings and pruning of outlying events – indicated that three major clusters of "aftershocks" occurred, as well as about a dozen small clusters of independent families of seismic events (personal communication with P. Zhol). Whether all of these were really aftershocks or separate events triggered by stress transference, remains to be investigated. Energy may have been released gradually by separate events – as with the September 12, 2007 event off Sumatra (Pararas-Carayannis, 2007) – which may partially account for the lesser far-field impact of the 2010 Chilean tsunami.

The spatial distribution of aftershock hypocenters and their chronological sequence were examined in trying to understand the tsunami's source mechanism as well as the directivity of its energy flux propagation. Review of focal mechanisms and of aftershocks can help understand the type of sea floor displacements that occurred that contributed to tsunami generation and whether the recorded swarms involved normal faulting - which would indicate simple aftershock gravitational settling - or thrust faulting, which would indicate separate events on adjacent faults caused by compression and stress transference.

Also, the problem of spatial distribution and clustering of aftershocks can be studied mathematically as a topological, geometrical manifold for which time is an important dimension, in the sense that each new seismic event (alleged as aftershock) must be considered in terms of previous history and whether it is a member of any existing clusters. What is even more important in understanding the tsunami source mechanism associated with a great earthquake such as the 2010, is the type of crustal displacements and the spatial properties each subsequent seismic event involved, relative to the initial rupture and to subsequent failures on adjacent faults. In other words, how stress is passed-on spatially from one event to another before it is totally released. However, such considerations require a more detailed analysis of geometrical topology and are outside the scope of the present study at this time.

Sequence of Aftershocks and Independent Earthquakes: The following sequence of events took place. An aftershock of M6.2 was recorded 20 minutes after the initial quake. Two more aftershocks with magnitudes M5.4 and M5.6 followed within an hour. An M6.9-magnitude offshore earthquake struck approximately 300 kilometers southwest less than 90 minutes after the initial shock; however, this may have been a separate event that may not have been related to the main shock. In the 2 1/2 hours following the 90-second main shock, 11 more were recorded. Up to the 1st of March a total of 121 aftershocks with magnitude 5.0 or greater were recorded (USGS, NEIC). Eight of these had magnitudes of 6.0 or greater. There was an apparent clustering in the distribution of these aftershocks (Fig. 8 which can be correlated to the anomalous rupture process and perhaps to the tsunami generation mechanism in the sense that displacements of the ocean floor occurred along different faults.

Fig. 8. Initial aftershock distribution showing four distinct clusters, one near the earthquake epicenter, another one closer to Santiago, a third one near Concepción and a fourth one to the south.

On March 5, two more aftershocks above M6.0 were reported. The first was a M6.3, off the coast of Bio-Bio region. The second was a M6.6 near the epicenter of the original quake.   On March 11, a M6.9 quake occurred near Pichilemu in the Libertador O'Higgins Region. It was reported as an aftershock – but apparently it was an independent event. It was followed by two aftershocks of M6.7 and M6.0. However, it will suffice to say that two remarkable events occurred on March 11 but 16 minutes apart, near Libertador O'Higgins which could not be considered as aftershocks, given their magnitude and depth (Table 1).

Table 1. Independent Seismic Events

Date	Time (UTC)	Latitude	Longitude	Magnitude	Depth
11 March	14:55	34.287 S	71.657 W	6.9	44
11 March	14:39	34.290 S	71.950 W	7.2	35

On March 15, two aftershocks of the main February 2010 earthquake were reported, one was a shallow (18 kms) event of M6.1 offshore Maule and the other a M6.7 offshore the Bio-Bio Region, near Cobquecura. Two more minor aftershocks of M5.5 followed.

On March 17, an M5.2 earthquake occurred in Aisén, in Southern Chile. On March 18 an M5.2 earthquake occurred in Los Lagos. On March 26, an M6.2 earthquake occurred in the Atacama Desert region, in Northern Chile.

By March 29, 2010, a total 458 aftershocks had been recorded.

The Bio-Bio region had an unusual sequence of aftershocks and what appear to be independent quakes. A strong M5.9 aftershock struck on April 2. Its epicenter was on land and its focal depth was 39 km. Another strong M6.2 aftershock struck again the same region on April 23. On May 3, a shallow (20Km) M6.4 earthquake struck again the offshore Bio-Bio region. On July 14, 2010, another M6.5 earthquake occurred again in the same area. The significance of the aftershock distribution and of their spatial clustering for tsunami generation is discussed in a subsequent section.

4.6 Source Mechanism of the February 27, 2010 Earthquake and Tsunami

Based on the areal extent and clustering of aftershocks and on geological and macroseismic observations, we can conclude that the earthquake of February 27, 2010 involved multiple ruptures of adjacent faults and various vertical crustal displacements of the ocean floor. Although the overall affected area was extensive, the greater vertical ocean floor displacements of up to 2 meters occurred in the region north of Concepción while the rest of the tsunami source area had displacements of 50 centimeters. The bulk of the earthquake energy that went into tsunami generation was in that limited region, thus the near and far-field effects were not as severe as those of the 1960 event that involved greater ocean floor displacements over a very extensive area. Furthermore most of the tsunami's energy was directed towards Talcahuano but also towards the Juan Fernández islands and French Polynesia. As discussed subsequently, the Juan Fernández ridge and the O'Higgins seamount further altered the far-field characteristics of the tsunami.

4.7 Examination of a Reported 40-meter Tsunami Wave

Shortly after the earthquake, there was an unconfirmed report that a 40-meter high tsunami wave swept over San Juan Bautista on Robinson Crusoe island of the Juan Fernández Archipelago (Spinali, 2010; Newsolio, 2010). The report was clearly erroneous as such wave was physically impossible. The small town is at Cumberland Bay on the northern center of the

mountainous coast of the island and the bay has a northeast configuration (Fig. 9). The tsunami generating area was some 670 km away to the southeast. Thus, the actual destruction at San Juan Bautista resulted from a 3 m (10 ft) tsunami, which resulted from edge waves that refracted around the north part of the island and perhaps were amplified by Cumberland Bay's bathymetry.

Fig. 9. Robinson Crusoe Island of the Juan Fernández Archipelago. Tsunami destruction occurred in the town San Juan Bautista in Cumberland Bay on the north shore.

   Although the reported 40-meter wave at San Juan Bautista was a gross exaggeration, it may not be outside the realm of possibility for some other coastal location on the island. As demonstrated for the November 26, 2006 Kuril islands tsunami at Crescent City, both local and distant bathymetric features and local resonance can be changed by natural shelf oscillations (eigenmodes) which can amplify local tsunami height, change tsunami travel time and alter characteristics of refraction and reflection and the trapping mechanism of tsunami wave energy (Horillo et al., 2007).
   Much larger tsunami waves than those observed at San Juan Bautista probably struck the southern uninhabited coasts of the islands. The combination of bathymetric features and near shore resonance probably contributed to larger waves - which may have occurred on the low-lying, south coast of (i.e. Playa Larga on Robinson Crusoe island) or at "Isla Afuera" at the western end of the Juan Fernández Archipelago.

4.8 Tsunami Energy Trapping and Ducting by the Juan Fernández Submarine Ridge and Other Bathymetric Features.

Tsunami properties are related to such characteristics as extent of ocean floor displacements and directional orientation of source. Trapping of tsunami energy can be induced by the submarine bathymetry of a sea basin bounded by islands and by seamounts. Excitation of "trapped" eigenmodes (free oscillations) of a basin may increase substantially tsunami height (Tinti & Vannini, 1995), but such resonance effect would be expected to enhance tsunami run-up locally. However, energy trapping by ridges and seamounts can also contribute to directional ducting and the refocusing of tsunami energy directivity over great distances.

Being in the direct path of the February 27, 2010 tsunami, prominent bathymetric features such as the Juan Fernández submarine ridge and the O' Higgins seamount, probably contributed to energy trapping and ducting of tsunami energy flux propagation. Further trapping and ducting probably occurred along the Nazca ridge to the north. Such concentrated energy trapping and ducting of long period waves appears to occur when a tsunami propagates for large distances over oceanic ridges. This was demonstrated by the non-linear, shallow water (NLSW) numerical simulation study of spatial derivatives of global propagation of the tsunami of 26 December 2004 (Kowalik et al. 2005). The high spatial resolution (one minute grid) modeling study of the 2004 tsunami on a supercomputer (with close to 200 million grid points) indicated that very small numerical dispersion occurs when tsunamis waves travel over long distances - and that the Coriolis force plays only a secondary role in the trapping.
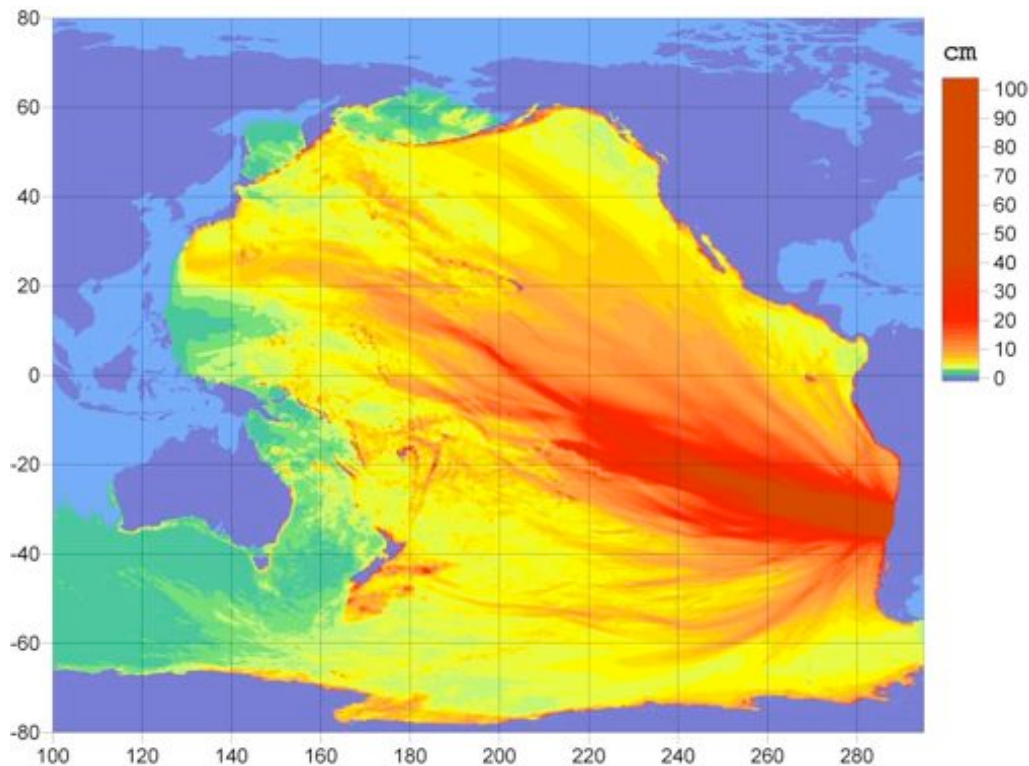

Fig. 10. NOAA map showing predicted amplitudes of the February 27, 2010 tsunami.

Although of lesser spatial grid resolution, the NOAA height forecast model of the 2010 tsunami (Fig. 10), shows bands of stronger energy flux signal in the direction of French Polynesia and towards the north and lesser energy flux directivity towards Hawaii, Japan, New Zealand and Australia. The higher recording of the tsunami in the Marquesas Islands supports such selective directivity in the propagation of tsunami energy towards French Polynesia, which in turn suggests that energy trapping and ducting by the Juan Fernández Submarine Ridge may have been a factor. In the same forecast model, there is a relatively stronger signal directed towards the north Pacific, which indicates some directional amplification, perhaps due to trapping and ducting by some other submarine feature in the immediate vicinity – which may account for the higher tsunami recording in Valparaiso - or the Nazca Ridge further north.

5. COMPARISON OF THE 27 FEBRUARY 2010 AND 22 MAY 1960 EARTHQUAKES AND TSUNAMIS

The February 27, 2010 earthquake generated a tsunami that was destructive locally but was relatively harmless in the rest of the Pacific. By contrast, the May 22, 1960 Chilean earthquake generated tsunami waves of up to 10 meters throughout the Pacific Basin, which devastated Hilo, Hawaii and caused damage as far away as Japan and New Zealand. Comparing similarities and differences between these two events can help understand the seismotectonic characteristics of Chile's central seismic zone from 33ºS to 41ºS and its potential for large earthquakes that can generate tsunamis with significant far-field impacts. Indeed the two events had differences in source characteristics, energy release, geometry of subduction, angle of dip and extent of crustal displacements on land and in the ocean. Also, there were significant differences in coastal geomorphology, spatial distribution of hypocenters, clustering and time sequence of aftershocks and of seismic gaps at depth.

5.1 Differences in Source Characteristics

Both the 2010 and the 1960 earthquakes – as well as that of 1545 - occurred on different segments of Chile's central seismic zone but were caused by the same, on-going crustal deformation associated with oblique tectonic convergence and ridge collision that results in accumulation of strain along this region.

A large precursor event occurred before the great 1960 earthquake struck, but this was not the case not with the 2010 quake. Also, the 1960 quake was associated with much larger subsidence and uplift. Specifically, on 21 May 1960 a great precursor quake with epicenter in the zone of Concepción caused extensive damage to towns in the area and generated a small tsunami, which recorded at 20 to 30 cm in height by the Valparaiso tide gauge. A few hours later, at about 1510 hours on 22 May 1960, the great earthquake struck. With epicenter in the province of Llanquihue, it caused extensive destruction in the region between Concepción and Chiloe and was particularly damaging at Puerto Montt, Valdivia, Ancud, Castro, and Corral. The quake caused both subsidence and uplift of land on Chile's coasts and offshore islands. Isla Guafo for example rose by 3 to 4 meters.

Epicenters - The epicenter of the 2010 earthquake was at 35.909 S., 72.733 W offshore from Maule. The epicenter the 1960 earthquake was at 39.50 S., 74.30 W. off the coast of the Valdivia province.
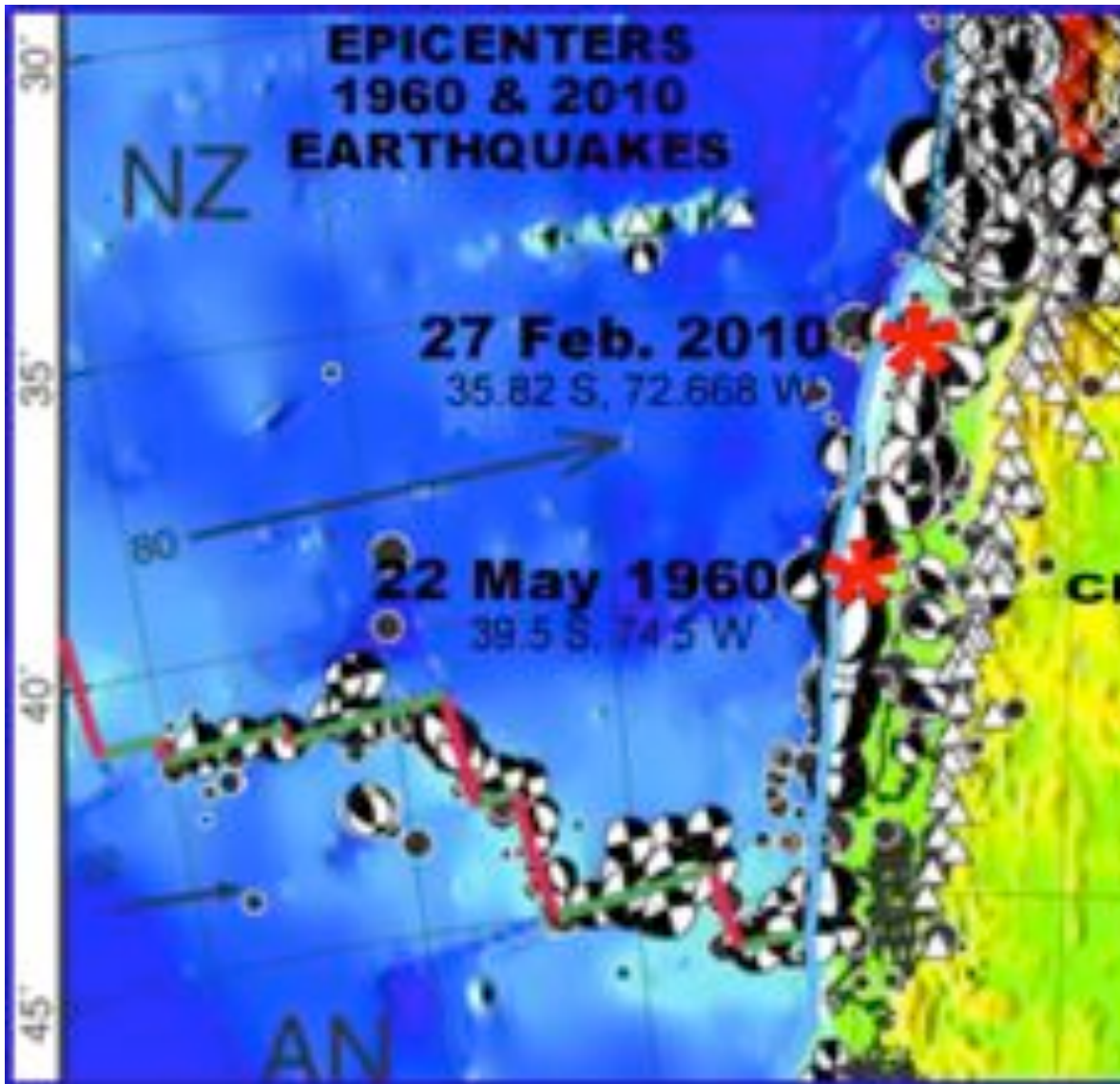

Fig. 11. Epicenters of the 27 February 2010 and of the 22 May 1960 earthquakes. Focal mechanisms of thrust faults on the coast of Chile and of tensional and compressive quakes on the Valdivia and the Juan Fernández Ridge, defining the extent of Chile's central seismic zone from 33^0-41^0 South (modified segment of Un. of Arizona graphic)

Earthquake Magnitudes - The great Chilean earthquake of May 22, 1960, was the largest seismic event ever recorded instrumentally in the world. The earthquake's moment magnitude (MW) was a staggering 9.5. The energy released was about one fourth of the total global seismic moment release between the years 1904-1986. A seismic moment of the 1960 quake was estimated at 2.7×10^{30} dyne-cm (Kanamori & Cipar, 1974), much greater than that of the 2010.

Foreshocks and Aftershocks **-** The 1960 earthquake was characterized by unusually long-period wave associated with a foreshock which occurred 15 minutes before the main shock, indicative of a large slow deformation in the epicentral area prior to the main failure (Kanamori & Cipar, 1974). The focal process resembled a large-scale deformation which begun gradually triggering first the foreshocks and then the main shock. No similar foreshock occurred with the 2010 earthquake, although it had an anomalously slow rupture.

Crustal Displacements **-** The 1960 earthquake affected an area estimated at 1.6×10^5 km^2. Other upper plate features that appear to correlate with earthquake slip may provide links to processes that occur on the megathrust. Wells et al. (2003) correlated the presence of forearc basins with locations of slip during great earthquakes. High slip during the 1960 earthquake occurred in the region of several forearc basins along that segment of the Chile margin (Bilek, 2009). The 2010 quake had with a maximum horizontal displacement of almost 10 meters. Comparison of aftershock distributions shows most of the crustal displacements of 2010 quake on land rather than in the ocean.

Rupture Lengths **-** The aftershock distribution of the 1960 earthquake indicates that its rupture was more than 1,000 km length and about 300 km in width and affected a much greater area. Its rupture velocity was 3.5 km/sec. The 2010 quake's rupture occurred immediately to the north of the segment ruptured by the great earthquake of 1960. It extended over 500 km in length and to depths of over 50 km below the earth's surface. The largest amount of its rupture occurred in the first 60 seconds, but smaller rupture displacements continued for up to 200 seconds.

Geometry of Subduction **-** Large earthquakes involve slip on a fault surface that is progressive in both time and space. Comparisons of focal hypocenters show differences in geometry of subduction near the surface and of dip along the Benioff zone. The 1960 quake had shallower angle of dip near the intersection of the Valdivia fracture zone with South America (Fig. 12) than the 2010 quake in the vicinity north of Concepción (Fig 13, 14). Based on synthetic seismograms a low-angle (10^0) thrust model was found to be consistent with the observed Rayleigh/Love wave ratio and the radiation asymmetry (Kanamori & Cipar, 1974).
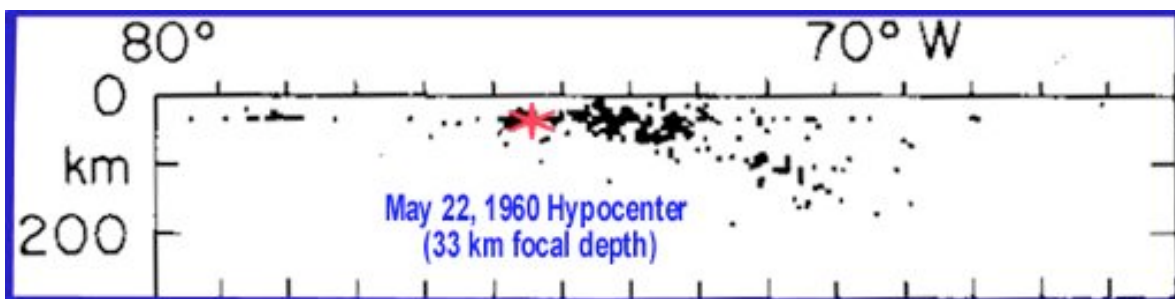

Fig. 12. Spatial distribution of aftershocks of the 1960 earthquake (refer)

An NEIS "map" of the slip on the fault surface of the 2010 Chilean earthquake (Fig. 7) shows how fault displacement propagated outward from an initial point (or focus) about 35

Km beneath the Earth's surface. Also the geometry of formation of the Valparaiso Basin and the aseismic subduction of the ridge seem to exhibit spatial patterns of earthquake ruptures and asperities in the 2010 affected region - something not occurring further south in the source region of the 1960 event.
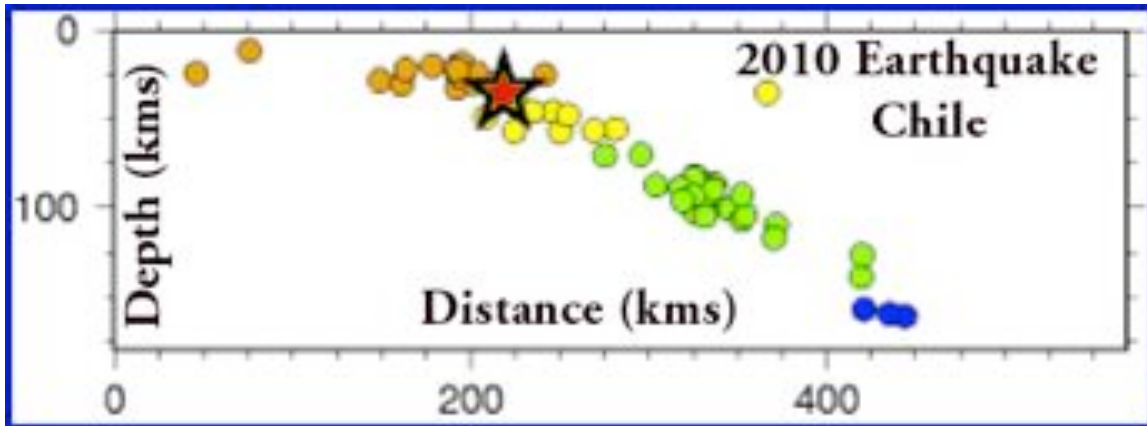

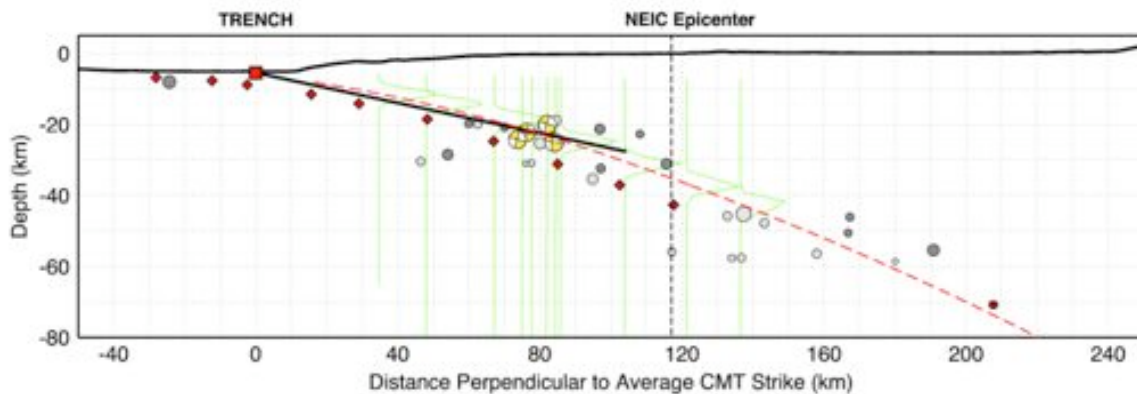*Fig. 13. Spatial distribution of aftershocks of the 2010 earthquake*

Fig. 14. Spatial distribution of aftershocks of the 2010 earthquake (modified NEIS graphic)

5.3 Comparison of Near and Far-field Tsunami Effects

Near-field effects - Given the 2010 earthquake's great magnitude (Mw8.8), greater near and far-field tsunami effects would have been expected. However, the 1960 tsunami had much greater near-field impact. Locally, the 1960 tsunami inflicted extensive damage in ten provinces of Chile. Waves ranging from 3 to 4 meters damaged the port of Lebu. Subsequent successive larger waves caused extensive destruction in Ancud, Bahia Mansa, Corral, Puerto Saavedra, and the coastal islands. Maximum tsunami height reached 14 meters in Maullin. At Caleta Mansa the first wave with a height of 8 meters, arrived 15 minutes after the quake. The second wave had a height of approximately 10 meters and the third was about 12 meters. Abnormal sea conditions continued for several days. Strangely, at Valparaiso the waves of greatest height were observed on 24 May – two days later. Local submarine topography and excitations of natural modes of oscillation (eigenmodes) of the Valparaiso basin may have been responsible for similar anomalies observed at different ports.

By contrast, the maximum tsunami wave heights of the 2010 tsunami observed of recorded locally in Chile, were significantly lower than those of 1960. Table 2 lists some of the heights of the two tsunamis as recorded by operating tide gauges in Chile.

Table 2. Tsunami wave heights in centimeters (above sea level) recorded at some tide gauges in Chile (San Juan Bautista is observed height)

LOCATION	2010	1960	LOCATION	2010	1960
Corral	144	1000	Valparaiso	261	170
Arica	118	220	Talcahuano	234	500
Caldera	90	290	Coquimbo	164	220
San Felix	79	NA	Constitución	200	250
Iquique	68	NA	San Juan Bautista	300	NA
Antofagasta	47	150			
San Pedro	40	NA			

Far-Field Effects - The far-field impact of the 1960 tsunami was much greater than that of 2010. The tsunami caused extensive destruction in Hawaii, Japan, Russia, New Zealand, Australia and elsewhere. The tsunami waves reached maximum height of 13 meters in the Pitcairn Islands, 12 meters in Hilo, Hawaii and up to 7 meters along some of Japan's coastline. By contrast, the 2010 tsunami had lesser amplitudes and caused only relatively small damage and no losses of lives. Table 2 summarizes some of the heights of the two tsunamis as recorded by selective operating tide gauges in the Pacific basin. Although heights recorded by tide gauges are not the maximum amplitudes of the waves that occurred on open coasts, they do indicate quantitatively the relative differences on the degree of tsunami impact.

Tsunami Energy Trapping, Reflection and Refraction - Some of the differences in near and far-field effects of the 1960 and 2010 tsunamis may have been caused by energy trapping and convergence by ducting, reflection and wave refraction. Given the orientation of the 2010 tsunami source and the directivity of maximum energy propagation, the Juan Fernández Juan Ridge, the O'Higgins seamount and other submarine features may have altered the tsunami's far-field impact by redirecting or deflecting its energy, thus resulting in the less significant far field effects that were observed. The submarine features may have trapped, channeled, refracted or reflected tsunami energy. Similar energy trapping by the Juan Fernández Submarine Ridge probably did not occur to the same degree with the 1960 tsunami because the generating source area was further south, was much larger and had different energy directivity. However, the Valdivia submarine ridge may have contributed to energy trapping and ducting of the 1960 tsunami towards the Southwest Pacific basin.

Table 3. Tsunami wave heights in centimeters (above sea level) recorded at some tide gauges in the Pacific.

LOCATION	2010	1960	LOCATION	2010	1960
Pago Pago, Am. Samoa	71	240	Callao, Peru	69	110
Winter Harbour, Canada	22	NA	Currimao, Philippines	16	NA
Rarotonga, Cook Islands	33	NA	Apia, Samoa	42	490
Santa Cruz, Ecuador La Libertad	105 NA	NA 190	King Cove	63	NA
Baltra, Galapagos	41	NA	Atka	42	NA
Rikitea, French Polynesia	32	NA	Seward	39	70
Hanasaki, Japan	95	NA	Shemya	39	NA
Ofunato	40	490	Kodiak	36	70
Naha	30	NA	Yakutat	36	80
Johnston Island	21	50	Craig, Alaska,	23	100
Saipan, Northern Marianas	15	NA	Santa Barbara	91	140
Midway Island	32	60	Crescent City	64	170
Acapulco	65.5	100	La Jolla	60	50
Cabo San Lucas, Mexico	35.9	75	Point Reyes, Calif.	46	NA
Gisborne	117	NA	Kahului	86	340
Chatham Island	101	NA	Kawaihae	51	270
Owenga	98	NA	Nawiliwili	40	150
Raoul Island, New Zealand	50	NA	Honolulu, Hawaii	26	80
			Hilo		1070

6. TSUNAMIGENIC EARTHQUAKES ALONG CHILE'S CENTRAL SEISMIC ZONE – FUTURE IMPACT

Combined oblique convergence, ridge collision and the subduction process play important roles in pre-seismic strain accumulation and must be taken into account in predicting future great tsunamigenic earthquakes along Chile's central seismic zone. The gradient in obliquity of convergence is also a significant factor in slip rates and crustal deformation and in the creation of forearc slivers, which may extend or contract parallel to the major tectonic arc. The build up in strain along this region of the subduction zone eventually requires release in the form of large horizontal and vertical crustal movements that restore temporarily isostatic balance. Thus, the February 27, 2010 earthquake and the numerous subsequent aftershock and independent events released substantial strain along the central seismic zone from about 33-37^0 South. Whether all the strain has been released further south is not known. However, based on the experience gained from the 2010 event, it is safe to conclude that future subduction earthquakes in this particular zone will generate tsunamis with destructive near-field impacts but with lesser far-field effects. The Juan Fernández Ridge, the O'Higgins seamount and other submarine features seem to alter a tsunami's far-field impact by redirecting or deflecting its energy, thus tsunamis generated in this segment do not result in very significant far-field effects.

However, this is not the case with the southern segment of the central zone (37^0-41^{0}S.) where the May 22, 1960 tsunamigenic earthquake occurred. The high seismicity of the Valdivia Ridge (Fig. 11) and the oblique plate convergence contribute significantly to the build up of strain in this southern segment. In the last five decades since 1960, crustal deformation from continuous plate convergence and subduction has been building strain in the region. Although some of the strain has been released partially by smaller events and some has been accommodated elastically, a great deal more is still accumulating. When the threshold limits of crustal elasticity are exceeded again in the region, another great earthquake can be expected. A tsunami similar to those generated by the 1960 and the 1575 earthquakes will have greater far-field tsunami impacts in the Pacific Basin. When such a great tsunami will occur again is very difficult to estimate with any degree of certainty at this time.

Estimating the recurrence frequencies of great earthquakes - based on slip rates - along the southern segment of Chile's central seismic region, is difficult. Apparently, the 1960 tsunamigenic earthquake ended a recurrence interval that had begun almost four centuries before in 1575. Two later earthquakes in 1737 and 1837 produced little subsidence or tsunamis and probably left a great deal of strain in this region from accumulated plate motion that the 1960 earthquake released subsequently (Cisternas et. al., 2005). Based on the intervals of the destructive earthquakes of 1575, 1737, 1837 and 1960, the recurrence frequency for the Valdivia segment has been estimated at 128 ± 31 yr.

Also, historic records of subduction earthquakes show that Isla Santa María is within the southern part of the Concepción seismic segment (Lomnitz, 1970; Barrientos, 1987; Beck et al., 1998; Campos et al., 2002), which nucleated M> 8 subduction tsunamigenic earthquakes in 1570, 1657, 1751 and 1835 (Lomnitz, 1970, 2004; Melnick et al., 2006). Fig. 15 is a cross-section at 37^0 South of the Nazca plate interaction with the South America continent across Isla Santa Maria and the Arauco Basin, just south of Concepción, which illustrates how faulting and oblique compression along the seismogenic

zone nucleates subduction, tsunamigenic earthquakes. Based on the historic events up to 1835, the recurrence of great earthquakes for this segment was estimated at 88 ± 5 yr (mean $\pm 1\sigma$ standard deviation) (Melnick et al., 2006). However, if the 2010 event is included, the average recurrence shifts to 110 yrs intervals. For the Valparaiso segment immediately to the north – based again on historic events - the recurrence is estimated at about 82 ± 7 yr intervals.

Finally, it is quite possible that the strain release from the 2010 event may accelerate the recurrence of another great tsunamigenic earthquake along the southern segment of the central zone. It could occur in a few decades from now or much sooner along the same rupture zone as that of 1960. However, the use of new technology based on GPS geodetic measurements can help assess plate movements and slip rates. Such measurements may eventually lead to more accurate estimates of the recurrence frequency of great tsunamigenic earthquakes along Chile's central seismic zone.
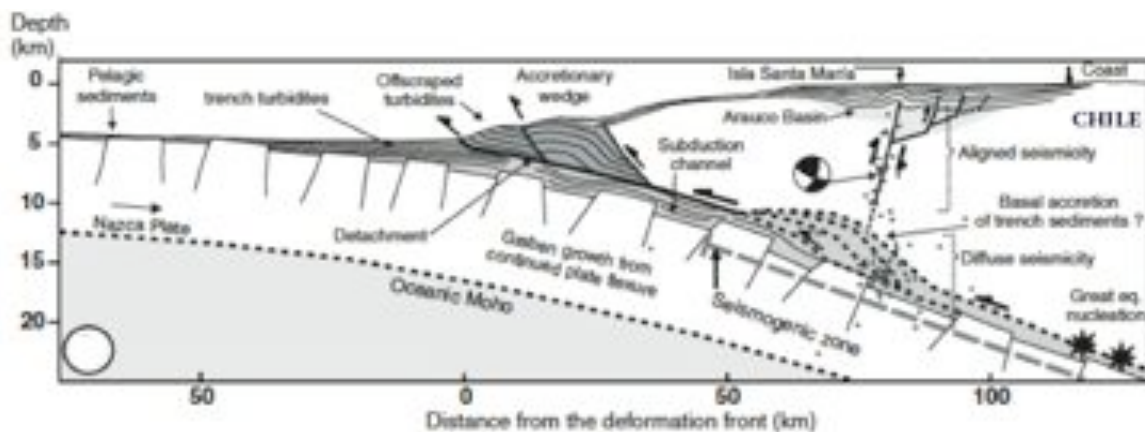

Fig. 15. *Cross-section at 37^0 South across Isla Santa Maria and the Arauco Basin, which illustrates how faulting and oblique compression along the Concepción seismogenic segment deforms the coastline and nucleates subduction-type of tsunamigenic earthquakes (modified after Melnick et al., 2006).*

7. SUMMARY AND CONCLUSIONS

Anomalous rupturing, clustering of aftershocks and slip distribution of earthquakes along the Nazca-South America convergence margin of Chile's central seismic region (33^0-41^0 South) are indicative of complexity in the moment release, which can be correlated to structural variations within the subducting and overriding plates. The anomalous interactions affect crustal displacements along this seismic zone and, therefore, the source characteristics of tsunamis that can be generated from large-scale, thrust and reverse thrust seismic events in the region - nucleated by offshore compressional earthquakes.

The February 27, 2010 earthquake occurred along a seismic gap along the region south of Valparaiso from about 34º South to 36º South of Chile's central seismic zone. The rupture connected directly to that of the great (M=9.5) 1960 tsunamigenic earthquake, which had its origin near Valdivia, immediately to the south. The anomalous, earthquake rupturing of the

2010 event in opposing directions probably has a diminishing effect on tsunami generating efficiency. The unusual clustering and chronological sequencing of aftershocks are indicative of a segmented and gradual release of tectonic stress. The unusual clustering in the spatial distribution of swarms of aftershocks which occurred near the Libertador O'Higgins and Bio-Bio regions following the main shock, appear to have acted as independent families of sequential seismic events. Energy may have been released gradually by such separate events on adjacent faults and this may partially account for observations of different degrees of inundation and tsunami directional approach as well as the lesser, far-field impact of the tsunami.

Evaluation of the source mechanism of tsunami generation associated with the earthquake of February 27, 2010 - as inferred from geologic structure, rupturing process, seismic intensities, spatial distribution of aftershocks, energy release and fault plane solutions - indicates that heterogeneous crustal displacements took place along the entire 550 km. earthquake rupture. As far as tsunami generation is concerned, such anomalous earthquake rupturing in opposing directions would be expected to have a diminishing effect on tsunami generating efficiency. Also, since more significant vertical displacements of the ocean floor occurred in the region north of Concepción, most of the tsunami energy was generated in this region. A good portion of this energy was trapped, ducted or reflected by prominent submarine features such as the Juan Fernández Ridge, the O'Higgins seamount - thus lessening the tsunami's far-field impact by redirecting or deflecting its energy. The crustal displacements and energy, which contributed to tsunami generation, need to be better determined and quantified.
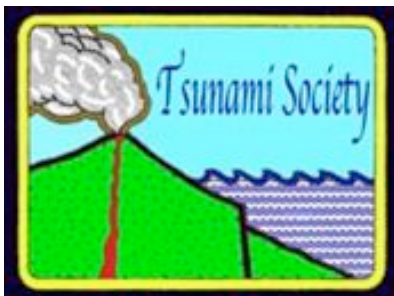
Comparison of the source characteristics of the 1960 and of the 2010-tsunamigenic earthquakes show differences in energy release, geometry of subduction, angle of dip and extent of crustal displacements on land and in the ocean. Also, there were significant differences in coastal geomorphology, spatial distribution of hypocenters, clustering and time sequence of aftershocks and of seismic gaps at depth.

8. REFERENCES

Abe, K., Y. Sato, and J. Frez (1970). Free oscillations of the earth excited by the Kurile Islands earthquake 1963, *Bull. Earth. Res.* 48, 87-114.

Alsop, L. E., G. H. Sutton, and M. Ewing (1961). Free oscillations of the earth observed on strain and pendulum seisomographs, *J. Geophys. Res.* 66, 605-619.

Alsop, L. E. ,1964a. Excitation of free oscillations of the earth by the Kurile Islands earthquake of 13 October 1963. *Bull. Seism. Soc. Am.* 54, 1341-1348.

Alsop, L. E. 1964b. Spheroidal free periods of the earth observed at eight stations around the world, *Bull. Seism. Soe. Am.* 54, 755-776.

Barrientos, S., 1987. Is the Pichilemu-Talcahuano (Chile) a seismic gap?: Seismological Research Letters, v. 61, p. 43–48.

Beck, S., Barrientos, S., Kausel, E. and Reyes, M., 1998. Source characteristics of historic earthquakes along the central Chile subduction zone, *J. South American Earth Sci.* **11**(2), 115–129.

Benioff, H., F. Press, and S. Smith (1961). Excitation of the free oscillations of the earth by earthquakes, *J. Geophys. Res.* 66, 605 649.

Bilek S. L. , 2009. Seismicity along the South American subduction zone: Review of large earthquakes, tsunamis, and subduction zone complexity. Tectonophysics Journal, http://www.elsevier.com/locate/tecto

Bogert, B. P. (1961). An observation of the free oscillations of the earth, *J. Geophys. Res.* 66, 643-646.

Bolt, B. A.,1963. Revised torsional eigen periods from the 1960 Trieste data, *Geophys.* J. 7, 510-512.

Campos, J., Hatzfeld, D., Madariaga, R., López, G., Kausel, E., Zollo, A., Iannacone, G., Fromm, R., Barrientos, S., and Lyon-Caen, H., 2002, A seismological study of the 1835 seismic gap in south-central Chile: Physics of the Earth and Planetary Interiors, v. 132, p. 177–195, doi: 10.1016/S0031-9201(02)00051-1.

Cisternas M., Atwater B. F., Torrejón F., Sawai Y., Machuca G., Lagos M., Eipert A., Youlton C., Salgado I., Kamataki T., Shishikura M., Rajendran C. P., Malik J. K., Rizal Y. & Husni M., 2005. Predecessors of the giant 1960 Chile earthquake. *Nature* **437**, 404-407 (15 September 2005)

Connes, J., P. A. Blum, G. and N. Jobert,1962. Observations des oscillations propres de la terre, *Ann. Geophys.* 18,260-268.

Dziewonski, A. and M. Landisman,1970. Great circle Rayleigh and Love wave dispersion from 100 to 900 seconds, *Geophys. J.* 19, 37-91.

Fromm R., Alvarado P. , Beck S. L. & Zandt G., 2006. The April 9, 2001 Juan Fernandez Ridge (*M*w 6.7) tensional outer-rise earthquake and its aftershock sequence. Journal of Seismology (2006) 10: 163–170, Springer 2006.

Horrillo, J., Knight, W. and Kowalik Z. 2007. THE KURIL ISLANDS TSUNAMI of November 2006. Part II: Impact at Crescent City by local amplification (submitted to J. Geoph. Res.)

Iida, K., D.C. Cox, and Pararas--Carayannis, G., 1967. Preliminary Catalog of Tsunamis Occurring in the Pacific Ocean. Data Report No. 5. Honolulu: Hawaii Inst.Geophys. Aug. 1967.

Kanamori, H. and Cipar J.J., 1974. Focal Process of the Great Chilean Earthquake May 22, 1960. Physics of the Earth and Planetary Interiors, 9 (1974) 128-136. North-Holland Publishing Company, Amsterdam – Printed in the Netherlands.

Kowalik Z.,W. Knight, T. Logan and P. Whitmore (2005), Numerical modeling of the Global Tsunami: Indonesia Tsunami of 26 December 2004. *Science of Tsunami Hazards*, Vol. 23, No. 1, page 40-56. http://www.sfos.uaf.edu/tsunami/global/paper.pdf

Lomnitz, C., 1970. Major earthquakes and tsunamis in Chile during the period 1535 to 1955. Geologische Rundschau 59, 938–960.

Lomnitz, C., 2004. Major earthquakes of Chile: a historical survey, 1535–1960. Seismological Research Letters 75 (3), 368–378.

McCann, W.R., Habermann, R.E., 1989. Morphologic and geologic effects of the subduction of bathymetric highs. Pure and Applied Geophysics 129 (1–2), 41–69.

Melnick D., Bookhagen B., Echtler H. P. & Strecker M. R., 2006. Coastal deformation and great subduction earthquakes, Isla Santa María, Chile (37°S), *GSA Bulletin*; November 2006; v. 118; no. 11-12; p. 1463-1480

Ness, N. F., J. C. Harrison, and L. B. Slichter (1961). Observations of the free oscillations of the earth, *J. Geophys. Res.* 66, 621-629.

Nowroozi, A. A.,1965. Eigen vibrations of the earth after the Alaskan earthquake, *J. Geophys. Res.* 70, 5145-5156.

Nowroozi, A. A., 1966. Terrestrial spectroscopy following the Rat Islands earthquake, *Bull. Seism. Soc. Am.* 56, 1269-1288.

Nowroozi, A. A. and L. E. Alsop (1968). Torsional free periods of the earth observed at six stations around the earth, *Nuovo Cimento, Ser. 1, Suppl.* 6, 133-146.

Newsolio. 2010-02-27. 40 Meter Tsunami Wave Hits Juan Fernández Island". Retrieved 27 February 2010.

Pararas-Carayannis, G., 1968. Catalog of Tsunamis in the Hawaiian Islands. Data Report Hawaii Inst.Geophys. Jan. 1968

Pararas-Carayannis, G. and Calebaugh P.J., 1977. Catalog of Tsunamis in Hawaii, Revised and Updated , World Data Center A for Solid Earth Geophysics, NOAA, 78 p., March 1977.

Pararas-Carayannis, G., 2005. Earthquake and Tsunami of December 26, 2004, in Indonesia http://drgeorgepc.com/Tsunami2004Indonesia.html

Pararas-Carayannis, G., 2007. Earthquakes and Tsunami of September 12, 2007, in Indonesia http://drgeorgepc.com/Tsunami2007Indonesia.html

Rehak K., Strecker M.R., and Echtler H P., 2008. Morphotectonic segmentation of an active forearc, 37°–41°S, Chile. Geomorphology 94 (2008) 98–116,

Slichter, L. B.,1967. Spherical oscillations of the earth, *Geophys. J.* 14, 171-177.

Smith, S. W.,1966. Free oscillations excited by the Alaskan earthquake, *J. Geophys. Res.* 71, 1183-1193.

Spinali, G., 2010. "40 Meter Tsunami Wave Smashes Juan Fernandez Island". Hollywood Backstage. Retrieved 27 February 2010.

Tinti, S. and Vannine C., 1995. Tsunami Trapping Near Circular Islands, PAGEOPH, Vol. 144, Nos. ¾ (1995), Birkhauser Verlag, Basel.